Self-sensing of coil springs and twisted and coiled polymer muscles

van der Weijde, J.O.

DOI
10.4233/uuid:f00eb0bb-6a04-44ba-a7ed-89127a4b3029

Publication date
2020

Document Version
Final published version

Citation (APA)
van der Weijde, J. O. (2020). *Self-sensing of coil springs and twisted and coiled polymer muscles*. [Dissertation (TU Delft), Delft University of Technology]. https://doi.org/10.4233/uuid:f00eb0bb-6a04-44ba-a7ed-89127a4b3029

SELF - SENSING 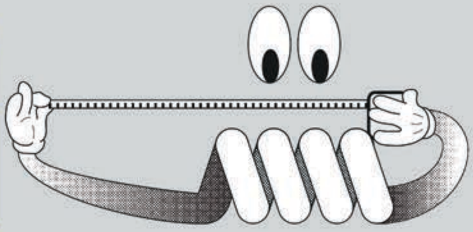

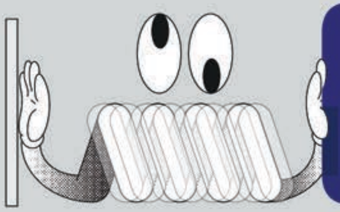 OF COIL SPRINGS

AND TWISTED AND 

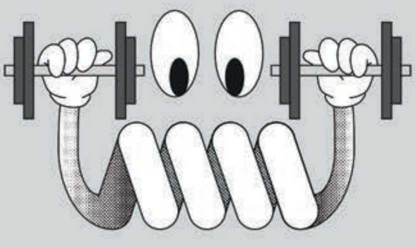 COILED POLYMER

MUSCLES 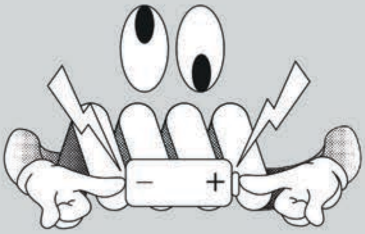

JOOST VAN DER WEIJDE

SELF-SENSING OF COIL SPRINGS AND TWISTED AND COILED POLYMER MUSCLES

SELF-SENSING OF COIL SPRINGS AND TWISTED AND COILED POLYMER MUSCLES

Proefschrift

ter verkrijging van de graad van doctor
aan de Technische Universiteit Delft,
op gezag van de Rector Magnificus prof. dr. ir. T. H. J. J. van der Hagen,
voorzitter van het College voor Promoties,
in het openbaar te verdedigen op donderdag 17 september 2020 om 12:30 uur

door

Johannes Oosten VAN DER WEIJDE

werktuigkundig ingenieur, Technische Universiteit Delft, Nederland
geboren te Haarlemmermeer, Nederland.

Dit proefschrift is goedgekeurd door de promotors:

Prof. Dr.-Ing. H. Vallery
Prof. dr. R. Babuška
Dr. ir. R. A. J. van Ostayen

Samenstelling promotiecommissie:

Rector Magnificus,	voorzitter
Prof. Dr.-Ing. H. Vallery,	Technische Universiteit Delft, promotor
Prof. dr. R. Babuška,	Technische Universiteit Delft, promotor
Dr. ir. R. A. J. van Ostayen,	Technische Universiteit Delft, promotor

Onafhankelijke leden:

Prof. dr. A. A. Zadpoor,	Technische Universiteit Delft
Prof. dr. R. Carloni,	Rijksuniversiteit Groningen
Prof. dr. ir. D. J. Rixen,	Technische Universität München
Prof. D. G. Caldwell, FREng,	Istituto Italiano di Tecnologia
Prof. dr. ir. D. A. Abbink,	Technische Universiteit Delft, reservelid

Keywords: Self-Sensing, Compliant Actuation, Coil Springs, Twisted and Coiled Polymer Muscles

ISBN 978-94-6402-484-5

An electronic version of this dissertation is available at
`http://repository.tudelft.nl/`.

For my wife, and for my parents.

CONTENTS

Summary 1

Samenvatting 3

1 Introduction 5
- 1.1 Motivation . . . 6
- 1.2 Research Questions and Thesis Outline . . . 7

2 Using Coil Spring Inductance for Force Sensing 11
- 2.1 Introduction . . . 12
- 2.2 Modeling Inductance of a Coil Spring . . . 13
- 2.3 Experimental Set-Up . . . 16
- 2.4 Results . . . 18
- 2.5 Discussion . . . 19
- 2.6 Conclusion . . . 21

3 Sensitivity of Electrical Impedance of Coil Springs to Deflection 23

4 Influence of Internal Oscillations on Force Sensing in Coil Springs 27
- 4.1 Introduction . . . 28
- 4.2 Coil Spring Model . . . 29
- 4.3 Simulation . . . 32
- 4.4 Experiment . . . 34
- 4.5 Results . . . 35
- 4.6 Discussion . . . 36
- 4.7 Conclusion . . . 38

5 TCPM Background 39
- 5.1 Working Principle . . . 40
- 5.2 State of the Art . . . 41
- 5.3 Sensing . . . 42

6 Self-Sensing Models of a TCPM 45
- 6.1 Introduction . . . 46
- 6.2 The Muscle . . . 47
- 6.3 Self-Sensing Model Derivation . . . 49
- 6.4 Experiment . . . 51
- 6.5 Results . . . 54
- 6.6 Discussion . . . 55
- 6.7 Conclusion . . . 58

7 Closed-Loop Control of a TCPM via Self-Sensing **59**
7.1 Introduction 60
7.2 Self-Sensing and Control Methods 61
7.3 Experimental Methods 65
7.4 Results 70
7.5 Discussion 71
7.6 Conclusion 74

8 Discussion and Conclusions **75**
8.1 Discussion 76
8.2 Conclusion 82
8.3 Future Research Directions 83

References **85**

A Overview of Compliant Actuators **101**

Acknowledgements **103**

Curriculum Vitæ **105**

List of Publications **107**

SUMMARY

The need to integrate robots in society grows, as several socioeconomic issues put pressure on our current level of productivity and prosperity. This requires robots to safely interact with unpredictable and fragile stakeholders, such as humans. Compliant actuation can facilitate such safe physical interaction.

The Series Elastic Actuator (SEA) and the Twisted and Coiled Polymer Muscle (TCPM) constitute two compliant actuators with favorable properties. However, both need sensors to be able to perform closed-loop control. This complicates design and integration of SEAs, and negates two major benefits of TCPMs. This problem can be solved by determining the state of the actuator via structures or materials that are already part of the actuator, i.e. self-sensing.

Coil-spring-based SEAs and Joule-heated TCPMs have in common that part of their body consists of a coil-shaped conductor. Additionally, every coil has an electrical impedance that changes with its thermomechanical state. In other words, the electrical impedance of a coil-shaped (part of an) actuator can be used for self-sensing.

This thesis investigates the use of electrical impedance for self-sensing of coil springs and TCPMs. These two applications are covered by four main contributions, and two minor contributions. The first contributions regard self-sensing in coil springs, and the last regard self-sensing and subsequent closed-loop control of TCPMs.

In the first main contribution we compare several methods for modeling inductance, and relate this to the deflection of coil springs. Subsequently, we analyze the general trend of the obtained inductance-deflection relations. Simplification of this trend results in a two-parameter description: an inverse-proportional relation with an offset. Fitting this relation to specific coil springs and using it to estimate deflection via inductance results in an estimation error below 2%. A slight overestimation of deflection indicates that there might be non-modeled effects.

In a short study, the first minor contribution compares the sensitivity of inductance to deflection to the sensitivity of resistance to deflection. It uses data gathered in the previous contribution. The results indicate that there is no unambiguous relation between resistance and deflection, while there is for inductance and deflection. Therefore, resistance cannot be used for self-sensing in the same way as inductance.

The second main contribution investigates the performance of several sensor types used to determine the state of a coil spring. Specifically, it studies the effects of dynamic excitation on sensing. Simulations and experiments show that dynamic excitations of coil springs, such as impacts or harmonic excitations, result in internal oscillations of the coil springs. In other words, the windings experience nonuniform movements with respect to each other. These dynamic effects influence measurements of both traditional and inductance-based sensing. However, the magnitude of these effects only becomes relevant when a frequency of the harmonic excitation approaches or equals one of the coil spring's internal Eigenfrequencies.

These contributions show that deflection estimation via inductance sensing in coil springs can compete with traditional sensing methods. However, the experiments in these studies are performed using lab equipment. A practical and affordable sensor could give different results. Additionally, coil springs might be susceptible to electromagnetic disturbances in their surroundings, which could influence the inductance measurements.

The second minor contribution provides a literature study on TCPMs. It explains the working principle, shows the state of the art of research and applications, and discusses other studies on sensing in TCPMs.

In the third main contribution we study the potential of self-sensing in TCPMs. We model the electrical impedance of a TCPM as a function of its thermomechanical state. Subsequently, we rewrite these static models to function as sensing models, i.e. have resistance and inductance as an input, and deflection, temperature and force as an output. Experiments using lab equipment show that the use of these models results in estimation errors below 1% for deflection and temperature, but errors above 7.5% for force. Hence, this study demonstrates that the presented static relations suffice for estimation of deflection and temperature, but not for estimation of force.

In the fourth main contribution we demonstrate closed-loop control of a TCPM via self-sensing. To that end, we employ a practical piece of electronics to both apply power and simultaneously take measurements of inductance. In this contribution, deflection is estimated using measurements of only inductance. This enables closed-loop control of deflection. To also enable force control, we apply a dynamic force model, which uses the applied power and the estimated deflection as input. The resulting closed-loop control bandwidths are 0.039 Hz and 0.056 Hz for control of deflection and force, respectively.

The latter contributions show the potential of self-sensing in TCPMs. However, compared to other compliant actuators, the absolute force a single large-stroke TCPM can apply is small, and the closed-loop control bandwidth is low. To make it a suitable actuator for general robotic applications, the force could be scaled by using structures of TCPMs. In addition, the control bandwidth could be increased by using different configurations, and by influencing the cooling- and heating rates of the TCPMs.

Through its contributions, this thesis contributes to self-sensing of coil springs and TCPMs via electrical impedance. This enables an inexpensive, lightweight and mechanically simple way of providing feedback on the (thermo-)mechanical state of coil springs and TCPMs. In turn, this simplifies the design and integration of SEA and TCPMs.

SAMENVATTING

De druk om robots in de maatschappij te integreren groeit, omdat verschillende sociaal-economische problemen de productiviteit en welvaart onder druk zetten. Dit vereist robots die veilig kunnen samenwerken met onvoorspelbare en kwetsbare belanghebbenden, zoals mensen. *Compliant actuation* (zachte aandrijving) kan die veilige interactie faciliteren.

De *Series Elastic Actuator (SEA)* (Serieel Elastische Actuator) en de *Twisted and Coiled Polymer Muscle (TCPM)* (gedraaide en opgerolde spier van polymeer) zijn compliant actuators met gunstige eigenschappen. Echter, beiden hebben sensors nodig om *closed-loop control* (gesloten-lus regeling) te kunnen verrichten. Dit bemoeilijkt het ontwerp en de integratie van SEAs en doet twee belangrijke voordelen van TCPMs teniet. Dit kan worden opgelost door de staat van de actuator te bepalen via structuren of materialen die al in de actuator zitten. Dit wordt ook wel *self-sensing* genoemd.

SEAs met springveren en elektrisch verwarmde TCPMs hebben gemeen dat ze (gedeeltelijk) bestaan uit een spoelvormige elektrische geleider. Daarnaast heeft elke spoel een elektrische impedantie die verandert met zijn thermomechanische staat. Met andere woorden, de elektrische impedantie van een spoelvormig elektrisch geleidend (onderdeel van een) aandrijfmechanisme kan worden gebruikt voor self-sensing.

Deze thesis onderzoekt het gebruik van elektrische impedantie voor self-sensing van springveren en TCPMs. Deze twee toepassingen zijn opgedeeld in vier hoofdbijdrages en twee kleine bijdrages. De eerste bijdrages gaan over self-sensing in springveren, en de laatste gaan over self-sensing en closed-loop control van TCPMs.

In de eerste hoofdbijdrage vergelijken we een aantal methodes om inductantie te modelleren. Dit relateren we aan de uitrekking van springveren. Vervolgens analyseren we de algemene trend van de verkregen relaties tussen inductantie en uitrekking. Versimpeling van deze trend resulteert in een invers-proportionele relatie met een compensatie parameter. Het toepassen van deze relatie op twee specifieke springveren, en vervolgens het schatten van uitrekking via een gemeten inductantie resulteert in een schattingsfout onder de 2%. Een kleine overschatting van uitrekking laat zien dat er wellicht niet-gemodelleerde effecten zijn.

In een korte studie vergelijkt de eerste kleine bijdrage de gevoeligheid van inductantie voor uitrekking met de gevoeligheid van elektrische weerstand voor uitrekking. Hiervoor gebruikt deze studie de data die verkregen is in de vorige bijdrage. De resultaten geven de indicatie dat de relatie tussen weerstand en uitrekking ambigu is, terwijl die van inductantie en uitrekking dat niet is. Weerstand kan dus niet op dezelfde manier als inductantie gebruikt worden voor self-sensing.

De tweede hoofdbijdrage onderzoekt de prestaties van verschillende sensor types die gebruikt worden om de staat van een spring veer te meten. We bestuderen specifiek de effecten van dynamische belastingen op meetresultaten van verschillende sensors. Simulaties en experimenten laten zien dat dynamische belasting van springveren, zoals

door een schok of een harmonische belasting, resulteert in interne oscillatie van een springveer. Met andere woorden, de windingen bewegen niet eenduidig ten opzichte van elkaar. Deze dynamische effecten beïnvloeden zowel traditionele meetmethodes, als inductantie-gebaseerd meten. Echter, de grootte van de effecten wordt pas relevant wanneer een frequentie van de harmonische belasting een van de interne Eigenfrequenties van de veer benadert of ermee overeenkomt.

De eerste bijdrages laten zien dat het schatten van uitrekking gebaseerd op metingen van inductantie kan concurreren met traditionele meetmethodes. Echter, de experimenten in deze studies zijn uitgevoerd met lab apparatuur. Een praktische en betaalbare sensor kan andere resultaten geven. Daarbovenop kunnen springveren gevoelig zijn voor elektromagnetische storing uit hun omgeving, wat de inductantie metingen kan beïnvloeden.

De tweede kleine bijdrage betreft een literatuurstudie over TCPMs. Deze bijdrage legt het werkingsprincipe uit, laat de *state of the art* van onderzoek en toepassingen zien en behandelt andere studies over het meten in TCPMs.

In de derde hoofdbijdrage bestuderen we het potentieel van self-sensing in TCPMs. We modelleren de elektrische impedantie van een TCPM als functie van zijn thermomechanische staat. Vervolgens herschrijven we deze statische modellen, zodat ze functioneren als self-sensing model. Met andere woorden, het self-sensing model heeft weerstand en inductantie als input, en uitrekking, temperatuur en kracht als output. Experimenten met lab apparatuur laten zien dat gebruik van deze modellen voor uitrekking en temperatuur resulteert in schattingsfouten onder de 1%, en voor kracht in schattingsfouten boven de 7.5%. Dat betekent dat de statische modellen voldoen voor de schatting van uitrekking en temperatuur, maar niet voor de schatting van kracht.

De vierde hoofdbijdrage betreft closed-loop control van een TCPM via self-sensing. Daartoe maken we gebruik van een praktisch stukje elektronica dat tegelijk een vermogen uitstuurt en inductantie meet. In deze bijdrage wordt uitrekking alleen op basis van inductantie geschat. Hiermee is closed-loop control van uitrekking al mogelijk. We passen ook een dynamisch model voor kracht toe, om schatting en regeling van kracht mogelijk te maken. Dit model gebruikt het opgelegde elektrische vermogen en de geschatte uitrekking als input. De resulterende bandbreedtes zijn 0.039 Hz voor closed-loop control van uitrekking en 0.056 Hz voor kracht.

De laatste bijdrages laten het potentieel voor self-sensing van TCPMs zien. Echter, in vergelijking met andere compliant actuators is de absolute kracht die een enkele TCPM kan opbrengen klein, en de bandbreedte voor closed-loop control laag. Om deze actuator geschikt te maken voor generieke robotische toepassingen zou de kracht opgeschaald kunnen worden door structuren van TCPMs te maken. Daarbovenop zouden verschillende configuraties en het beïnvloeden van de koel- en verwarmingssnelheid de bandbreedtes kunnen verhogen.

Door deze bijdrages draagt deze thesis bij aan self-sensing van springveren en TCPMs via hun elektrische impedantie. Dit maakt het mogelijk om op een betaalbare, licht gewicht en mechanisch simpele manier terugkoppeling te geven over de (thermo-) mechanische staat van springveren en TCPMs. Op zijn beurt versimpelt dit het ontwerp en de integratie van SEA en TCPMs.

1

INTRODUCTION

"In a properly automated and educated world, then, machines may prove to be the true humanizing influence. It may be that machines will do the work that makes life possible and that human beings will do all the other things that make life pleasant and worthwhile."

Isaac Asimov, Robot Visions (1990)

THIS thesis investigates the integration of actuating and sensing within robotics hardware. The results may contribute to safer and more productive interaction between robots and humans. The introduction shows the need for compliant actuation and the integration of sensing in two variants. It finishes with the research questions and contributions of this thesis.

1.1. MOTIVATION

The quote by Isaac Asimov at the title page of this chapter sketches a future where robots maintain us humans, such that we can focus on "all the other things that make life pleasant and worthwhile." The sustained growth of life expectancy that our society has experienced over the last few decades has two effects that show that we need such robots sooner rather than later. Firstly, growing life expectancy leads to *gray pressure* [35]. This means that the average workload per working person has to increase, to maintain or increase the national total productivity, and with it the current level of prosperity and its potential to increase [24, 35]. Secondly, as life expectancy grows, the group of elderly citizens that need help with everyday activities grows as well. Prolonging their autonomy helps to reduce the workload of carers, prevents loneliness and reduces the direct negative effects on well-being [5, 31]. Both mitigation of gray pressure and increased autonomy of elderly citizens could be achieved by increased integration of robots in industry and society.

The integration of robots in society is a characteristic feature of an ongoing trend that is already being called the fourth industrial revolution [25]. Several developments illustrate this feature: self-driving cars [44, 146, 166], robots assisting elderly citizens [21, 116], cooperation of humans and robots in factories [41, 162, 176], or integration of robotics in basic human functioning, like active prostheses [52, 106, 119], exoskeletons [53, 160, 165], exosuits [168], or active balance assists [77]. The challenges that we face to successfully integrate robots into society are: defining moral and legal constructs for robots to obey, developing an appropriate interface for communication, and ensuring safe physical interaction [25, 44, 161]. This thesis contributes to one of the fields on which the technological challenges rely: compliant hardware [25, 161].

Compliant hardware is one of the key components to achieve safe physical interaction between humans and robots [25, 161]. Compliant actuators typically consist of one or more physically compliant parts. This makes the drive train of a robot physically compliant in at least the actuated Degree of Freedom (DOF). That makes it more difficult to perform heavy tasks with high precision trajectories, compared to stiff actuators [109]. However, it is easier to control and physically limit the force exerted by the robot. This allows for robots that are inherently safe for interaction.

Today, we have a variety of compliant actuators at our disposal. This includes direct-drive motors, pneumatic actuators, shape-memory alloys, series elastic actuators, artificial muscles, and twisted and coiled polymer muscles. The comparison in Appendix A shows that each type of actuator has its own strengths and limitations. Consequently, they are each suitable for different applications.

Within the variety of compliant actuators, the Series Elastic Actuator (SEA) and the Twisted and Coiled Polymer Muscle (TCPM) have several favorable properties and versatile applications. However, while they do have traction in the research community, they are not widely applied in industry or commercial products. Currently, both SEAs and TCPMs need sensors added to be part of a closed-loop control system. Most SEAs use one of three sensing options: a force sensor as a part of the kinematic chain, a deflection sensor in parallel to the elastic element, or two position sensors on either side of the elastic element. The same sensing solutions apply to TCPMs to measure deflection or force. Adding these sensors complicates the design and integration of SEAs. For TCPMs it increases cost, weight and form factor, which negates some of its major benefits. In addition, a reduced mechanical complexity benefits sustainability by simplifying design, assembly, maintenance, and disassembly and recycling. All these facets illustrate that integration of sensing will bring these compliant actuators closer to application in commercially feasible closed-loop control systems, which may stimulate integration of these systems in society.

1.2. RESEARCH QUESTIONS AND THESIS OUTLINE

Integrated sensing, or self-sensing, involves using the structure or material properties of an already used part to measure the state of that part [60, 86]. For example, self-sensing actuators make use of smart input signals or extra electrical leads to determine their state [60, 86]. By not adding hardware, self-sensing enables feedback control without compromising on cost, weight and complexity.

A common ground between SEAs that use metal coil springs and TCPMs conductively heated with an electrical conductor is that (part of) their elastic element essentially is an electromagnetic coil. This resemblance implies that they have both a resistance and an inductance. Making use of resistance for sensing is already very common. Resistance varies with the resistivity of the material, and the length and cross section of the wire. This is used in, for example, strain gauges. In contrast, inductance is rarely used for sensing. In most geometries the inductance is a negligible property and a source of disturbance. However, in coil springs it might be a suitable property for sensing. Inductance strongly varies with the length of a coil [127], i.e. inductance is a property that is sensitive to changes in deflection of a coil spring. This leads to the following questions:

1. What is the theoretical relation between inductance and deflection of a coil spring?
2. How can we practically use the inductance-deflection relation to measure deflection?

Chapter 2 answers both of these questions. It investigates the geometrically determined inductance-deflection relation. Theory and practice are combined, to deliver a model with two fitted parameters. The results indicate that the accuracy and precision of self-sensing based on this principle can potentially match traditional, primarily resistance-based, sensing methods. However, this does raise the question:

3. How does sensing deflection of coil springs via inductance compare to via resistance?

In a short study Chapter 3 answers this question. Based on data gathered in Chapter 2, it investigates and compares the change of of resistance and inductance with the deflection of coil springs.

The experiments in Chapter 2, illustrated in Figure 1.1, are performed statically. However, the intended applications have to deal with varying disturbances and typically require a dynamic response. Dynamic excitation of coil springs results in oscillation of their windings. This will inevitably influence inductance, which also influences measurements. However, readings of other sensors might also suffer from internal oscillations. This leads to the questions:

4. How do dynamic excitations on coil springs affect measurements of different sensor types?

5. Is the influence of internal oscillations on inductance a practically relevant effect?

Chapter 4 starts with the mechanical modeling of a coil spring to find its transmittance of force as a function of excitation frequency, i.e. the transfer function of force on one end of the coil spring to the other end. Coupling one of the models for inductance found in Chapter 2 to this mechanical model provides a hypothesis for the effect of internal oscillations on different types of sensors. Simulations and experiments on coil springs, illustrated in Figure 1.2, show their response to excitations such as a sine sweep and varying types of impact. The results show that the inductance sensing principle performs equally well, compared to the influence of internal oscillations on traditional sensors.

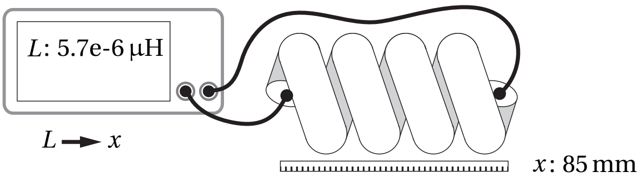

Figure 1.1: Chapter 2 characterizes the relation between inductance L and deflection x of coil springs. This figure conceptually illustrates the performed experiment. The gray box represents the inductance sensor, and the ruler represents the deflection sensor. The numerical values represent a typical data point measured by the respective sensors.

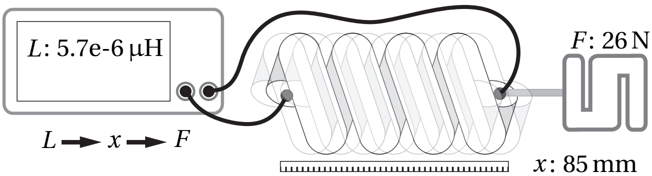

Figure 1.2: Chapter 4 investigates the influence of coil spring oscillations on three sensors, respectively measuring inductance L, deflection x and force F. This figure illustrates the sensors used. The gray box represents the inductance sensor, the ruler represents the deflection sensor and the S-shaped structure represents the force sensor. The numerical values represent a typical data point measured by the respective sensors.

For the previous research questions the scope was limited to the link between the mechanical- and electrical domain. For TCPMs, the thermal domain has to be added, as it is the stimulus of this artificial muscle. To give an introduction into the working principle of TCPMs, and to illustrate the state of the art in research and applications, Chapter 5 presents a review of studies towards TCPMs.

While in SEAs force is estimated from only the deflection of the coil spring, in TCPMs this is a function of both deflection and temperature. Additionally, the resistivity of most metals depends on temperature. This means that measuring the full electrical impedance of a Joule-heated TCPM provides information about its temperature and deflection, and subsequently force. This leads to the following questions:

6. How does the inductance and resistance of a TCPM relate to its deflection and temperature, and subsequently force?

7. What is the estimation quality when using these relations for sensing?

Chapter 6 describes how the electrical impedance of a Joule-heated TCPM depends on deflection and temperature. Rewriting this relation provides a model that can be used for self-sensing. Subsequent experiments identify and validate the sensing model in a static fashion. Figure 1.3 illustrates this experiment. The results confirm that the found relations can indeed be used for self-sensing of Joule-heated TCPMs.

The next step is to actually perform self-sensing in a dynamic fashion, and perform closed-loop control with those measurements. Custom hardware described in [43] is able to obtain a measure of inductance based on the electrical response. Combined with the electrical power as control output, this should provide information on both deflection and force of the muscle. This leads to the following questions:

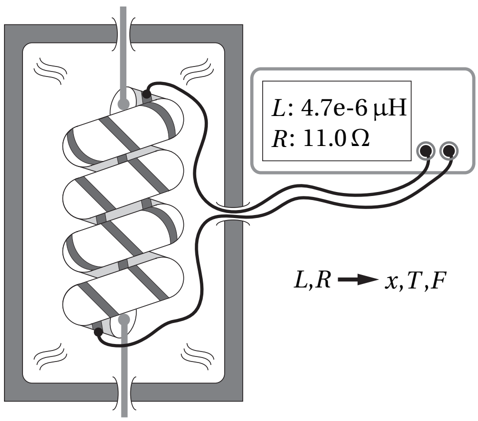

Figure 1.3: Chapter 6 contains a characterization of the relation between inductance L and resistance R, and the thermo-mechanical state of a Joule-heated Twisted and Coiled Polymer Muscle consisting of deflection x, temperature T and force F. This figure illustrates the muscle suspended inside a testing machine with climate chamber, represented by the dark gray box, to apply and measure temperature, deflection and force. The light gray box measures the electrical impedance of the muscle's Joule heating. The numerical values represent a typical data point measured by the respective sensors.

8. What is the performance of self-sensing of force and position of a TCPM, based on input power and measurements of inductance?

9. What is the control performance when using this self-sensing implementation?

Chapter 7 starts with a derivation of a decoupled self-sensing model. It uses inductance to estimate deflection, and power to estimate temperature. Contrary to the study in Chapter 6, this approach requires the physical muscle to have a resistance independent of temperature. This is achieved by the use of a constantan resistance wire. This chapter employs Proportional Integral and Derivative (PID) control to track deflection and force, and uses anti-windup to cope with the imposed limits on input power. Figure 1.4 illustrates the experiment.

Chapter 8 reflects on these research questions, and provides a discussion and the main conclusions of this thesis.

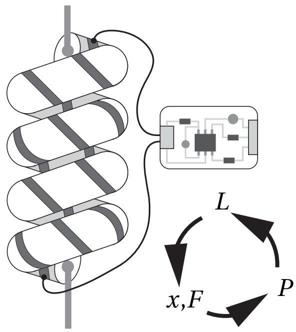

Figure 1.4: Chapter 7 contains an implementation of self-sensing and closed-loop control of a Twisted and Coiled Polymer Muscle using self-sensing. The self-sensing implementation is based on the applied power P and the measured inductance L. It enables closed-loop control of both deflection x and force F. The illustration shows closed-loop control of the muscle's deflection under a constant force, represented by the weight and its position, performed by the custom hardware, represented by the printed circuit board.

2

USING COIL SPRING INDUCTANCE FOR FORCE SENSING

Joost van der Weijde, Erik Vlasblom, Heike Vallery and Michael Fritschi

The content of this chapter has been published in the Proceedings of the IEEE International Conference on Intelligent Robots and Systems (IROS) in 2015.

ABSTRACT
Coil springs are nowadays widely used in robotic applications, in particular in Series Elastic Actuators. The measurement of spring force, either via load cells or via position sensors, conventionally requires additional sensor hardware to be part of or parallel to the kinematic chain. In order to simplify measurement of spring deflection, we exploit the fact that helical springs are in fact solenoid coils, and as such exhibit inductance properties that change strongly with length. We investigate theoretical models for this effect, and we experimentally evaluate the accuracy of such models in predicting spring length from inductance, with and without additional calibrating measurements. Our preliminary results show that a sensing precision as low as 2% can be achieved, indicating that the principle could be suitable for force sensing of compliant actuators.

2.1. INTRODUCTION
Force-controlled robots are found in many new applications, ranging from rehabilitation robotics to robust grasping and manipulation in industrial robotics. This development drives research on compliant actuators and force sensors. Currently, numerous machines rely on springs and their force-deflection characteristic to achieve force control. One typical application herein is the Series Elastic Actuator (SEA) [108].

In a SEA, an elastic element such as a spring is connected between the motor and the joint. In order to control the spring force, either the force or the spring deflection should be measured. Typical solutions for measuring these variables include wire potentiometers [153] and load cells [89]. These solutions require additional sensor hardware to be mechanically put in series with or parallel to the kinematic chain. In general this complicates design.

Some SEAs use joint and motor positions to derive spring deflection from relative displacement between motor and joint. However, this is an indirect measurement of the deflection, which is prone to error due to geometric uncertainties, transmission compliance and noise [55]. Furthermore, it compromises on resolution, since spring deflection is usually much smaller than joint displacement. Particularly for multi-Degree of Freedom (DOF) joints with SEAs [34, 36], measurement of spring forces is challenging.

In this paper, we investigate a new principle to measure spring deflection, exploiting the fact that a helical spring resembles a solenoid coil. This leads to the assumption that such a spring, if made from a conductive material, will exhibit similar inductive behavior (Figure 2.1).

In [67], inductance measurements on Shape Memory Alloy springs were used to determine deflection. However, only empirical data was presented and the theoretical characteristic between spring deflection and inductance was not investigated. In [187], theory was investigated, but only simulations were conducted and no experimental evaluation was included. Here, we investigate several theoretical models and compare them with respect to their accuracy in predicting spring deflection from inductance in practical experiments.

Section 2.2 provides the theoretical background on inductance calculations, applied to coil springs. Section 2.3 describes the measurement set-up, protocol and methods to experimentally determine the spring inductance and deflection. Section 2.4 presents the results. Finally, Section 2.5 and Section 2.6 contain the discussion and conclusion.

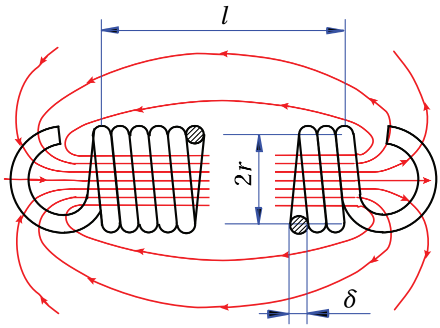

Figure 2.1: Spring of length l, coil radius r, and wire diameter δ, and magnetic field when a current is applied.

2.2. MODELING INDUCTANCE OF A COIL SPRING

In this section, the theoretical background of inductance is investigated. Underlying assumptions and approximations are discussed in order to calculate the inductance of a spring as a function of its deflection.

2.2.1. NEUMANN'S EQUATION

From the law of Biot-Savart, it can be seen that the strength of a magnetic field is proportional to the current and consequently, so is the flux. The constant of proportionality is called the inductance [45, 102]. For the flux through some loop j caused by the magnetic field of a loop i, the inductance can be found using Neumann's equation as:

$$M_{i,j} = \frac{\mu_0}{4\pi} \oint \oint \frac{\mathrm{d}\boldsymbol{l}_j \cdot \mathrm{d}\boldsymbol{l}_i}{r_{i,j}}. \tag{2.1}$$

$M_{i,j}$ refers to the mutual inductance and the constant μ_0 to the magnetic permeability of vacuum. This equation contains a line integral around both loops, where $r_{i,j}$ is the distance between line element vectors $\mathrm{d}\boldsymbol{l}_j$ and $\mathrm{d}\boldsymbol{l}_i$. The self-inductance L_i of loop i is then $M_{i,i}$. Two important observations can be made from this equation. First, it is seen that the inductance is a purely geometric property. It captures the shape of the magnetic field and flux area due to the geometry of the circuit. Second, switching the integral does not effect the end result, meaning that $M_{i,j} = M_{j,i}$ [45].

2.2.2. BASIC MODEL OF COIL INDUCTANCE

Now, we consider a spring of given geometry (Figure 2.1), which can be interpreted as a coil. Generally, the inductance L of a coil is given by the equation:

$$L = \mu_0 \frac{N^2}{l} \pi r^2. \tag{2.2}$$

μ_0 refers again to the magnetic permeability of vacuum, N is the number of windings in the coil, l is the length along the principal axis of the coil, and r is the radius of the coil, measured from the principal axis to the center of the wire [127]. However, this equation assumes homogeneity of the magnetic field inside the coil, and it neglects flux leakage.

Moreover, this equation assumes uniform distribution of windings. For springs of finite length, with round wire and with distance between these wires, it is expected that this equation is not accurate enough. Therefore, the following subsections describe various corrections, approximations and other methods to improve the predicted inductance. For more methods and approximations, see for example [46].

2.2.3. NAGAOKA'S CORRECTION

Magnetic field homogeneity is largely caused by the assumption of the coil having an infinite length l. In reality, the magnetic field lines bend near the ends (Figure 2.1). This difference thus reduces the inductance. Nagaoka found an expression that takes this effect into account [95], conveniently formulated as a variation on (2.2):

$$L = \mu_0 \frac{N^2}{l} \pi r^2 \kappa(r, l), \tag{2.3}$$

where the correction factor κ, called Nagaoka's coefficient, is a function of r and l:

$$\kappa(r, l) = \frac{4}{3\pi k'} \left(\frac{k'^2}{k^2} (K(k) - E(k)) + E(k) - k \right), \tag{2.4}$$

with

$$k^2 = \frac{(2r)^2}{(2r)^2 + l}, \tag{2.5}$$

and

$$k'^2 = \frac{l^2}{(2r)^2 + l}. \tag{2.6}$$

In here $K(k)$ and $E(k)$ are elliptic integrals of the first and second kind.

2.2.4. ROSA'S CORRECTION

In Nagaoka's derivation, the current is assumed to be distributed evenly over the surface of the coil as if it were a tube with infinitesimal wall thickness. This is called a current sheet. Instead, a coil consists of a finite number of windings. Especially in the case of coil springs, these windings have space in between them. Using solutions to Neumann's equation (2.1), the difference between a stack of coaxial circles and its equivalent current sheet was calculated by Rosa [118]. It resulted in a corrected inductance L with

$$L = \mu_0 \frac{N^2}{l} \pi r^2 \kappa(r, l) - \Delta L(N, r, l, \delta). \tag{2.7}$$

The correction $\Delta L(N, r, l, \delta)$with respect to Nagaoka's correction in equation (2.3) is a function of the number of windings N, the pitch l/N and the wire diameter δ, and it is calculated as

$$\Delta L(N, r, l, \delta) = \mu_0 r N (A + B), \tag{2.8}$$

with

$$A = \frac{5}{4} - \log\left(\frac{2l}{N\delta}\right) \tag{2.9}$$

$$B = \frac{2}{N}\sum_{i=1}^{N-1}(N-i)\left(\sum_{j=1}^{\infty}\left(\frac{1}{2j}+\frac{1}{2j+2}-\frac{2}{2j+1}\right)\frac{1}{i^{2j}}\right). \tag{2.10}$$

2.2.5. MAXWELL'S SUMMATION

In his classic works, Maxwell introduced expressions for the inductance of circular currents. By treating the windings as separate circles, the total coil inductance is found by summing the self-inductance and mutual inductance of each circle [85]. Starting from Neumann's equation (2.1), the mutual inductance of two rings i and j can be found as

$$M_{i,j} = -\mu_0 r\left(\left(k_{i,j} - \frac{2}{k_{i,j}}\right)K(k_{i,j}) + \frac{2}{k_{i,j}}E(k_{i,j})\right), \tag{2.11}$$

with

$$k_{i,j}^2 = \frac{(2r)^2}{(2r)^2 + h_{i,j}^2}, \tag{2.12}$$

2

where $h_{i,j}$ is the distance between the rings. For the special case of self-inductance, where $i = j$, Maxwell introduces the geometrical mean distance. In the case of a wire of diameter δ, this is $h_{i,i} = 1/2\,\delta e^{-1/4}$. The total inductance is the sum of the individual inductances. Keeping in mind that $M_{i,j} = M_{j,i}$, it is found that

$$L = NM_{1,1} + \sum_{i=1}^{N-1} 2\,(N-1)\,M_{1,i}. \tag{2.13}$$

It can be seen that Rosa's correction makes use of this summation. In fact, it corrects Nagaoka's solution to come closer to Maxwell's method, but it is computationally less expensive.

2.2.6. INTEGRATING NEUMANN'S EQUATION FOR A HELIX

Finally, several methods exist that also take into account the fact that a coil is a helix instead of a stack of rings. By substituting the coordinates of a helix in Neumann's equation (2.1), the self-inductance can be found. However, in this case, it is not straightforward to find a solution for the double line integral. One can either get a closed-form solution by making approximations that limit the pitch l/N of the helix [133], or resort to numerical integration techniques that are computationally expensive [167]. Using helix coordinates and numerical integration, a solution for a coil spring can be found.

Additionally, it is also possible to include the current distribution in the wire in Neumann's equation by using volume integrals, for example to account for the skin effect. This effect occurs at high frequencies, where the current mainly flows through the outer part of the wire. However, it takes considerably longer to numerically compute the volume integrals, ranging from several minutes to hours depending on the number of windings [131].

2.2.7. FITTED MODEL

By observing the above models, it becomes apparent that the theoretical relationship between deflection and inductance is dominated by an inverse-proportional behavior with offset. In a practical application, it is likely that there are discrepancies between theory and measurements, for example due to manufacturing uncertainties of the springs. Therefore, we propose to use a simplified model that makes use of the general shape of the curve, as predicted by theory, but also uses a limited data set to fit the curve to a particular spring. With reasonable effort, two pairs of data could be generated, e.g. at minimum and maximum deflection of the spring for the application at hand. With

$$L = \frac{\alpha}{l} + \beta \tag{2.14}$$

and the two data points, one can already identify the scaling parameter α and the offset β. Also in [67], a model fit to empirical data was presented. However, since the shape of the deflection-inductance curve was unknown, authors chose to fit a polynomial to a large set of calibration data via optimization. In contrast, our proposed semi-empirical procedure exploits the fact that the shape of the curve is known, such that a very low number of data points (minimally two) is sufficient and calibration can be accelerated. The fitted model (2.14) is computationally inexpensive, and its inversion (to find deflection in function of inductance), is trivial, in contrast to the more complex models explained in the previous subsections.

2

2.3. EXPERIMENTAL SET-UP

In order to assess the predictive power of the models, we conducted measurements with a set of springs. Spring length was varied in a quasi-static manner, while inductance was measured. In the following, the experimental protocol and data analysis will be described.

2.3.1. MEASUREMENT EQUIPMENT AND MATERIALS

The set-up consists of a *Zwick 1484* standard Universal Testing Machine (UTM) to apply and measure an incremental deflection and an LCR-meter (*Wayne Kerr LCR-43100*) to measure inductance. The LCR-meter was placed close to the measured spring. It was connected via shielded two-wire cables and crocodile clips to the hooks on each side of the spring, to ensure proper 4-terminal (Kelvin) measurement. With this equipment, the inductance measurements achieve an accuracy between 0.2% and 0.5% at a signal frequency of 1 kHz. The signal frequency was chosen such that the LCR-meter had the best accuracy attainable, given the range of inductance of the coil springs. The spring fixation was insulated with a thin layer of tape, to prevent other electromagnetic disturbances. The set-up is shown in Figure 2.2.

A set of four stainless steel springs (Verenfabriek TEVEMA, NL) with varying characteristics, as shown in Table 2.1, was chosen to assess validity of the several models. These springs were labeled S1 to S4.

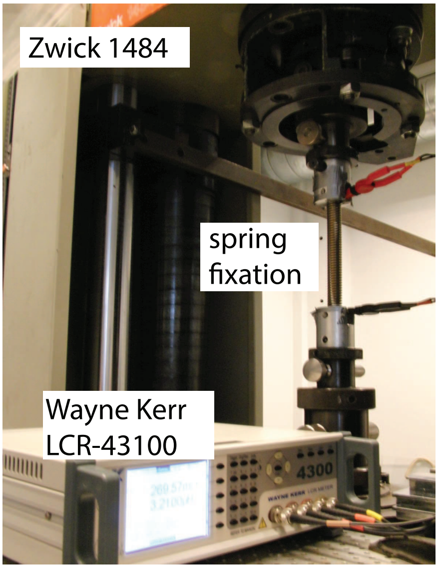

Figure 2.2: Measurement setup, with the Zwick 1484 applying and measuring displacement between the spring fixations, and the Wayne Kerr LCR-43100 measuring inductance of the spring.

Table 2.1: Set of tested springs, with relevant parameters.

Spring	δ (mm)	r (mm)	l_0 (mm)	L_{min} (µH)	L_{max} (µH)
S1	2.8	8.5	117.3	2.71	4.01
S2	2.5	12.5	98.5	6.28	9.03
S3	1.2	5.65	76.3	4.59	7.05
S4	2.2	11.05	50.7	2.92	3.99

2.3.2. MEASUREMENT PROTOCOL

All springs were tested in the same way: A measurement profile for one spring started at 5% elongation from rest length (to ensure the windings did not touch), and it consisted of 10 incremental elongation steps, each time increasing elongation by further 5% of rest length. First, a force well below pretension was applied to align the spring, after which the LCR-meter was calibrated to compensate for the flux area of the wires. Then, at each incremental elongation step, 10 individual measurements were made, with 0.5 s pause after each measurement.

Additionally, the whole measurement sequence was repeated five times with spring S1. For each of these five repetitions, the cables were detached and re-attached, the spring was re-aligned, and the LCR-meter was re-calibrated.

2.3.3. DATA ANALYSIS

For each step of the measurement profile, the mean of the ten measurements was taken to represent the inductance at that step. The standard deviation across the measurements at each step was also computed, to quantify measurement noise. The standard deviation of the means of the five measurement sequences of spring S1 was also computed for each step. This standard deviation quantifies uncertainty due to repositioning of cables and spring, as well as recalibration of the LCR-meter.

The different models described in the previous section have various degrees of complexity. For the evaluation in this paper, all of them were implemented: The basic model in (2.2), Nagaoka's correction for end-effects in (2.3), Rosa's correction for spacing between windings in (2.7), Maxwell's summation in (2.13), and Neumann's equation (2.1) with helical coordinates, using an algorithm from [167] (Because of the relatively low measurement frequency, the skin effect was neglected). Lastly, also the fitted model as proposed in Section 2.2.7 was used, fitted to the first and last data point (so at 5 and 50% elongation).

To assess the precision of the fitted model over multiple measurement sequences, the fit of the first sequence of spring S1, sequence S1-a, was used to calculate deflection for the four remaining sequences, S1-b to S1-e, as well.

To asses how well the various theoretical models and the fit describe the inductance of the springs, the R^2 value was used, which is a measure for the goodness of a fit. For each spring and all models the R^2 value was calculated by

$$R^2 = 1 - \frac{\sum_{i=1}^{n}(y_i - f_i)^2}{\sum_{i=1}^{n}(y_i - \bar{y})^2}, \tag{2.15}$$

in which y_i are the n data points with $\bar{y}$ as their mean, and f_i are the predicted deflections.

In order to predict spring deflection from inductance using the theoretical models (so to invert the models), the models were used to generate a table of 25 values between 0% and 55% elongation. Then, linear interpolation was used to obtain a predicted deflection based on the measured inductance. For the fitted curve, the inverse model was used directly.

For the resulting characteristics, the Root Mean Square Error (RMSE) between the predicted and the actual deflection was computed. This value was divided by the range of the measured deflection, to obtain a percentage. This measure was calculated for all models and each spring, in order to quantify the predictive power of each model.

2.4. RESULTS

The measurement data and the MATLAB code used to do the analysis are publicly available at [1].

The standard deviation of the ten inductance measurements at each step for each individual measurement sequence was found to be in the range of 0.0023 μH to 0.0065 μH. The standard deviation of the mean of measurement profiles S1-a to S1-e ranged from 0.0042 μH to 0.0067 μH throughout the measurement profile.

Figure 2.3 shows the deflection-inductance characteristics of the four springs and the results of all models for each spring. The error bars indicate the standard deviation of the ten measurements at the respective measurement step. For spring S1 only the first measurement sequence is shown. The R^2 values are summarized in Table 2.2, which also includes all measurement sequences of spring S1.

Table 2.2: The R^2 value to asses goodness of fit of the different models for the four springs.

Spring	Basic	Nagaoka	Rosa	Maxwell	Neumann (Helix)	Fitted
S1-a	0.829	0.997	0.216	0.294	0.793	0.998
S1-b	0.846	0.995	0.181	0.260	0.775	0.999
S1-c	0.839	0.996	0.211	0.289	0.787	0.999
S1-d	0.814	0.998	0.250	0.326	0.809	0.997
S1-e	0.830	0.997	0.206	0.285	0.790	0.998
S2	0.953	0.653	-0.414	-0.097	0.182	0.999
S3	0.997	0.838	0.195	0.217	0.539	0.996
S4	-4.143	0.790	0.622	0.940	0.998	1.000

Table 2.3: Root mean square error of predicted spring deflections using the different models.

Spring	Basic	Nagaoka	Rosa	Maxwell	Neumann (Helix)	Fitted
S1-a	12.6 %	1.4 %	30.2 %	28.4 %	14.7 %	1.3 %
S1-b	11.9 %	2.0 %	30.9 %	29.1 %	15.4 %	0.8 %
S1-c	12.4 %	1.6 %	30.4 %	28.6 %	14.9 %	1.1 %
S1-d	13.2 %	1.0 %	29.5 %	27.7 %	14.0 %	1.9 %
S1-e	12.5 %	1.5 %	30.3 %	28.5 %	14.8 %	1.2 %
S2	5.8 %	19.2 %	41.4 %	35.3 %	30.4 %	0.9 %
S3	1.9 %	12.9 %	31.4 %	30.8 %	23.1 %	1.9 %
S4	54.2 %	12.6 %	20.5 %	8.1 %	1.3 %	0.3 %

Predictions of deflection were done for all springs with all models. The predictions were evaluated using the RMSE, of which the results are summarized in Table 2.3.

The result for the predictive power of the fitted model of spring S1 is illustrated in Figure 2.4. The means of each of the five sequences at each step are given. The standard deviations across the sequences lie between 0.16 mm and 0.38 mm, which corresponds to a percentual interval of [0.29,0.71]%. The red solid line indicates the ideal, a perfect prediction. The two measurement points on which the fit is based are the gray plus signs, the predicted points are black dots.

2.5. DISCUSSION

The paper aimed at determining the usability of an inductance-deflection relation for coil springs. For the investigated set of springs, results showed a good qualitative congruence between theoretical deflection-inductance characteristics. Across all springs, none of the models showed a quantitative error between predicted and measured deflection that would be acceptable in a practical application. Nevertheless, a fitted model, which also takes into account two calibration measurements, yielded a deflection prediction below 2%, which would lead to the same percentual errors in force sensing (given linear spring characteristics). This precision would suffice for force sensing in a compliant actuator. Measurement noise of inductance was extremely low.

We also investigated the sensitivity of the measurements to potential error sources such as re-attachment of the inductance measurement connectors to the spring, and re-

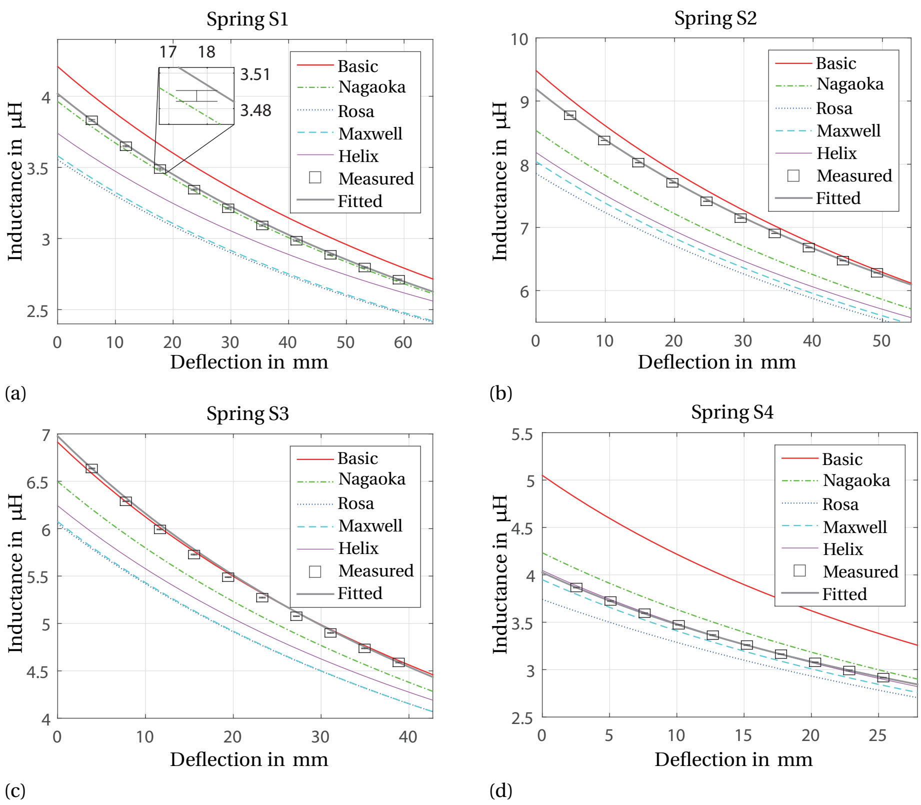

Figure 2.3: Experimentally determined deflection-inductance characteristics of the four springs, compared to predictions of the different theoretical models as well as a simplified model that is fitted to the data. The standard deviations of the measured inductances along the measurement profile of S1 lie between 0.0038 µH and 0.0060 µH, of S2 between 0.0023 µH and 0.0051 µH, of S3 between 0.0037 µH and 0.0055 µH and of S4 between 0.0034 µH and 0.0065 µH.

calibration of the measurement equipment. The influence of these errors was negligible, such that repeatability of the proposed method seems high.

What we did not investigate so far is the dynamic behavior of inductance with respect to spring elongation. Given that inductance is measured e.g. by measuring the time response of an alternating signal, the maximum frequency of this measurement limits the achievable bandwidth. A possible disturbance resulting from dynamic behavior might be a nonuniform distribution of windings due to waves in the spring, which might occur for example when exciting the resonance frequency in any way. Further modeling and experiments with dynamic measurements are needed to determine the influence of these and possibly other adverse dynamic effects.

Furthermore, for some applications a calibration on one specimen might perform sufficiently for another specimen of the same specification. To that end, future research should investigate interchangeability of the results and generalizability of the method.

Potentially, time-dependent effects like creep, and wear and tear during the life time

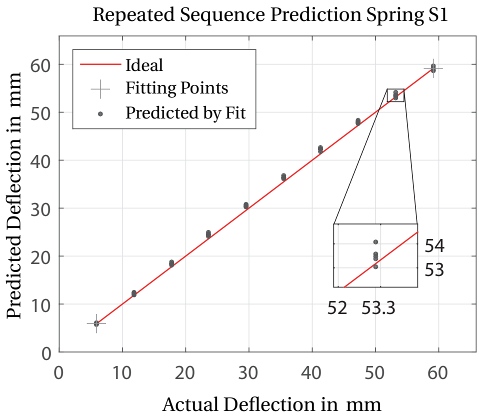

Figure 2.4: The measured versus predicted deflection of spring S1 for five sequences, according to the fit of sequence S1-a. The standard deviations across the sequences lie between 0.16 mm and 0.38 mm.

of a spring could affect the sensing performance as well. An application using this method would strongly benefit from knowledge regarding these time-dependent effects. This could be mitigated by recalibrating the sensor after a predetermined time. These time-dependent effects, and the time interval for which a calibration remains valid, are part of future research.

Further, the influence of diverse electromagnetic disturbances on inductance measurements needs to be investigated. Often operated in close proximity to DC motors, sensors in compliant actuators need to be highly robust to such disturbances. Note that these disturbances do not influence the inductance-deflection relation, but that they influence the measuring of inductance. Future research aimed at implementation of this relation will investigate this sensitivity.

Moreover, the current work investigates basic coil springs. Other coil shapes will most likely also display an inductance-deflection relation. A theoretical derivation similar to the one in Section 2.2 might indicate the required complexity of a fitted relation for these different coil shapes.

Finally, we used a commercial device for inductance measurements in this proof of principle. Preliminary design indicates that in a practical application, the required electronics could be much more compact and lightweight. Practical problems when using the proposed principle in an application are outside the scope of this paper. Detailed design, the precision and accuracy of the resulting sensor and how that compares to conventional, more mature sensing solutions will be the subject of future work.

2.6. CONCLUSION

In this paper, we showed that deflection of steel coil springs can be predicted with high precision and accuracy from inductance measurements of the springs, and that the experimentally determined relationship is qualitatively well explained by theoretical models on inductance of coils. We also showed a simple calibration routine, which exploits the theoretical relationship, and which allows a prediction of deflection with an accuracy below 2%. When the springs are used as force sensors, this would be equivalent to the same accuracy in force, given linear spring characteristics. This opens up new possibilities for measurement of force in compliant actuators, without bulky sensors that measure spring length or force directly.

3

Sensitivity of Electrical Impedance of Coil Springs to Deflection

The work in Chapter 2 theoretically investigates, and practically characterizes the relation between inductance and deflection of a coil spring. It describes the relation as inverse proportional behavior with an offset. However, Chapter 2 focuses solely on inductance, while most methods that rely on deformation of a conductor focus on resistance. For example, the deformation of a strain gauge results in a change in resistance. This indicates the deflection of the structure the strain gauge is applied on, and subsequently the force on that structure. This begs the question stated in the introduction:

> How does sensing deflection of coil springs via inductance compare to via resistance?

To answer this question, this short study analyzes the change in resistance due to deflection of a coil spring. Next, it presents experimental data to verify the analysis and compare with the data obtained in Chapter 2.

A simple analysis of the change in resistance of a coil spring with its deflection requires a few notions. First, the resistance of a homogeneous and uniform piece of wire depends on the area of its cross section, its length and its resistivity [127]. So changes in either will influence resistance. Second, a common assumption attributes the deflection of a coil spring to twisting of its constituent wire, and neglects other deformations like bending and lengthening of the wire [39]. When sticking to small elastic deformations, the twist resulting from coil deflection will hardly influence the cross-sectional area. In other words, deflecting a coil spring only has small influences on change in cross-sectional area and wire length. Third, resistivity changes due to stress [20, 71], but in coil springs the magnitude of these effects are of no practical relevance. Based on these notions, there will be a change in resistance with deflection of a coil spring, but the effects are small.

The experimental comparison is based on the experiment in Chapter 2. It consisted of a Universal Testing Machine (UTM) stretching a coil spring and measuring the applied deflection and resulting force, while an LCR-meter provided data on electrical impedance. The LCR-meter took ten measurements at each deflection. This procedure was repeated for four coil springs. Next to the data on inductance presented in Chapter 2, it also produced data on resistance. Figure 3.1 shows the mean and standard deviation of each series of measurements, for all four coil springs.

Most springs do show variations in resistance with deflection. However, there is no unambiguous relation between resistance and deflection. Therefore, resistance cannot be used for sensing of coil spring deflection in a similar way as inductance.

In general applications, resistance measurements do have benefits over inductance measurements. Actually obtaining data is very easy, and apart from temperature its not very sensitive to its environment. This warrants attempts to find other easy ways of using resistance to measure coil spring deflection. For example, a highly conductive coating on the constituent wire of the coil spring might be sensitive to the small geometric changes happening during coil spring deflection, similar to [2, 3, 143].

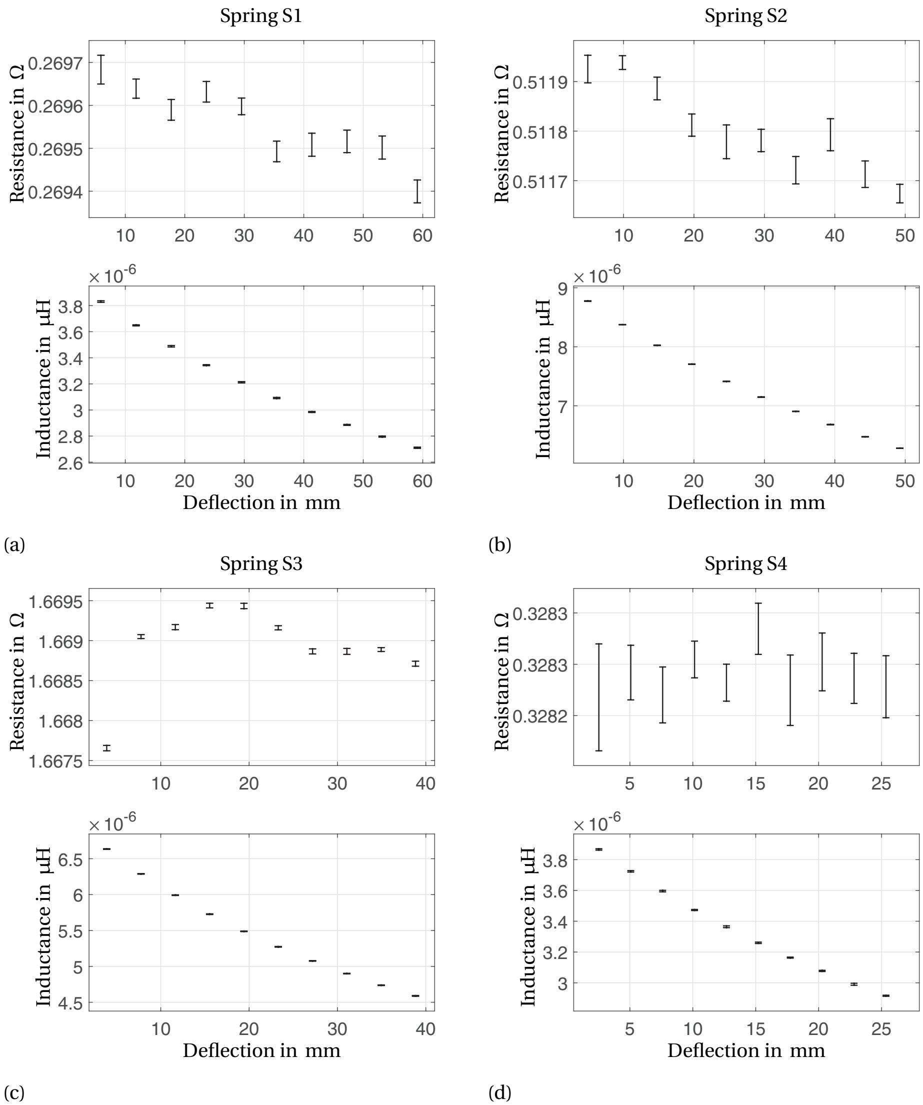

Figure 3.1: Data demonstrating the sensitivity of respectively resistance and inductance to deflection of four coil springs. The errorbars indicate the mean and standard deviation of ten measurements taken at each deflection.

4

INFLUENCE OF INTERNAL OSCILLATIONS ON FORCE SENSING IN COIL SPRINGS

Joost van der Weijde, Ron van Ostayen and Heike Vallery

The content of this chapter has been published in IEEE Robotics and Automation Letters (RA-L) in July 2017.

ABSTRACT

Coil springs are a common element in compliant actuators. For closed-loop control, the force of the coil spring has to be measured. Typically, deflection sensors indirectly measure this force. Implicitly, this assumes that the coil spring is a pure stiffness, without any mass. In reality, oscillations of the windings can occur due to impacts or other excitations of the spring's resonance frequencies. This paper investigates the reliability of different force sensing methods for coil springs that are oscillating internally. In addition to standard sensing via strain gauges or deflection sensors, also a new type of sensing is included, namely force estimation via the spring's own electrical inductance. First, a lumped-mass model is used in simulations of three realistic conditions a coil spring might be subjected to in robotic applications. Second, a hardware experiment is conducted for one condition. Key effects predicted by the model are also found in the experiment, confirming the model's validity. Results show that for all sensors, the increase in measuring uncertainty due to internal oscillations is of the same order of magnitude as typical sensors' measuring uncertainty.

4.1. INTRODUCTION

More and more robotic designs use physical compliance to enhance impedance-controlled interaction, for example around humans [51, 106]. Prominent examples are the Series Elastic Actuator (SEA) [108, 154] and Parallel Elastic Actuators. Most of these robots rely on closed-loop force control, requiring force sensing.

Commercially available force sensors often measure force by means of strain gauges. We call this "direct" force sensing, because only negligible deformations are required. Strain gauges consist of deformable resistors. They are typically used in combination with a structure, where the relation between strain on its surfaces and force at the end points is well known. This structure is typically an S-beam. Another commercial variant of force sensors employs the piezoelectric principle, which enables high precision and stiffness.

Dedicated force sensors are rare in the drive train of SEAs (for example found in [89]). Instead, force sensing in SEAs is mostly performed indirectly, by measuring deformation of the compliant elements. With coil springs as compliant elements, force sensing is simplified by exploiting Hooke's law and linearly relating force to spring deflection. This requires additional deflection sensor elements, e.g. encoders [34, 106] or potentiometers [110, 115, 160]. Ideally, coil-spring deflection is measured directly, for example by placing linear potentiometers. A more indirect option to measure spring deflection in a robotic structure is to take the difference between measurements of two encoders placed on either side of the spring. A SEA typically has those two encoders in its drive train: one motor encoder and one joint encoder. This method relies on the (often incorrect) assumption that any further compliance or backlash in the drive train is negligible.

As a potentially cheaper and simpler sensor, we recently suggested a method to measure force using self-sensing of a metal coil spring, via its inductance [156]. This work, which included the theoretical background of the sensing principle, follows up on earlier empirical work by [67]. This sensing principle has not yet been applied apart from these papers, so its properties still need further investigation. Furthermore, this method is also based on deflection, but does not suffer from uncertainties introduced by the drive train.

What deflection-based sensing methods for spring force in robotics have in common is that they ignore spring mass and thereby inertial effects. Such effects can lead to internal oscillations of coil springs [61, 75, 163], in particular induced by collisions or harmonic excitation near the spring's resonance frequencies. An argument to neglect these internal vibrations is damping. In fact, [163] mentions several causes for damping in coil springs, like hysteresis in the spring material, air damping, friction in the end turns, and loss of energy in the supports. However, finding an actual value for damping requires experimental identification. Also, according to [163], damping in steel coil springs does not significantly change resonance frequencies, and amplification due to resonance may still be as high as 300.

So far, it has not been investigated in how far such oscillations influence force measurement in coil springs, neither for conventional deflection-based sensing, nor for inductance-based sensing. Such knowledge could be beneficial to judge relevance of these oscillations for particular applications, for example SEAs or parallel elastic actuators in robotic devices, or controlled car suspension systems. It can guide the choice of spring designs, sensing principles, sensor locations, or control schemes that are robust to the found uncertainties.

In this paper, we quantify how the different force sensing principles behave immediately following a collision or in response to excitation at a resonance frequency. For this analysis, we first model the coil spring as a system of lumped masses in Section 4.2, and simulate its responses in Section 4.3. Second, we verify the model predictions via a hardware experiment in Section 4.4. Section 4.5 provides the results.

4.2. COIL SPRING MODEL

4.2.1. MECHANICAL MODEL

A coil spring has several Eigenfrequencies with corresponding mode shapes [75]. For our coil spring model, we only consider winding movements in axial direction, containing the first and most prominent mode shape.

The force transfer function for the axial direction of helical springs clamped on one side and with an imposed force at the other, with stiffness k and mass m, has for example been derived in [61]. They give the transmittance of force on one side of the spring F_i to the other side F_o as

$$\frac{F_o(j\omega)}{F_i(j\omega)} = \frac{2}{e^{j\omega\tau} + e^{-j\omega\tau}}, \tag{4.1}$$

where ω is the excitation frequency and τ is the dynamic spring characteristic:

$$\tau = \sqrt{m/k}. \tag{4.2}$$

Note that the dynamic spring characteristic τ is a physical property of a spring and should not be confused with the inverse of Eigenfrequencies, ω_n, of a coil spring. According to [163], Eigenfrequencies of clamped springs are found by

$$\omega_n = n\pi\sqrt{k/m}, \tag{4.3}$$

where n is a positive integer. Equation (4.1) describes the global input-output behavior, but the individual movement of each single winding remains unknown. Particularly

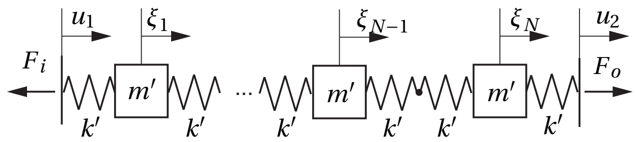

Figure 4.1: N^{th}-dimensional mass-spring model of a coil spring, with inputs u_1 and u_2, positions ξ_1 to ξ_N. The individual masses m' are found by m/N and the individual stiffnesses k' are found by $2Nk$.

for sensing via inductance, a nonuniform winding distribution could influence length measurement.

A lumped-mass model can represent the coil spring in more detail. We take each winding as an individual mass, with massless spring elements on either side. This results in an N-dimensional mass-spring system, where N is the number of windings (Figure 4.1). Following [163], we consider damping negligible.

The absolute positions of the windings, ξ_1 to ξ_N, are collected in the vector ξ and the absolute positions of the end points of the spring are modeled as inputs u_1 and u_2 and collected in the vector $\mathbf{u}$. The vector $\mathbf{S}$ contains the deflections of all massless spring elements in between the masses and the matrix $\mathbf{K}$ contains their stiffness:

$$\mathbf{S} = \begin{bmatrix} \xi_1 - u_1 \\ \xi_2 - \xi_1 \\ \vdots \\ \xi_N - \xi_{N-1} \\ u_2 - \xi_N \end{bmatrix}, \mathbf{K} = \mathrm{diag}\begin{bmatrix} 2Nk \\ Nk \\ \vdots \\ Nk \\ 2Nk \end{bmatrix}, \tag{4.4}$$

The Jacobians of $\mathbf{S}$ with respect to ξ and $\mathbf{u}$, respectively $\mathbf{S}_{,\xi}$ and $\mathbf{S}_{,\mathbf{u}}$, deliver the vector of resultant forces acting on each mass element:

$$\mathbf{F}_s = -\mathbf{S}_{,\xi}{}^{\mathrm{T}}\mathbf{K}\left(\mathbf{S}_{,\xi}\xi + \mathbf{S}_{,\mathbf{u}}\mathbf{u}\right). \tag{4.5}$$

The equations of motion are

$$\frac{m}{N}\ddot{\xi} = \mathbf{F}_s. \tag{4.6}$$

The spring forces at the end points, F_i and F_o, are

$$\begin{bmatrix} -F_i & F_o \end{bmatrix}^{\mathrm{T}} = \mathbf{S}_{,\mathbf{u}}{}^{\mathrm{T}}\mathbf{K}\left(\mathbf{S}_{,\xi}\xi + \mathbf{S}_{,\mathbf{u}}\mathbf{u}\right). \tag{4.7}$$

To validate the mechanical model, we compared its transmittance to the algebraic transmittance in (4.1). The transmittance of the model was obtained by applying a sinusoid force on one end of the coil spring, and investigating the response at the other end, for a frequency range from 1 to 200 Hz with steps of 1 Hz. We determined the amplitude and phase of the output by fitting the response on a sinusoid with the same frequency as the input. Figure 4.2 illustrates the comparison in amplitude, using coil spring S_T in Table 4.1.

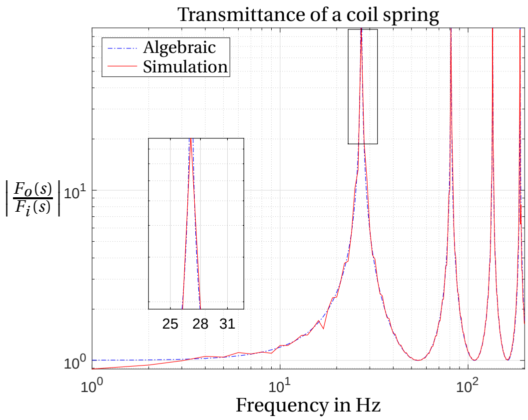

Figure 4.2: Comparison of the algebraically calculated transmittance (blue dash-dotted line) with the transmittance of the model (red solid line). Both represent the transmittance of coil spring S_T in Table 4.1.

4.2.2. INDUCTANCE MODEL

Investigation of inductance-based sensing requires a model of the inductance of a coil spring. We previously provided a comparison of several theoretical inductance-deflection relations [156]. We found that each theory captures the general behavior, given a uniform winding distribution. However, a vibrating coil spring has a nonuniform winding distribution. Maxwell's summation and integration of Neumann's equation are the only theories that capture the influence of a nonuniform winding distribution. Maxwell's summation fits best with the mechanical coil spring model, since it takes individual windings into account. Therefore, we choose this model in the following.

Maxwell's method finds the inductance L of a coil by summation of all mutual inductances $M_{i,j}$ between individual windings i and j. One such mutual inductance is given by

$$M_{i,j} = -\mu_0 r \left(\left(\kappa_{i,j} - \frac{2}{\kappa_{i,j}} \right) K(\kappa_{i,j}) + \frac{2}{\kappa_{i,j}} E(\kappa_{i,j}) \right), \tag{4.8}$$

where μ_0 is the magnetic permeability of air, r the coil radius, $K(\kappa)$ and $E(\kappa)$ the elliptical integrals of the first and second kind, and

$$\kappa_{i,j}^2 = \frac{(2r)^2}{(2r)^2 + h_{i,j}^2}, \tag{4.9}$$

in which $h_{i,j}$ is the distance between the windings, resulting from the mechanical model. For the case of self inductance, where $i = j$, $h_{i,j}$ is given by the geometrical mean distance

$$h_{1,1} = {}^1\!/\!_4\delta e^{-1/4}, \tag{4.10}$$

where δ is the wire diameter. The summation is now given by

$$L = \sum_{i=1}^{N} \sum_{j=1}^{N} M_{i,j}. \tag{4.11}$$

Table 4.1: Parameters of investigated coil springs.

	S_T	S_A
l_0	104 mm	81 mm
N	52	25
r	8 mm	8 mm
δ	2 mm	3.2 mm
m	65 g	80 g
k	760 N/m	9100 N/m
$l_{\min}$	196 mm	82 mm
$l_{\max}$	264 mm	122 mm

4.3. SIMULATION

4.3.1. COIL SPRING PARAMETERS

We investigate two different coil springs that originate from existing robotic platforms. More specifically, they form part of the drive trains of the respective platforms. Coil spring S_T is the antagonistic (front) spring of the SEA in the ankle of the humanoid robot TUlip [34]. Spring S_A is the parallel spring in the drive train of the lower-leg prosthetic ANGELAA [106]. Their relevant properties, rest length l_0, number of windings N, coil radius r, wire diameter δ, mass m, stiffness k and operating range $[l_{\min}, l_{\max}]$ in their respective systems are given in Table 4.1.

4.3.2. CONDITIONS

4

Typical use of coil springs in SEAs involves cases that result in internal oscillations. In the following, three such cases are modeled as conditions, and their respective influence on force sensing is investigated. We simulated each condition for 1 s and analyzed the final 0.25 s.

First, impacts on the structure of the robotic system, for example heel strike of walking robots, are noticed in the drive train. To simplify impact, we consider a coil spring initially moving at a uniform velocity when both ends simultaneously come to a sudden stop. We model this as the windings initially having a uniform distribution with a uniform velocity, with both position inputs fixed. We choose an initial velocity of 0.25 m/s, and we choose the extension for this condition to be at half of the application range.

Second, while extending or contracting the coil spring, the drive train might encounter a physical end stop. To model the behavior immediately after hitting such an end stop, we let the windings initially have uniform spacing, and the velocity be linearly distributed from zero to the extension or contraction velocity, while the inputs are both at a fixed position. A typical human or teen-/man-sized humanoid has a step time of about 1 second [19, 34]. We assume a case where the operating range is traversed within the step time. Therefore, we set the extension and contraction velocity to

$$\max\left(\dot{\xi}_{\text{ext}}\right) = \max\left(-\dot{\xi}_{\text{con}}\right) = {}^{l_{\max} - l_{\min}}/_{1}. \tag{4.12}$$

Both extension and contraction are evaluated. In these cases the end points are, respectively, fixed to the maximum and minimum extension.

Third, an actuator might apply a harmonic force or deflection on one of the inputs of the coil spring. If this sinusoid has a frequency in the neighborhood of one of the spring's Eigenfrequencies, the spring will start resonating. For this condition, we perform two harmonic excitations as a position input, at half of and on the first Eigenfrequency as calculated by (4.3), respectively with an amplitude of 1% and 0.1% of the position range of the coil spring. The other position input remains fixed.

4.3.3. FORCE SENSING MODEL

The sensor behavior is modeled by investigating the response of the coil spring at the points that are relevant for the respective sensors.

Force sensors would be applied at the ends of the coil springs, so their outputs are F_i and F_o as in (4.7).

For the inductance-based sensor, we assume the method given in [156]. A fit with parameters α and β, given by

$$\frac{1}{l_0 + x} = \alpha L + \beta, \tag{4.13}$$

captures the inductance-deflection behavior of a coil spring with a uniform winding distribution. While in a practical application, the parameters would be estimated with two or more inductance measurements at different deflections, here we use the theoretical inductance model in (4.11) with a uniform winding distribution to generate data to estimate α and β. A least-squares fit with a constraint to have the model match the static preload reduces the influence of fitting errors. The inductance response of a vibrating spring, i.e. the inductance with a nonuniform winding distribution, results from the same inductance model (4.11), with the simulated mechanical response as input. The resulting inductance is the input for (4.13), to estimate the deflection of the coil spring. Via the stiffness of the coil spring, we arrive at the inductance-based force measurement F_L.

Both encoders and linear potentiometers can measure net spring deflection x directly. As with the inductance-based method, force is found by multiplication of x with k, to arrive at F_x.

4.3.4. OUTCOME MEASURES

Assessing the relative performance of a sensor requires a definition of nominal behavior and measurement range. Table 4.1 gives the operating range of the investigated coil springs. We define the nominal force F_{nom} as the maximum static force on the coil spring in their respective systems. It is found by

$$F_{\text{nom}} = k\left(l_{\max} - l_0\right). \tag{4.14}$$

We compare F_i, F_o and F_L to F_x for all simulated conditions. We choose the force that assumes a massless, and therefore static, spring, F_x, as a reference. The maximum force differences and the Root Mean Squared Difference (RMSD), indicate the uncertainty of the measurements. From these absolute values, relative measures are computed with respect to the nominal force F_{nom}.

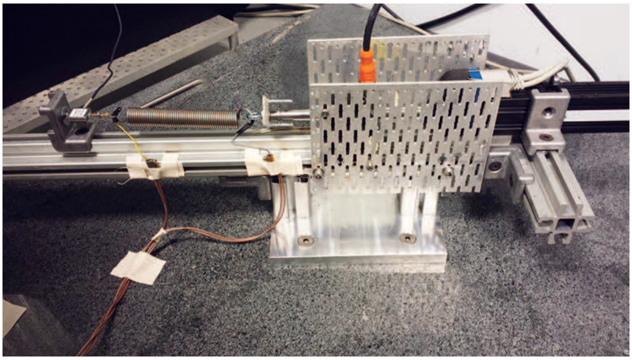

Figure 4.3: The experimental setup: The spring is mounted between a linear actuator and a force sensor. It is also connected to an inductance meter, and a laser distance sensor measures deflection. The motor imposes harmonic oscillations at a range of frequencies, including the spring's first resonance.

4.4. EXPERIMENT

4.4.1. EXPERIMENTAL SETUP

To support the simulation in Section 4.3, we conducted an experiment with a hardware setup that can reproduce one condition, namely excitation by a harmonic oscillation.

The S_T coil spring was suspended between a Dunkermotoren Servotube STA1116 Linear Actuator (LA), and a Futek LSB200 110 N Load Cell (LC). The LA can apply a maximum continuous force of 27 N. The relative deflection of the attachment point at the linear actuator was measured by a MicroEpsilon optoNCDT ILD 1401-10 Laser Distance Meter (LDM). A Matlab Simulink model controlled the LA at 500 Hz, and a National Instruments USB-6211 Data AcQuisition box (DAQ) acquired the signals of the LC and the LDM at 2.5 kHz. An LCR43100 by Wayne Kerr measured the inductance using four-point measurement cables. The LCR43100 needs 445 ms per measurement, which limits the experiment to inductance averaged over several oscillation periods when the oscillations occur. As illustrated in Figure 4.3, all mechanical parts were mounted on a granite slab, to minimize any transfer of vibrations beyond the spring.

4.4.2. PROTOCOL

First, the end of the LA that was fixed to the spring, was moved to the middle of the range of the LDM. This resulted in a preload of about 26 N. To reduce settling behavior during the experiment, we excited the coil spring at half of its Eigenfrequency for two minutes. Next, the stiffness and deflection offset of the coil spring were determined by force and position measurements at the end points of the LDM's range. The fitting parameters for (4.13) were determined using inductance measurements at those positions. We used a least-squares fit, with a constraint to have the fit match the static preload condition.

At the start, the LA held the preload position for 40 s. Next, it applied a series of sinusoid excitations around this position, each with a different frequency, for 40 s per frequency, with an amplitude of 1 mm. The frequencies were chosen such that the measurement time of the LCR43100 contained an integer number of periods of the excitation, starting with 1 and ending with 13 periods. The amplitude is chosen such that the

LA is able to track the reference of the excitation signal, and that the effects are clearly measurable. For each condition, the DAQ and the LCR43100 were triggered simultaneously after the coil spring response had reached a steady state. Due to communication overhead, the LCR43100 took 59 samples per condition. At the end of the experiment, the LA held the preload position again for 40 s, to be able to identify any relaxation effects.

The 12th frequency was close to half the coil spring's first Eigenfrequency. We chose this moderate way of exciting the first Eigenfrequency, to avoid practical problems that would influence the results, like collisions between windings.

4.4.3. DATA PROCESSING

In analogy to the simulation, the force at the load cell F_o can be compared to the force that results from deflection measurements F_x. For all excitations, the RMSD and the maximum deviation were calculated, relative to the nominal force as found by (4.14).

The inductance-based force measurements F_L require a different approach. In the dynamic cases, the LCR43100 measurement gives the averaged inductance over multiple periods of the excitation. The averaged inductance corresponds to an averaged force. Subtracting the deflection-based measurement of the preload provides the averaged force difference. For all three types of force measurement, the relative averaged force differences $\Delta\bar{F}_x$, $\Delta\bar{F}_o$ and $\Delta\bar{F}_L$were calculated, with their standard errors. Standard error $\sigma_{\bar{F}}$ is given by

$$\sigma_{\bar{F}} = {}^{\sigma}/_{\sqrt{n}}, \tag{4.15}$$

with standard deviation σ and the number of samples n.

4.5. RESULTS

Figure 4.4 illustrates the responses of coil spring S_T to the 'heel strike' condition, the 'end stop' condition and the 'resonance' condition of the simulations.

Table 4.2: Root Mean Squared Differences and Maximum Differences of F_o, F_i and F_L with respect to F_x, relative to F_{nom}.

	RMSD			Maximum Difference		
	F_i	F_o	F_L	F_i	F_o	F_L
S_T						
heel strike	1.44%	1.44%	0.01%	3.11%	3.08%	0.00%
end stop collision max	0.22%	0.23%	0.01%	0.46%	0.44%	0.01%
end stop collision min	0.39%	0.39%	0.00%	0.85%	0.84%	0.00%
$^1/_2\,\omega_1$	0.37%	0.27%	0.00%	0.80%	0.42%	0.01%
ω_1	8.93%	8.94%	0.34%	14.39%	14.21%	0.00%
S_A						
heel strike	1.67%	1.67%	0.01%	3.77%	3.78%	-0.00%
end stop collision max	0.15%	0.15%	0.01%	0.46%	0.42%	0.01%
end stop collision min	0.27%	0.27%	0.00%	0.60%	0.61%	-0.00%
$^1/_2\,\omega_1$	0.78%	0.57%	0.02%	1.69%	0.94%	0.04%
ω_1	58.32%	58.36%	7.73%	93.05%	96.41%	0.03%

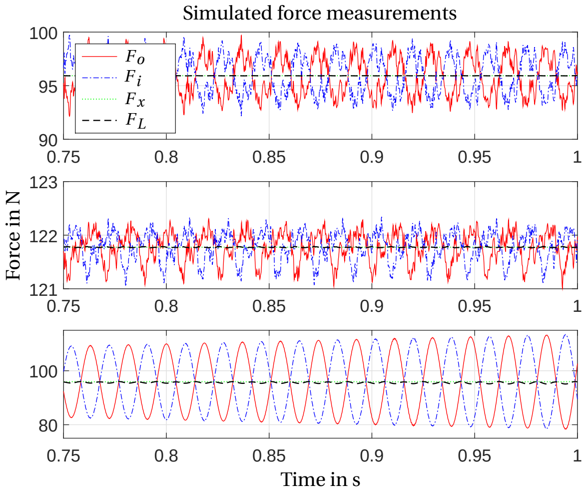

Figure 4.4: Simulated force measurements for three excitation cases. The three subplots respectively contain the heel strike, the end-stop collision when extending and the excitation at the first Eigenfrequency. The red solid lines are the output forces F_o as in (4.7), the blue dash-dotted lines are the input forces F_i as in (4.7), the green dotted lines are the measured forces via direct position data F_x, and the black dashed lines are the measured forces via inductance data F_L.

Table 4.2 gives the RMSDs and the maximum deviations of the force measurements for all conditions with respect to the massless spring assumption, for the simulations.

For the physical experiment, Figure 4.5 shows the force data of the LC and force estimates using the LDM over time, for three excitation frequencies: 4.5, 20.2 and 27.0 Hz. Figure 4.6 compares the RMSD and maximum difference between LC and LDM data (top) and the means and standard errors of all three measurement principles (bottom). The small frequency deviations in the second subplot facilitate clear reading of the error bars.

4.6. DISCUSSION

Results indicate that internal oscillations in coil springs increase the measurement uncertainty of sensors for spring force. However, typical position and force sensors have an uncertainty of about 0.2%. Table 4.2 shows that, in simulation, uncertainties due to internal oscillations not caused by harmonic excitation at a resonance frequency remain in the same order of magnitude. This holds true for all sensors, including the new sensing principle via inductance. In practice, the RMSD and maximum difference are larger, but still not exceeding 2 and 5%, respectively.

The differences between input and output forces confirm the well-known fact that in order to promote control stability when using a dedicated force sensor, such a sensor should preferably be placed at the motor side of the spring, avoiding non-collocated actuation and sensing [32].

The double set of data points in Figure 4.6 at 0 Hz quantifies the relaxation during the experiment. We consider it negligible as it remains within the sensors' uncertainty.

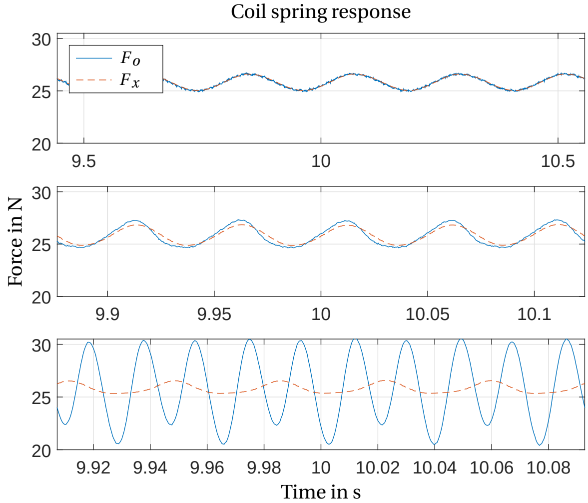

Figure 4.5: Raw force measurements from a load cell and a laser distance meter, for three excitations: 4.5, 20.2 and 27.0 Hz.

For inductance-based force sensing, an interesting observation can be made: nonuniform winding distribution results in a negative inductance bias. Nonuniformity, so local winding density variation, changes each winding's contribution to the total inductance. While this change can be both positive and negative, the inverse proportional influence on inductance lets the inductance increase exceed the magnitude of the decrease. A higher inductance compared to uniform distribution, on which the fit is based, makes the coil appear shorter than it actually is, resulting in a lower average force estimate. Both in simulation and the hardware experiment, the effect is clearly visible at harmonic excitation at half the first resonance frequency, as illustrated in Figure 4.6.

While the force differences between F_o and F_x are visible in the RMSD and maximum difference in Figure 4.6, the averaged values do not seem to differ. The inductance bias, however, is clearly visible at 27 Hz, when the first Eigenfrequency is being excited; averaging does not eliminate this bias. Future research could include measuring RMSD and maximum difference for inductance-based force sensing, using a faster inductance measuring device.

The simulation data and the data of the last subplot in Figure 4.5 clearly show a large contribution of Eigenfrequencies calculated by (4.3) in the LC signal.

Although the observation of the bias may be of theoretical value, any resonance-induced bias in inductance sensing with respect to direct deflection sensing is negligible compared to the difference between the forces at the input and at the output side of the spring. Once resonance effects are so strong that the two ends of the spring do not exhibit comparable forces, conventional force control as in a SEA has little meaning. Based on this experiment, resonance-induced differences between inductance-based and conventional deflection sensing have no practical relevance.

Another, general indication from this study is that hardware and control designers should not only avoid excitation of a device's structural resonance frequencies, but also

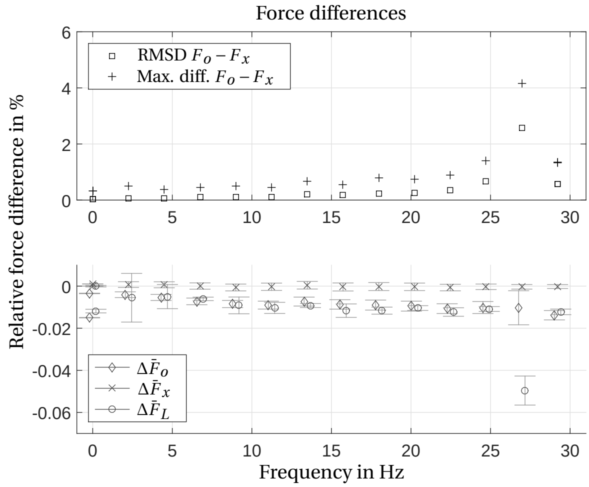

Figure 4.6: Relative force measurement performance from a LC F_O, LDM F_X and an inductance meter F_L. The first subplot indicates the difference over time between the LC and the LDM, in the form of the RMSD and the maximum difference. The second subplot gives the relative averaged force measurements $\Delta\bar{F}_O$, $\Delta\bar{F}_X$ and $\Delta\bar{F}_L$.

excitation of coil spring's own Eigenfrequencies in the system, at least if these springs are used for force sensing. Note that these Eigenfrequencies are not simply found by inverting (4.2), but from (4.3). Ways to mitigate oscillations in coil springs would be to purposefully introduce physical damping in the coil spring, for example by material choice or clamping conditions. Application of a low-pass filter on the control output, below the first Eigenfrequency of the coil spring, might help as well, but this reduces force control bandwidth. Notch filters or inverting the sensor model might be another option but would require specific knowledge on the used coil springs. In future work, we aim to identify and mitigate coil spring internal oscillation effects in a controlled system.

4.7. CONCLUSION

In this paper, we showed how collisions and resonance effects can affect force sensing in coil springs. We used a lumped-mass model to simulate such internal oscillations in the spring's axial direction, in three different practically relevant conditions. An experiment confirmed expectations for one condition.

First, results indicate that internal oscillations can result in notably different forces at either end points of the coil spring, and therefore increase the uncertainty of sensor readings. Second, the increase in uncertainty for each measurement method has the same order of magnitude as the measuring uncertainty under normal conditions. Third, the recently introduced inductance-based force sensing gives very similar results as sensing based on direct measurement of spring deflection. This is true even in the presence of large internal oscillations and non-uniformity of the windings.

Incorporation of this knowledge into design and control strategies of robots may increase their safety and reliability.

5

TCPM BACKGROUND

In 2014, Haines et al. introduced Twisted and Coiled Polymer Muscle (TCPM)s as "artificial muscles from fishing line and sewing thread" [49]. The invention found traction in multiple research groups, in various fields of research. This has resulted in a myriad of papers, creating the new field of twisted and coiled actuators. This chapter, however, limits its scope to thermally activated twisted and coiled nylon muscles. It first explains the working principle of the muscle. Next, it shows the state of the art of this field. Finally, it discusses research towards self-sensing of TCPMs done by others.

5.1. WORKING PRINCIPLE

The functionality of the TCPM depends on three things. First, it needs a highly directional substructure along the longitudinal axis, and an anisotropic thermal expansion. Second, twisting the fiber allows for torque generation. Third, coiling the twisted fiber converts torsional stroke in the fiber, into longitudinal stroke of a coil.

Extruding nylon to obtain nylon fiber aligns the polymer chains along the longitudinal axis of the fiber. This gives the nylon fiber its remarkably high tensile strength in the direction of the fiber, but it also affects thermal expansion. When heated, the fiber expands in radial direction, and it contracts in the axial direction. The former effect is regular thermal expansion, and the latter is attributed to entropic contraction of the polymer chains.

Insertion of twist levers the anisotropic thermal expansion for the working principle of the TCPM. Figure 5.1 illustrates this. Twist insertion wraps the polymer chains helically around the axis of the fiber. Heating of the twisted fiber will generate a torque to counteract the twist. In [48], Haines explains the so called *thermal torsion effect* as follows: let the polymer chains be represented by a string, tightly wrapped around a rod of fixed length, representing the fiber. If the rod increases in diameter, but the string does not change in length, it will generate a torque to unwrap the string. Similarly, if the rod is fixed in diameter, but the string shortens, it will again generate a torque to unwrap

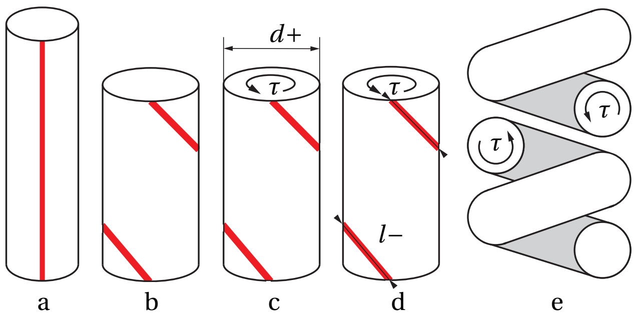

Figure 5.1: The working principle of twisted and coiled actuators. Subfigure (a) shows the precursor fiber, with the red line indicating the alignment of the polymer chains. Subfigure (b) shows the twisted fiber after annealing, so the fiber retains its shape. In this figure the polymer chains have obtained a helical orientation. Subfigures (c) and (d) respectively show the torque that results from increasing fiber diameter and from entropic contraction of the polymer chains. Subfigure (e) illustrates that a (homochiral) coil of twisted fiber contracts when heated.

the string. In general, this holds true for any oriented fiber in which the radial expansion exceeds the (untwisted) axial expansion [48]. Models based on this view are called single-helix approximations [16].

Coiling the twisted fiber turns the torsional actuator into a linear actuator. Love's treatise on elasticity relates deflection of a coil spring to (un)twisting of its constituent wire, and the corresponding torque in its cross section [48, 74, 80]. In the case where the chirality of coiling matches the chirality of the twist inserted in the wire (homochiral coiling) [49], the generated torque pulls the windings closer, thus contracting the coil, as illustrated in Figure 5.1.

There are two methods to coil the twisted fiber. The first method uses saturation of twist in the fiber. At a given point during twisting the fiber cannot contain anymore twist, and spontaneously starts to form coils by itself. Preventing untwist happens through thermal annealing or folding the twisted fiber in two, connecting the ends of the coiled fiber. This process results in auto-coiled or super-coiled muscles. The second method wraps the twisted fiber around a mandrel. Thermal annealing fixes the shape of the coil and prevents untwist. The majority of the studies in this field use the first method, with [122, 126, 143, 173, 184] and the work in this thesis as the exceptions.

5.2. State of the Art

Since 2014, research towards the TCPM sparked in several groups around the world. They investigate varieties in construction, heating and cooling methods, modeling, control methods, implementations and applications.

Many factors in construction and operation influence the final performance of a TCPM. The study in [123] shows the influence of speed of twist insertion, and [17] investigates the effects of annealing, training and moisture. Furthermore, [78] demonstrates remodeling of isotonic behavior through heat treatment. The work in [26] shows a 'preload knee' in the behavior of the muscle, and it shows that hysteresis losses decrease for higher temperatures. The study in [65] investigates the behavior of the muscle at a broad temperature range, including freezing. The authors of [88] investigate the isometric behavior of the muscle. The work in [126] shows the development of a machine to produce muscles with minimal human effort, to obtain a constant quality. Finally, the work in [15] proposes a method to test torque actuation, followed by a study in [16] investigating the influence of the amount of twist inserted, and the diameter of the fiber.

The next step is regulating the temperature of the muscle. The vast majority of researchers use Joule heating via a coating on the fiber [8, 9, 28, 40, 59, 62, 66, 83, 92, 114, 121, 123, 132, 135–137, 171, 172], a number use Joule heating via an additional resistance wire [10, 84, 97, 98, 128, 173], and some even use shape memory alloy [177, 179], creating a hybrid actuator. The work in [174] uses forced convective heating and cooling with water, and [144] uses convective heating with air. Finally, the study in [14] uses Peltier elements.

Several studies propose methods for modeling the TCPM. Both [130] and [178] take a multi-scale approach, i.e. they investigate mechanisms at the macro scale, the nano scale, and levels in between, to explain and model the behavior of the muscle. The study in [83] finds a nonlinear model for deflection and temperature via the energy balance. The work in [180] uses a spring-damper model to predict force, with a contribution of temperature in parallel. The authors of [16] use the single helix model to predict torsional actuation behavior. Furthermore, [81, 177, 183] have different approaches to model hysteresis. The study in [62] takes a phenomenological approach, and [97] uses a gray-box model. Finally, the work in [144] builds a finite element model to predict the generated torque in a twisted fiber.

A number of papers specifically investigates control methods for the TCPM's. The authors of [180] propose a lead compensator, based on the model they found. The work in [10] proposes PID control with a feedforward signal, and add controlled cooling by means of a fan in [140]. The study in [137] uses PID control, with anti-windup via backcalculation. Furthermore, in [138] the same authors propose 2-Degree of Freedom (DOF) PID control for muscles in an antagonist configuration. The work in [98] determines a feedforward signal through iterative learning, using the behavior of a PID controller in parallel. The study in [177] proposes integral-inverse control, to compensate for hysteresis. The authors of [84] apply a feedforward control signal based on inversion of the models they found in [83]. Finally, [59] proposes a Takagi–Sugeno–Kang fuzzy inference system to control force.

Next, several studies investigate implementations without a specific application in mind. The studies in [40, 98, 114, 138, 172, 177] propose an antagonist configuration, to be able to control both deflection and stiffness, or to improve their general performance. The authors of [134] propose active liquid cooling, in addition to Joule heating and an antagonist configuration, to further increase performance. The work in [66] puts muscles in a pennate configuration, to obtain variable stiffness. Finally, [132] investigates different weaving and braiding techniques, to embed TCPMs in textiles.

An array of applications illustrates the versatility of the TCPM. Robotic applications include fingers [28, 59, 174, 180, 181], an arm [183], a wrist orthosis [136], a hand orthosis [121], joints in general [40, 173], silicon manipulators [9], silicon skin for robotic facial expressions [8], a robot fish [114] and a tensegrity robot [171]. Other applications include energy harvesting [69], self-healing foam-composite panels [184], a thermostat [122] and a self-adjusting sports bra [135].

5.3. SENSING

Alongside this thesis, a number of studies have investigated (self-) sensing of TCPMs.

The authors of [3] derive a sensing model for an autocoiled nylon muscle, to have it act as a sensor. To that end, they model the resistance of the coated nylon via a phenomenological approach. They do this along the same lines as their work in [2]. Elongation of the coil results in a torque and untwist in the fiber, which they relate via Castigliano's Second Theorem. The changing geometry changes the resistance, which can be used for sensing purposes. This research lacks the inclusion of actuation, so it cannot be used as a self-sensing model. That could be obtained by including the influence of temperature on geometry, as in [2], and its influence on the resistivity of the coating.

The study in [175] investigates the change in resistance when actuating the muscle. They found nonlinearities when the muscle was heated. It appeared that the windings of the autocoiled muscles made contact at that point. This would suddenly lower the resistance. The contribution of this paper shows the possibility of self-sensing.

The work in [143] uses mandrel-coiled coated nylon muscles as a sensor in a silicon manipulator. They measure resistance and relate it to the bending angle of the manipulator.

The study in [50] investigates closed-loop temperature control of autocoiled muscles via self-sensing of resistance. They investigate the isometric force generation, and demonstrate position control with a constant load.

The authors of [142] determine the temperature of an autocoiled muscle via the resistance of its Joule-heating element. With a constant load, they relate the temperature of the muscle to its deflection. This enables them to perform closed-loop position control via self-sensing of temperature.

Finally, the work in [139] investigates self-sensing and control of the temperature of a twisted polymer fiber via resistance of a Joule-heating element. Subsequently, it demonstrates the closed-loop control of the rotational angle of the twisted fiber.

6

Self-Sensing of Deflection, Force and Temperature for Joule-Heated Twisted and Coiled Polymer Muscles via Electrical Impedance

Joost van der Weijde, Bram Smit, Michael Fritschi, Cornelis van de Kamp and Heike Vallery

The content of this chapter has been published in Transactions on Mechatronics (T-Mech) in June 2017.

ABSTRACT

The recently introduced Twisted and Coiled Polymer Muscle is an inexpensive and lightweight compliant actuator. Incorporation of the muscle in applications that rely on feedback creates the need for sensing of deflection and force. In this paper, we explore a sensing principle that does not require any bulky or expensive additional hardware: self-sensing via electrical impedance. To this end, we characterize the relation between electrical impedance on the one hand, and deflection, force and temperature on the other hand, for the Joule-heated version of this muscle. Investigation of the theoretical relations provides potential fit functions that are verified experimentally. Using these fit functions results in an average estimation error of 0.8%, 7.6% and 0.5% for estimating respectively deflection, force and temperature. This indicates the suitability of this self-sensing principle in the Joule-heated Twisted and Coiled Polymer Muscle.

6.1. INTRODUCTION

Compliant actuators are a popular area of research [57, 159]. Their inherently low mechanical impedance enables safe interaction with humans, other robots and an uncertain environment. In analogy to the human muscle, often represented by Hill-type models [169], artificial muscles are actuated compliant elements. Polymeric Artificial Muscles (PAMs) form one group within the variety of artificial muscles. Actuators based on Conductive Polymer (CP), Ionic Polymer-Metal Composite (IPMC) and Dielectric Elastomer, amongst others, constitute this group.

Within PAMs, the Twisted and Coiled Polymer Muscle (TCPM) [49] is a recent development. It is a thermally activated actuator in the form of a coil made of a twisted polymer fiber such as a nylon fishing line. Despite low speed and efficiency, this actuator is capable of high strain, high power- and work density [26] and good quality production is inexpensive [49].

Self-sensing actuators are a promising research direction to have truly collocated sensing [37] and to enable closed-loop controlled systems without increasing cost. Dosch and Inman coined the term in 1992 and applied the principle to a piezoelectric actuator [37]. Although a strict definition does not exist, systems are considered self-sensing when information on the state of the system is provided by reading input signal behavior, using a special input signal, or adding additional leads to existing hardware [70]. In general, self-sensing actuators make use of 'smart materials' [86] or 'smart structures' [60].

In PAMs, diverse types of self-sensing already exists: CP actuators consist of a conductive and nonconductive polymer structure placed in an electrolyte. A Faradaic process drives these actuators [82]. Changes in the physical, chemical or thermal domain effectively change the resistivity [70, 99]. A carbon-particle-containing version of this actuator, as presented in [141], works in the same way. IPMC actuators are structures of an ion-conducting polymer membrane coated with metal on either side, placed in deionized water. Ion migration due to application of an electrical potential drives these actuators. The nonuniform ion concentration affects the applied electrical potential [112]. An actuator related to the TCPM is the twisted carbon nanotube yarn actuator. It responds to heat. In [79], a layered version of this actuator measures strain due to changing capacity. In [76], a glucose-containing version of this actuator can sense temperature.

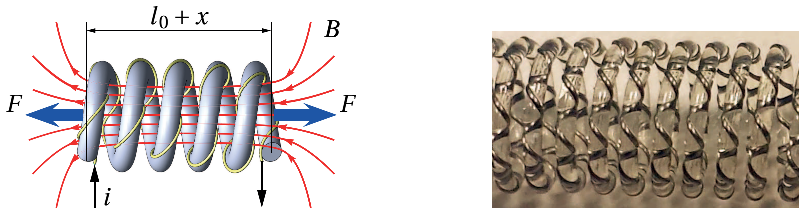

Figure 6.1: Electromechanical model of a Joule-heated TCPM (Figure 6.1a), and a close-up of an actual TCPM (Figure 6.1b). A metal wire wrapped around a polymer helix is the conductor for Joule heating. The muscle contracts when heated and has a substantial mechanical stiffness, so a force F results from a temperature change or a deflection x. The metal wire has an inductance, so a magnetic flux B results from a change in current i through the wire. The wire's resistance changes with temperature. Therefore, the electrical impedance of the muscle provides information on the mechanical state.

To date, feedback controlled systems with TCPMs still rely on conventional sensing methods for information on their state. Existing applications use encoders [180] and laser distance meters [10] to provide position feedback, and load cells [180] to provide force feedback. Next to these solutions we can imagine the use of linear potentiometers, hall sensors and thermocouples to provide feedback when applying TCPMs. The cost of these sensors range from around 1 euro to upwards of 1.000 euro's. Adding the previous solutions to TCPMs increases their weight, size and cost disproportionately. This makes development of self-sensing in TCPMs a priority.

In this paper, we introduce self-sensing for Joule-heated TCPMs. Following up on our work in [156], we make use of the macroscopic resemblance between helical springs and solenoid coils, illustrated in Figure 6.1. We characterize a relation between deflection, force and temperature on the one hand and electrical impedance (inductance and resistance) on the other hand. In this first proof of principle, we disregard time-dependent behavior. We evaluate the relation both in theory and in practical experiments, demonstrating usability for sensing.

Section 6.2 introduces the TCPM and its production in more detail. Section 6.3 contains the derivation of theoretical relations between inductance and resistance on the one hand, and deflection, force and temperature on the other hand. Section 6.4 describes the experiment used to investigate the usability of these relations for sensing. Section 6.5 presents the results, followed by the discussion in Section 6.6 and the conclusion in Section 6.7.

6.2. THE MUSCLE

This section introduces the working principle of the TCPM, followed by its construction method in general.

6.2.1. WORKING PRINCIPLE

As explained in [49] two principles form the base of the TCPM's functionality. The first principle is a negative thermal expansion in the axial direction, caused by what in rubbers is known as the entropic effect [30]: when heated, highly drawn polymeric fibers access conformational entropy providing reversible contractions. The second principle is the amplification of stroke: inserting twist into the polymer fiber amplifies the tensile stroke. The TCPM is a coil made from this highly twisted fiber. A number of parameters determines the achievable stroke and load capacity, for example: precursor-fiber dimensions and material, number of twists, load while twisting and coil diameter.

Application of heat drives the TCPM. Although a number of methods exist [26, 49, 92, 180], the simplest application oriented method is Joule heating with a resistance wire. Wrapping the resistance wire around the polymer, as illustrated in Figure 6.1, distributes contact of the wire with the polymer over the muscle. Passing a current through the resistance wire heats up the wire and subsequently the polymer.

6.2.2. TWIST INSERTION AND INCORPORATION OF THE RESISTANCE WIRE

The construction of the TCPM with Joule heating via a resistance wire follows the method in [10, 49]. We start with aligning a polymer precursor fiber with an equal length of the resistance wire. We jointly clamp one end to a rotational motor. A weight is fixed to the other end using a tether and a system of pulleys, such that it applies a constant load on the fiber under influence of gravity. Rotation of the motor inserts twist. Blocking rotation of the tether prevents the wires from untwisting, while the applied load prevents the wire from snarling. When coils start forming spontaneously (cf. nucleation of coiling or auto coiling [49]), the fiber has reached maximum twist density. At this point we stop twist insertion.

The physical connection between the resistance wire and the polymer fiber has to be reliable in order to achieve repeatable actuation and sensing. As a consequence of the twist insertion process, the resistance wire is automatically wrapped around the thickening polymer fiber and tightened, partly embedding itself in the polymer.

6.2.3. MANDREL COILING AND THERMAL ANNEALING

Guiding the resistance-wire-wrapped precursor fiber around a mandrel forms the TCPM. This is done under the same load as the twist insertion process. The ends of the mandrel are manufactured such that the wire's ends line up in the middle of the coil. Mandrel coiling is done such that a homochiral TCPM results [49]. Mandrel formed coils require thermal annealing to retain their shape when taken off the mandrel. Our TCPMs are annealed for one hour at 175 °C in a conventional oven.

6.2.4. TRAINING

Training of the muscle is usually seen as repeating the actuation cycle in the setup a number of times before performing the actual experiment [15, 26, 92]. We let muscles undergo a number of cycles of heating and cooling, from room temperature to the maximum actuation temperature, in the intended setup. When the muscle shows repeatable temperature-force behavior, we consider it trained. Pilot experiments have shown that the muscles show repeatable temperature-force behavior within six training cycles, with a maximum actuation temperature of 120 °C.

6.3. Self-Sensing Model Derivation

TCPMs could be considered actuated coil springs. Also, TCPMs with Joule heating contain conductive material. Therefore, our reasoning in [156] can be extended to TCPMs: A TCPM's electrical impedance changes with deflection, force and temperature. In a dynamic application, these state variables are highly coupled with each other. Only two are required to fully describe the TCPM's behavior. We assume that in a quasi-static case temperature and deflection are independent, and that force is a function of these two. This section characterizes the dependencies of inductance and resistance on temperature and deflection. We solve the two independent equations to find expressions for deflection and temperature, with inductance and resistance as input. Finally, we find an expression for force dependent on deflection and temperature.

6.3.1. Inductance

Several models exist to describe inductance L of coils. The simplest form is

$$L = \mu_0 \frac{N^2}{l} \pi r^2, \tag{6.1}$$

for example given in [127]. It depends on the magnetic permeability μ_0, the number of windings N, the length l and the radius r of the coil. This equation assumes homogeneity of the magnetic field inside the coil, and it neglects flux leakage. Adaptations of (6.1) are introduced in [95, 118] to improve the accuracy of this model. Maxwell provided another approach in [85], by summing the self- and mutual inductances of the individual windings in a coil. Neumann's equation [45] provides the supposedly most accurate model, but requires computation of line- or volume integrals. A more thorough comparison of these inductance theories can be found in [156].

When investigating the relation between coil length and inductance, it becomes apparent that all models show inverse proportional behavior with an offset. In practice, theoretical and actual inductance differ. Recently we showed that a fitting relation with two parameters

$$L(x) = \frac{\lambda_l}{x + l_0} + \lambda_o \tag{6.2}$$

6

performs adequately for deflection sensing of coil springs [156]. Herein, x is the deflection, and l_0 the known rest length of the spring. The two parameters λ_l and λ_o can be determined using a least-squares fit using minimally two data points of $L(x)$.

For the metal coil springs of [156], this fit suffices to estimate deflection or force. In the TCPM, however, this fit function does not suffice. Heat drives the system by changing the geometry and properties of the material. A pilot experiment has shown that an increase in temperature gives an offset to the inductance. Therefore, we add temperature T and a parameter λ_T to (6.2), resulting in

$$L(x, T) = \frac{\lambda_l}{x + l_0} + \lambda_T T + \lambda_o. \tag{6.3}$$

6.3.2. RESISTANCE

An increase in temperature typically increases the resistance of conductors. For the temperature differences under consideration the linear approximation

$$R(T) = R_0\left(1 + \kappa\left(T - T_0\right)\right) \tag{6.4}$$

suffices [127]. In this approximation, the actual resistance of the conductor R depends on the resistance R_0 at a known temperature T_0, the current temperature T and the temperature coefficient κ.

Another influence on resistance is deflection of the muscle. This in- or decreases the strain on the Joule-heating wire. Like a common strain gauge, this influences the resistance. A pilot experiment has shown that an increase in deflection, decreases the resistance.

We assume that these influences and possible other influences caused by temperature and deflection are linear and additive. The equation

$$R(x, T) = \rho_x x + \rho_T T + \rho_o, \tag{6.5}$$

with ρ_x, ρ_T and ρ_o as fitted parameters, describes the dependency of resistance on deflection and temperature.

6.3.3. ESTIMATION OF TEMPERATURE, DEFLECTION AND FORCE FROM INDUCTANCE AND RESISTANCE

For self-sensing purposes, the above relations for inductance and resistance need to be solved for temperature and deflection. In turn, force depends on both temperature and deflection.

Solving the two independent equations (6.3) and (6.5) for their inputs T and x gives two nonlinear equations

$$T(L, R) = \frac{R\lambda_T + L\rho_T - \lambda_T\rho_o - \lambda_o\rho_T + \lambda_T\rho_x l_0 + \sqrt{D}}{2\lambda_T\rho_T}, \tag{6.6}$$

and

$$x(L, R) = \frac{R\lambda_T - L\rho_T - \lambda_T\rho_o + \lambda_o\rho_T - \lambda_T\rho_x l_0 + \sqrt{D}}{2\lambda_T\rho_x}, \tag{6.7}$$

with

$$\begin{aligned} D = {} & \left(L\rho_T - R\lambda_T - \lambda_T\rho_x l_0 + \lambda_T\rho_o - \lambda_o\rho_T\right)^2 \\ & + 4\lambda_l\lambda_T\rho_x\rho_T, \end{aligned} \tag{6.8}$$

both containing the six presented parameters that need to be identified.

Currently existing models for the TCPM let the force depend linearly on actual deflection and a difference in rest length due to thermal activation [65, 130, 180]. Although cross terms might increase the accuracy of the model, in this paper we chose to follow the linear relation

$$F(x, T) = \phi_x x + \phi_T T + \phi_o, \tag{6.9}$$

with ϕ_x, ϕ_T and ϕ_o as parameters that need to be identified.

Table 6.1: Muscle Construction Specifications

Property	Value
precursor fiber diameter	0.6 mm
precursor fiber material	nylon
resistance wire diameter	0.2 mm
resistance wire material	iron
twist per initial fiber length	≈ 400 rotations/m
load at twisting	≈ 3.00 N
mandrel diameter	5 mm
mandrel length	50 mm
annealing temperature	175 °C
annealing time	1 hour
nr. of windings	51
training temperature	120 °C
nr. training cycles	6

6.4. EXPERIMENT

This section describes the experiment to validate the fit functions introduced in the previous section, including muscle construction, experimental protocol and data analysis.

6.4.1. MUSCLE CONSTRUCTION AND MATERIAL CHOICE

The muscle was fabricated according to the method in Sections 6.2.2, 6.2.3 and 6.2.4, with the specifications in Table 6.1. A table-mounted drill functioned as the motor. The number of revolutions was counted by an Arduino Uno, reading a hall sensor that was triggered by a permanent magnet attached to the head of the drill. Regarding the precursor fiber, we chose transparent nylon fishing line from *midnight moon* with a diameter of 0.6 mm. The resulting muscle had a rest length after training of 61 mm.

The resistance wire has a dual purpose as it generally serves as the Joule-heating element and here as the probe for self-sensing of temperature, deflection and force. We therefore chose an iron resistance wire with a diameter of 0.2 mm. The temperature coefficient of iron is $\kappa = 6.41 \cdot 10^{-3}\,^{\circ}\mathrm{C}^{-1}$. Equation (6.4) shows that with a temperature difference of for example 70 °C, the resistance should change about 45%.

6.4.2. EXPERIMENTAL SETUP

Verification of the fit functions required data on temperature, deflection, force, inductance and resistance. Parts of the data were used for fitting, the other parts were used for verification.

We used a *Zwick Z005* Universal Testing Machine (UTM) with heating chamber to control and/or measure temperature, deflection and force. The heating chamber allowed us to achieve a fully homogeneous temperature distribution in the muscle. The positioning uncertainty of the UTM is 2 μm. The relative uncertainty of the 1 kN loadcell is 0.35% at 0.2% of its capacity, i.e. an uncertainty of at most 7 mN. The temperature uncertainty of the sensor is 0.5 °C.

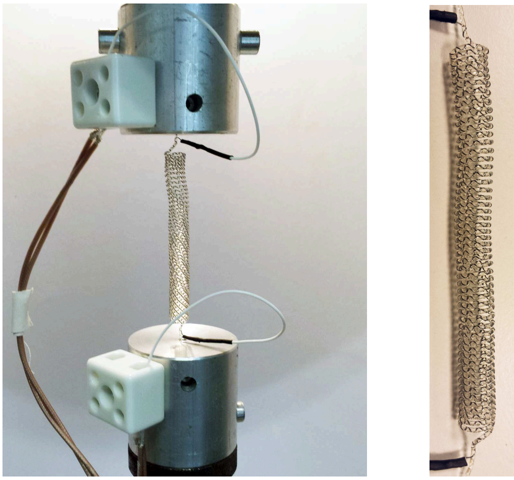

(a) (b)

Figure 6.2: Illustration of the measurement setup. Figure 6.2a shows the TCPM in the UTM with four-point measuring cables attached, leading to the LCR43100. Figure 6.2b shows a close-up of the TCPM.

An LCR43100 by *Wayne Kerr* measured the inductance and resistance via four *RG-178B/U* coax cables of 1 m, which allowed for measurements inside the heating chamber. Figure 6.2 illustrates the setup and the TCPM in practice.

The measurement-signal frequency of the LCR43100 was based on a pilot experiment. This experiment determined the order of magnitude of resistance and inductance. The signal frequency was set such that the real and imaginary part of the electrical impedance were of approximately the same order of magnitude, with an acceptable measuring uncertainty. With the order of magnitude of resistance and inductance at respectively 10 Ω and 5 μH, a signal frequency of 0.5 MHz resulted. The relative accuracy of the LCR43100 with this configuration is 0.5%. We neglect a possible influence of the measuring signal on the temperature of the muscle.

6.4.3. PROTOCOL

For this experiment, the UTM controlled temperature and deflection, and measured force. In a pilot experiment, the TCPM showed unexpected deformations at large deflections and at 120 °C, which is a conventional temperature for actuation [26, 174, 180]. The windings of the muscle slanted, such that the muscle no longer resembled a coil. When this happened, the muscle was not functional anymore. Therefore, we chose a uniform temperature distribution with seven points, ranging from 50 °C to 110 °C. At each temperature a series of 15 extending and subsequently 15 retracting steps was applied. The deflection ranged from 2 to 30 mm. The UTM extended and retracted at approximately 15 mm/min. Figure 6.3 illustrates the sequence of deflection steps, and the division between fitting and verification steps. The UTM logged data at approximately 10 Hz.

The UTM maintained each deflection step for 15 seconds. This allowed the LCR43100 to measure inductance and resistance. A Matlab script was used to time, and subse-

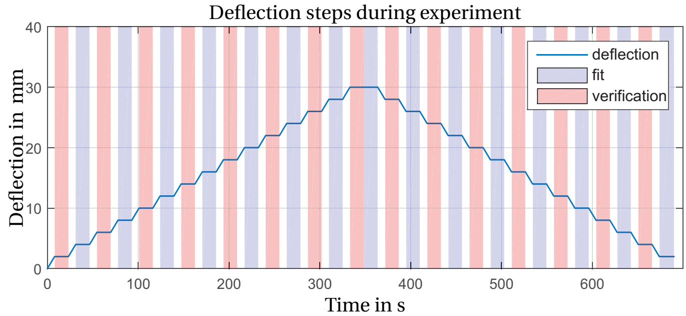

Figure 6.3: The deflection steps taken during the experiment for one reference temperature, once the heating chamber had reached that temperature. The blue and red ribbons indicate which data was used for respectively fitting and verification.

quently trigger and record ten measurements via a serial connection, at each deflection step. A single measurement took approximately 0.8 seconds. The ambient temperature at the start of the experiment was 23 °C.

In more detail the protocol was as follows. After training the muscle in the UTM, we calibrated the LCR43100 with the measurement cables connected, to account for their flux area. The trained muscle was then fixed to the top clamp. Suspended from its own weight, the bottom clamp was attached, after which the UTM deflection and force was set to zero. For each reference temperature, the UTM ramped to the temperature, after which the extension/retraction sequence was triggered automatically, and we manually triggered the LCR43100 measuring script. After each sequence the heating chamber was opened and cooled with forced convection for about 5 minutes.

6.4.4. DATA PROCESSING

The LCR43100 provided measurements that relate to a reference deflection at a reference temperature. The UTM provided measurements of temperature, deflection and force related to time. The time intervals where the UTM held its position were indicated by the first and last instants where the deflection deviated less than 1 µm from its reference. Only data within these intervals was used for processing.

The means and standard deviations of all controlled and measured variables were calculated per deflection step. The relative standard deviation was calculated by dividing the absolute standard deviation by the difference between the maximum and minimum mean value of the variable over all data points.

The means and standard deviations provided discretized data points for fitting and verification. The order of the points was based on the moment of measuring. Following this order, the even-numbered mean values were collected in the vectors R_f, L_f, T_f, x_f and F_f, and were used for fitting. The odd-numbered mean values were collected in the vectors R_v, L_v, T_v, x_v and F_v, and were used for verification. Figure 6.3 illustrates this division.

6.4.5. DATA ANALYSIS

The coefficients of (6.3) and (6.5) resulted from a least-squares fit, respectively minimizing the errors with respect to the vectors L_f and R_f, with x_f and T_f as input. We used these coefficients as the initial condition for a nonlinear least-squares optimization with the trust-region-reflective algorithm, to minimize V, given by

$$\begin{aligned} V = \sum \left(v_1\left(T(L_f, R_f) - T_f\right)\right)^2 \\ + \left(v_2\left(x(L_f, R_f) - x_f\right)\right)^2, \end{aligned} \tag{6.10}$$

in which the weighing factors $v_1 = {}^1/_{110}\,°\mathrm{C}^{-1}$ and $v_2 = {}^1/_{30}\,\mathrm{mm}^{-1}$. The coefficients of the fit function for force in (6.9) were determined by a least-squares fit with the vectors x_f, T_f, minimizing the error with respect to F_f.

Using the entries of L_v and R_v as input for (6.6) and (6.7) respectively gave estimates on temperature $\hat{T}$ and deflection $\hat{x}$. These estimates served as an input for (6.9) to estimate force $\hat{F}$.

Comparing the estimates $\hat{T}$, $\hat{x}$ and $\hat{F}$ with the measured values in T_v, x_v and F_v determined the quality of the fit. We used two measures to evaluate the estimation quality. First the R^2 value, or variance explained, measured the quality of fit. It is defined as

$$R^2 = 1 - \frac{\sum_{i=1}^{n}(y_i - f_i)^2}{\sum_{i=1}^{n}(y_i - \bar{y})^2}, \tag{6.11}$$

in which y_i are the n data points with $\bar{y}$ as their mean, and f_i the estimates. Secondly, the Root Mean Square Error (RMSE) quantified the estimation error. Comparing the RMSE of the estimates with the standard deviations of the measurements showed the reliability of the fit compared to direct measurements.The relative RMSE was calculated by dividing the absolute RMSE by the difference between the maximum and minimum measured value of the corresponding variable. The relative RMSE illustrated the magnitude of the error compared to the interval of interest.

A fit with predicted isothermal, isometric and isotonic lines illustrated the mapping from inductance and resistance to respectively temperature, deflection and force. The vectors L^* and R^* were generated inputs for inductance and resistance. They consisted of fifty equidistant points between the respective minimum and maximum measured values. Equations (6.6), (6.7) and (6.9) provided the outcomes T^*, x^* and F^*.

6.5. RESULTS

Table 6.2 shows the minimum and maximum measured values of inductance, resistance, temperature, deflection and force. These measurement interval values were used to calculate the relative standard deviations and relative RMSE's. Table 6.2 also shows the maximum standard deviations σ for the measured data over all deflection steps and desired temperatures, both as an absolute and a relative value. They indicate the precision of the used instruments and protocol.

Figure 6.4a shows the fits for deflection, force and temperature with inductance and resistance as input variables. The dashed lines are the predicted isometric lines of the deflection fit, the solid lines are the predicted isotonic lines of the force fit and the dotted

Table 6.2: Interval of measured inductance, resistance, temperature, deflection and force and the maximum standard deviations σ over a deflection step.

	min	max	σ absolute	σ relative
L	4.254 µH	5.261 µH	0.001 µH	0.1%
R	10.091 Ω	12.083 Ω	0.004 Ω	0.2%
T	50.0 °C	110.0 °C	0.5 °C	0.8%
x	2.000 mm	30.000 mm	0.000 mm	0.0%
F	0.05 N	0.79 N	0.01 N	2.0%

lines are the predicted isothermal lines of the temperature fit. The labels of the iso lines are respectively in mm, N and °C.

Figure 6.4b shows the estimated deflection $\hat{x}$ at the corresponding measured deflection x_v. Figure 6.4c shows the estimated force $\hat{F}$ at the corresponding measured force F_v. Figure 6.4d shows the estimated temperature $\hat{T}$ at the corresponding measured temperature T_v. In these figures, the circles indicate the data points for extension and the crosses indicate the data points for retraction. The red solid lines that bisect these figures, indicate the perfect values.

Table 6.3 shows the fit-quality measures. Comparing the absolute and relative RMSE to respectively the absolute and relative standard deviations of T, x and F in Table 6.2 indicates the difference in quality between estimating and measuring these variables.

Table 6.4 shows the fitting parameters for (6.3) and (6.5), used in (6.6), and (6.7) to respectively estimate temperature and deflection, and the fitting parameters for force in (6.9).

6.6. DISCUSSION

The paper aimed at determining the usability of a static relation between electrical and mechanical properties of a Joule-heated TCPM. This paper took inductance and resistance as the relevant electrical properties to measure, deflection and force as the mechanical state to estimate, and temperature as a relevant intermediate variable. For the investigated TCPM, estimation results showed an RMSE of 0.8% for deflection, 7.6% for force and 0.5% for temperature. More mature sensing solutions for deflection, with a similar range, typically have an uncertainty in the order of magnitude of 0.2%. For existing temperature sensors that is typically around 0.5%, and for force also around 0.2%. Compared to these more mature solutions, self-sensing of deflection and temperature already approaches those uncertainties. However, force sensing is still far away from those solutions.

Deflection was measured and tracked very accurately, as indicated by the negligible variance. The RMSE can therefore be attributed to the fit function and realization of the muscle.

The slanting of the isometric lines in Figure 6.4a shows the influence of temperature on inductance of the muscle. This implies that deflection sensing in TCPM should not rely on inductance only, in contrast to metal coil springs [156].

The RMSE of the force estimate is almost four times the maximum variance within a

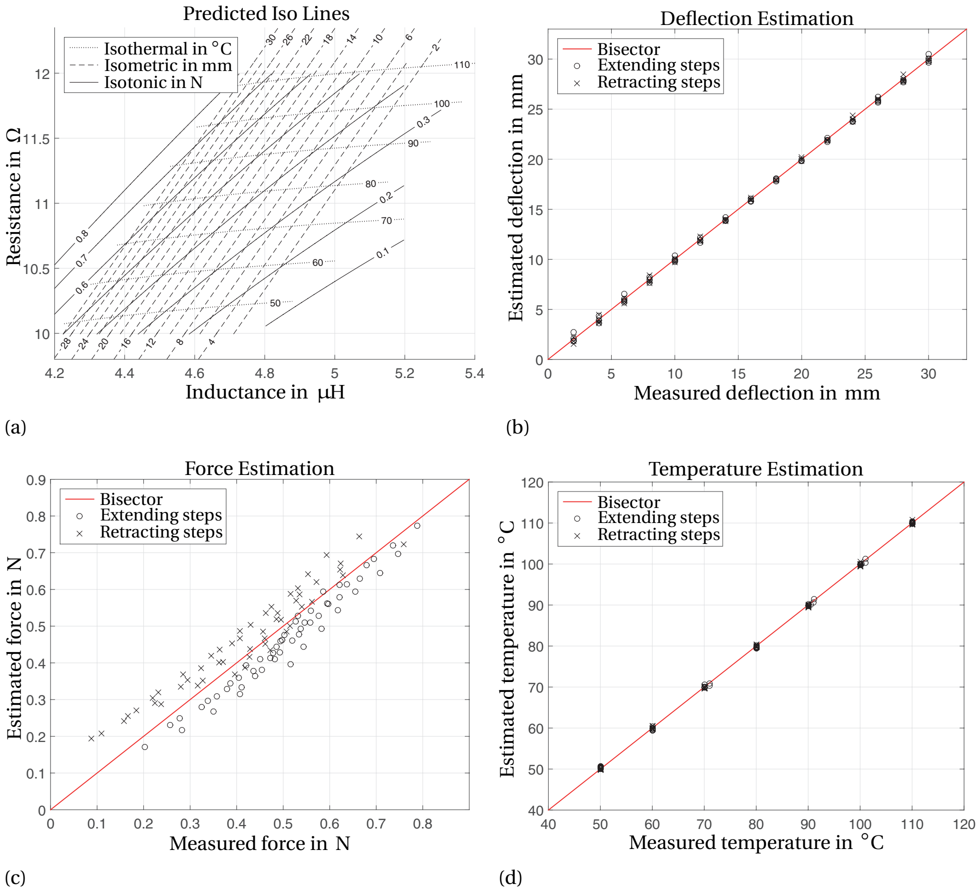

Figure 6.4: Graphic representation of fit and verification. Figure 6.4a shows the fit for deflection x^*, force F^* and temperature T^*, with inductance L^* and resistance R^* as input. The dashed, solid and dotted lines are respectively the predicted isometric, isotonic and isothermal lines of the fit functions. The labels of the iso lines are respectively in mm, N and °C. Please note that, although the experimental conditions are similar, the iso lines are predictions based on the fitted parameters. Figure 6.4b shows the estimated deflection $\hat{x}$, using inductance and resistance as input, versus the measured deflection x_v. The extending steps are indicated by circles, the retracting steps are indicated by crosses. The solid red bisector indicates the perfect value. Figure 6.4c shows the estimated force $\hat{F}$, using estimated deflection and temperature as input, versus the measured force F_v. The extending steps are indicated by circles, the retracting steps are indicated by crosses. The solid red line indicates the perfect value. Figure 6.4d the estimated temperature $\hat{T}$, using inductance and resistance data as input, versus the measured temperature T_v. The extending steps are indicated by circles, the retracting steps are indicated by crosses. The solid red line indicates the perfect value.

Table 6.3: Fit quality measures for temperature, deflection and length

	R^2	RMSE absolute	RMSE relative
T	1.000	0.3 °C	0.5%
x	0.999	0.23 mm	0.8%
F	0.854	0.06 N	7.6%

Table 6.4: Fitted parameters for (6.3), (6.5) and (6.9).

	$L(x,T)$		$R(x,T)$		$F(x,T)$
λ_l	107.429 μH.mm	ρ_x	-0.005 Ω/mm	ϕ_x	0.013 N/mm
λ_T	0.008 μH/°C	ρ_T	0.030 Ω/°C	ϕ_T	0.004 N/°C
λ_0	2.670 μH	ρ_0	8.717 Ω	ϕ_0	-0.075 N

deflection step. A remarkable feature in Figure 6.4c is that the force estimates while extending were generally underestimated and while retracting overestimated. Both might be explained by time-dependent behavior. Although we disregarded it in the fit function descriptions and data processing, in practice we did encounter the effects. Spectral analysis of the force data indicated that frequency content above 2 Hz had an amplitude lower than the 7 mN uncertainty of the load cell. For a short analysis of the low frequency behavior, we filtered the force measurements with a 2 Hz lowpass filter. This revealed a 30 mN force variation during measurements within a step, which is 4.1% of the force interval. The maximum hysteresis over a full deflection sequence was 149 mN. These values also explain the high variance and RMSE of force estimation.

The variance and RMSE of the estimate of temperature were comparable, so for estimation of temperature the relation with electrical properties is as reliable as a ground truth measurement with a standard temperature sensor. Figure 6.4a shows that temperature mainly relates to resistance. However, since resistance also changes with deflection, including inductance in the fit function improves the estimates.

In Figure 6.4d some temperature measurements deviate from the reference temperature. The deviations occurred at the initial steps of the respective measurement series. This deviation is due to the quantization of the temperature sensor in, and tracking inaccuracy of the heating chamber. This does not invalidate the data points, and it does not seem to influence the fit.

Implementations of the muscle will involve dynamic behavior. Currently, any damping is disregarded. The estimation principle should therefore be validated in a dynamic setting. Overall, temperature and deflection can be estimated accurately and precisely with only 6 parameters in time-independent relations. Force estimates should be improved by taking time-dependent behavior into account, for example as in [101]. Moreover, if the application of the TCPM is known, the fit functions could possibly be simplified by including system behavior.

This paper did not investigate the repeatability of these measurements within a muscle, nor did it investigate the repeatability between muscles. Future research towards both will indicate the universality of the fit functions. We expect that the repeatability within a muscle strongly depends on the repeatability of the mechanical behavior of the TCPMs and the effectiveness of the training process, which relates to their time-dependent behavior. This holds particularly for force. Therefore, investigation of this repeatability requires knowledge on creep, relaxation and other time-dependent effects. We expect that the repeatability between muscles strongly depends on the repeatability in production and training. Investigation hereof therefore requires knowledge on the repeatability of production and training.

A more detailed investigation on the influence of deflection and temperature on geometry and properties of the muscle might result in a more appropriate form of the fit function. Future work towards this aspect might improve the universality of the fit functions.

Furthermore, a change in the training procedure, for example training at different loads, might result in a different relation between temperature, deflection and force. This would also affect the universality of the fit. Therefore, future research should also be directed towards the effects of training.

The current work is a proof of principle regarding self-sensing of Joule-heated TCPMs using their electrical impedance. We used a commercially available LCR meter and a heating chamber. When the principle is applied, the characterization should happen under conditions close to their application and with the measurement device used in the application. To that end, future work firstly aims at developing a practical combination of actuation and sensing. Preliminary design indicates that the required electronics for combined actuation and sensing will not exceed the size and cost of available methods, and eliminates the need to incorporate the sensor in the kinematic chain. Future work will include a detailed design for such electronics and comparison of its performance to existing sensing solutions for deflection and force. Secondly, future work will combine modeling of the (thermo)dynamic behavior with the presented sensing principle, and validating the current static relations in a dynamic setting. Moreover, time-dependent behavior will be included in the fitting relations, likely improving estimation of deflection and force. Finally, future work will study the degradation of the muscles over their lifetime. For example, these studies should investigate how factors like operation time and overloading degrade the muscle.

6.7. CONCLUSION

In this paper, we introduced self-sensing for Joule-heated TCPMs. We showed that deflection, force and temperature of such a muscle can be estimated with high precision and accuracy from measurements on the system's inductance and resistance. The theoretically derived forms of static relations between the state of the muscle and its electrical impedance were validated by experiments. The relations resulted in an average estimation error of 0.8% for deflection, 7.6% for force and 0.5% for temperature. This paper enables the incorporation of these inexpensive lightweight actuators in applications that require feedback, without the need of additional expensive sensor hardware.

7

Closed-Loop Control Through Self-Sensing of a Joule-Heated Twisted and Coiled Polymer Muscle

Joost van der Weijde, Heike Vallery, and Robert Babuška

The content of this chapter has been published in Soft Robotics (SoRo) in October 2019.

ABSTRACT

The twisted and coiled polymer muscle has two major benefits: low weight and low cost. Therefore, this new type of actuator is increasingly used in robotic applications where these benefits are relevant. Closed-loop control of these muscles, however, requires additional sensors that add weight and cost, negating the muscles' intrinsic benefits. Self-sensing enables feedback without added sensors. In this paper, we investigate the feasibility of using self-sensing in closed-loop control of a Joule-heated muscle. We use a hardware module capable of driving the muscle, and simultaneously providing sensor measurements based on inductance. A mathematical model relates the measurements to the deflection. In combination with a simple force model, we can estimate both deflection and force, and control either of them. For a muscle that operates within deflections of [10,30] mm and forces of [0.32,0.51] N, our self-sensing method exhibited a 95% confidence interval of 2.14 mm around a mean estimation error of -0.27 mm and 29.0 mN around a mean estimation error of 7.5 mN, for the estimation of respectively deflection and force. We conclude that self-sensing in closed-loop control of Joule-heated twisted and coiled polymer muscles is feasible and may facilitate further deployment of such actuators in applications where low cost and weight are critical.

7.1. INTRODUCTION

The recently developed actuation principle represented by the Twisted and Coiled Polymer Muscle (TCPM) has a number of benefits that make it interesting for application in soft robotics [49]. Two major benefits are its low weight and low cost. The working principle of this actuator is based on the thermal torsion effect [48]. Twisting a fiber with a substructure highly aligned in the direction of the fiber, such as polymer chains or carbon nanotubes, results in a helically aligned substructure. Radial expansion of the twisted fiber and entropic contraction of the helical substructure generate a torque in the opposite direction of the twist. In nylon, both effects can be induced through heating. These torsional actuators become linear actuators through coiling [48, 74].

Of the varieties of the TCPM, the thermally-activated Joule-heated nylon muscle receives the most attention. This specific type already has a wide range of applications: robotic fingers [28, 59, 180], joints [40, 173, 183], orthoses [121, 136], complete robots [114, 171], or being embedded in a silicon manipulator [9], silicon skin for robotic facial expressions [8], or a self-adjusting sports bra [135].

Systems that benefit most from TCPMs are typically lightweight and inexpensive, and should function in environments with varying conditions. However, most TCPM control schemes rely either on added sensors to enable feedback control [10, 28, 40, 59, 98, 138, 174, 180], or on predictable circumstances to enable feedforward control [84]. Added sensors increase weight and cost, negating two major benefits of these actuators. Accurate feedforward control requires a controlled environment, which limits its usability in real-life applications. One way to enjoy the benefits of TCPMs without the drawbacks of added sensors or complex models is through self-sensing. This means that a system determines its state through the interpretation of input-signal behavior, use of special input signals, or connecting additional electrical leads to existing hardware [70]. Self-sensing in TCPMs will provide an inexpensive and light-weight way to implement feedback.

TCPMs with Joule heating possess self-sensing capabilities, as we demonstrate in our previous work [155]. We show the potential to use both resistance and inductance of heating wires for self-sensing purposes. Next to our work, three studies on sensing in TCPMs focus on modeling the resistance of coated nylon muscles [3, 143, 175]. Two of these works use auto-coiled muscles [3, 175]. The first work contributes a phenomenological approach to derive a sensing model [3]. They relate resistance of a coated fiber to geometric changes during stretching of the coil. However, this approach does not include actuation, and therefore cannot be applied as a self-sensing model. The second work contributes an analysis of the resistance when actuating the muscle [175]. The authors found nonlinearities in the resistance attributed to coil windings making contact with each other. The third study uses mandrel-coiled muscles embedded in a silicon manipulator [143]. The authors use the muscles purely as sensors, instead of actuators, and propose a fourth-order polynomial fit as measurement model. Although these contributions demonstrate the capability for self-sensing, none use self-sensing to close the feedback loop.

In this article we close the feedback loop via self-sensing. We first identify and validate parameters for two models: one model to estimate deflection via the muscle's inductance, and another model to estimate force, with as inputs the power and the estimated deflection. Second, with the models applied, we implement a feedback loop through self-sensing, and perform simple control tasks, as illustrated by Figure 7.1.

We start with an explanation of the methods. The subsequent section contains the experimental validation of our methods. Next, we present the results of the experiments. Finally, we discuss our work and provide conclusions.

7.2. SELF-SENSING AND CONTROL METHODS

We first describe the hardware that combines actuation and sensing. Next, we introduce the models used for self-sensing of deflection and estimation of force, as well as their online implementations. Finally, we introduce the control method.

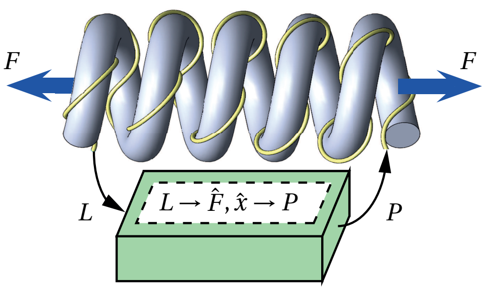

Figure 7.1: Impression of a self-sensing muscle. A control signal P is used to both drive the muscle to generate the force F and measure the inductance L of the Joule-heating wire. Based on the measurement and the previous control input, the self-sensing and control module estimates the force $\hat{F}$ and deflection $\hat{x}$, and subsequently determines the new control signal.

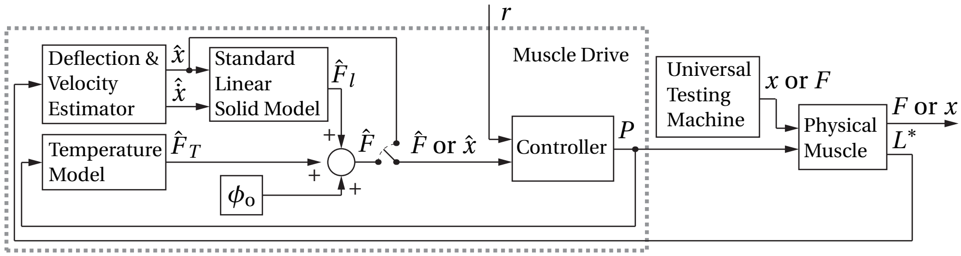

Figure 7.2: Block diagram for estimation and control. The gray dashed rectangle contains the functionality of the Muscle Drive (MD). Within the MD, the switch indicates that either the deflection estimate $\hat{x}$ or the force estimate $\hat{F}$ is used as input for the controller, alongside reference r, resulting in either control of deflection x or force F. The Universal Testing Machine (UTM) acts as a load on the muscle. When the MD controls force, the UTM imposes deflection, and vice versa. The temperature model uses power input P to compute the contribution of temperature to force $\hat{F}_T$, as in (7.1). The deflection and velocity estimator represents the measurement of deflection based on decay time L^* in (7.4), the subsequent low-pass filtering of the deflection measurement, and taking the backward difference to find velocity $\hat{\dot{x}}$. The Standard Linear Solid model calculates the contribution $\hat{F}_l$ to force by deflection and velocity using (7.6). The total force estimate $\hat{F}$ is found by adding $\hat{F}_l$, $\hat{F}_T$ and force offset ϕ_o. Finally, the PID controller with anti-windup determines the control signal by using (7.7).

7.2.1. COMBINED ACTUATION AND SENSING

While several ways exist to activate the TCPM, we choose Joule heating by means of a constantan resistance wire. Joule heating has the benefit that it can be used for self-sensing [155]. In this paper, we make use of hardware that realizes this principle [43]. The so-called Muscle Drive (MD) drives the TCPM by applying a Pulse Width Modulated (PWM) signal with a controlled duty cycle D. The electrical response of the TCPM during the off time of a signal period relates to inductance. Based on this response, the MD determines a measure of inductance L^* called decay time [43].

7.2.2. SELF-SENSING MODEL

In our previous work we have introduced a self-sensing model to estimate deflection x, force F and temperature, when measuring both inductance and resistance [155]. In this paper, we first use the electrical power used to heat the muscle P to estimate the contribution of temperature to force F_T. Next, we use L^* to determine x and velocity $\dot{x}$. We calculate their contribution to force F_l via a mechanical model. Addition of F_T, F_l and a force offset ϕ_o gives the total force. Figure 7.2 illustrates this process. Note that the symbol L^* in this paper does not represent physical inductance, but an assumed proportionally related measure thereof.

For the estimation of F_T, we disregard the heating time of the resistance wire and assume it heats the fiber homogeneously. We do not measure temperature independently, and we want to use a minimal set of fitted parameters. Therefore, rather than using temperature, we directly relate input power P to the contribution of temperature to force F_T. A first-order model describes the relation between P, F_T and its derivative with respect to time $\dot{F}_T$ as a function of time t:

$$\dot{F}_T(t) = \kappa_P P(t) - \kappa_c F_T(t), \tag{7.1}$$

where κ_P and κ_c represent the coefficient of conductive heating and convective cooling, respectively. Since F_T represents the contribution of temperature to force, κ_P includes a factor modeling the influence of temperature on force and a factor to correct for power dissipated by the wire directly to the air. We find P by

$$P(t) = D(t)^2 R_\mathrm{m} \left(\frac{U_\mathrm{b}}{R_\mathrm{b}}\right)^2, \tag{7.2}$$

where U_b is the voltage at the connectors of the drive when $D = 1$, R_b the electrical resistance of the circuit as measured at the connectors, and R_m the electrical resistance of the Joule-heating part of the circuit. Note that we neglect the influence of reactive power on heating of the muscle. The muscles used in this paper have an inductance in the order of magnitude of 1 µH. With a signal frequency in the order of magnitude of 100 Hz, the reactive power is around 0.01% of the total power.

The model for computing deflection is taken directly from our previous work [155]. It relates L^* to x and temperature T by

$$L^*(t) = \frac{\lambda_l}{x(t) + \lambda_x} + \lambda_T T(t) + \lambda_\mathrm{o}, \tag{7.3}$$

with λ_l, λ_x, λ_T, λ_o as fitted parameters. In contrast to our previous work [155], we use a constantan resistance wire, which exhibits almost constant resistance regardless of temperature. We can therefore neglect the influence of temperature on the actuation and measurement signal. We furthermore neglect the potential influences of temperature on inductance that do not also influence deflection. Omitting temperature from (7.3) and rewriting the equation to act as a self-sensing model results in

$$x(t) = \frac{\lambda_l - \lambda_x (L^*(t) - \lambda_\mathrm{o})}{L^*(t) - \lambda_\mathrm{o}}. \tag{7.4}$$

As a force model we combine the Standard Linear Solid (SLS) model for the mechanical behavior [120], with a contribution by temperature in parallel, as shown in Figure 7.3. This makes the force model

$$F(t) = F_l(t) + F_T(t) + \phi_\mathrm{o}, \tag{7.5}$$

in which ϕ_o represents a force offset, and for which the contribution by F_l is governed by

$$\dot{F}_l(t) = -\frac{k_2}{c} F_l(t) + \frac{k_1 k_2}{c} x(t) + (k_1 + k_2)\,\dot{x}(t), \tag{7.6}$$

with stiffnesses k_1 and k_2, and damping c. These three parameters, in addition to ϕ_o, are fitted parameters.

7.2.3. ESTIMATOR IMPLEMENTATION

F_T and F_l can be found by transferring their respective models to discrete time. However, filtering is required to process deflection measurements into usable estimates, and we need to estimate $\dot{x}$ as an input for the force model. To that end, we apply a low-pass filter, with a cut-off frequency at 0.111 Hz. Subsequently, we find the velocity by taking the backward difference of the deflection estimate.

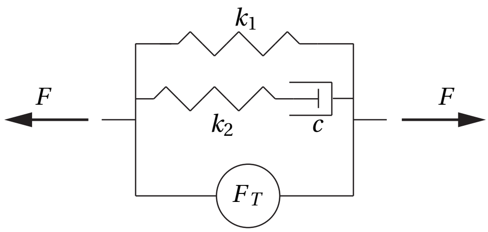

Figure 7.3: Representation of the force model used for the muscles: the Standard Linear Solid model [120], with a contribution by temperature in parallel.

7.2.4. CONTROL DESIGN

To keep control simple, we choose to use PID control with anti-windup via back calculation to deal with the actuation-signal limits [137]. The control law to find the desired actuation signal P_d is given by

$$P_\mathrm{d}(t) = K_\mathrm{p}\left(e(t) + T_\mathrm{d}\dot{e}(t) + \frac{1}{T_\mathrm{i}}\int^t z(\tau)\,\mathrm{d}\tau\right), \tag{7.7}$$

with

$$z(t) = e(t) - \frac{1}{K_\mathrm{p}}\left(P_\mathrm{d}(t) - P(t)\right), \tag{7.8}$$

with the error e and $\dot{e}$ its derivative with respect to time. Control parameters K_p, T_d and T_i respectively represent the proportional gain, and the derivative and integral time constants. We saturate P_d using

$$P(t) = \max\left(P_\mathrm{min}, \min\left(P_\mathrm{max}, P_\mathrm{d}(t)\right)\right) \tag{7.9}$$

with P_max and P_min representing the respective upper and lower bound of the actuation signal. We use this control law for both deflection control and force control. Therefore, the reference r can be either a deflection or a force, and we use the corresponding estimate, $\hat{x}$ or $\hat{F}$, to calculate e and $\dot{e}$. We discretize the integral action by using Euler's method.

7.2.5. STABILITY ANALYSIS

Stability analysis requires knowledge of the full system: the physical actuator, its controller and the load. However, for the method in this paper we do not make assumptions regarding the behavior of the load. In other words, we do not know the behavior of the blocks representing the Universal Testing Machine (UTM) and the physical muscle in Figure 7.2 for arbitrary cases. This means that we cannot analyze stability for the full system. However, we can analyze the stability of the control loop within the gray dotted lines representing the MD, by assuming a constant x, and hence a constant L^*. This case represents force control with a constant deflection.

In this case, closed-loop control reduces to the interaction between the temperature model in (7.1) and the control law in (7.7). A potential source of instability is the saturation in (7.9). Separating the nonlinearity from the dynamics allows for stability analysis via describing functions [13]. To that end, we determine the transfer function from P to P_d, and use a describing function to represent the saturation in the controller. In the Laplace domain, the transfer function that represents the interaction between (7.1) and (7.7) is given by

$$\frac{P_\mathrm{d}}{P} = \frac{-K_\mathrm{p} T_\mathrm{d} \kappa_P s^2 + \left(\frac{1}{T_i} - \kappa_P K_\mathrm{p}\right) s + \left(\frac{\kappa_c}{T_i} - \frac{\kappa_P K_\mathrm{p}}{T_i}\right)}{s^2 + \left(\frac{1}{T_i} + \kappa_c\right) s + \frac{\kappa_c}{T_i}}, \tag{7.10}$$

where s represents the Laplace variable. We can analyze the stability of this system via the describing-function method [13]. Given a properly tuned controller and positive parameters, this system is stable.[1]

7.3. EXPERIMENTAL METHODS

In this section, we first describe the experimental setup, followed by the construction method and limits of the muscle. We then explain the signal construction for identification, training and warming up, followed by the control tasks. Then, we explain the experimental protocol. Lastly we describe how we processed the data.

7.3.1. EXPERIMENTAL SETUP

The MD applies a 20 Hz PWM signal, and measures L^*. To cope with artifacts of the device that result in spikes and predictable variations in the measurements, we apply a 2-sample moving-average filter, and a 15-sample median filter. We use a UTM with a load cell to apply and measure deflection and force. The UTM is a *Mark10 ESM303*, which has a resolution of 0.02 mm. The load cell of the UTM is a *Mark10 M5-05* Force Gauge, which has a resolution of 0.5 mN. We control both the UTM and the MD with custom Python code, running on a laptop. The perspex duct surrounding the TCPM, and a *GELID silent 12* 120 mm fan directed at the TCPM, with 10 V applied, ensures the controlled flow of air at room temperature for convective cooling. Figure 7.4 illustrates this setup.

7.3.2. MUSCLE CONSTRUCTION AND LIMITS

For construction of the TCPM we use the method described in our previous work [155]: we align the precursor fiber and resistance wire, with a load suspended at one end, blocking rotation, and a rotary motor at the other. We twist the line until it just starts to coil upon itself. Complete coiling can be achieved either by letting the whole fiber coil upon itself, or by wrapping it around a mandrel. We choose the latter, for it increases the sensitivity of inductance to muscle deflection. Annealing finishes the muscle. The endings of the resistance wire connected to the electrical leads are shaped such that when the TCPM is under tension, their influence on the force measurement is minimal. The relevant specifications for construction are shown in Table 7.1.

[1]The negative reciprocal of the describing function for the saturation nonlinearity is part of the negative real axis in the Nyquist plot. In such a case, a limit cycle can exist if the relative degree of the loop transfer function is greater than two, and the gain of the saturation is sufficiently high. This is not the case for transfer function in (7.10), and the applied saturation. The closed loop is therefore stable.

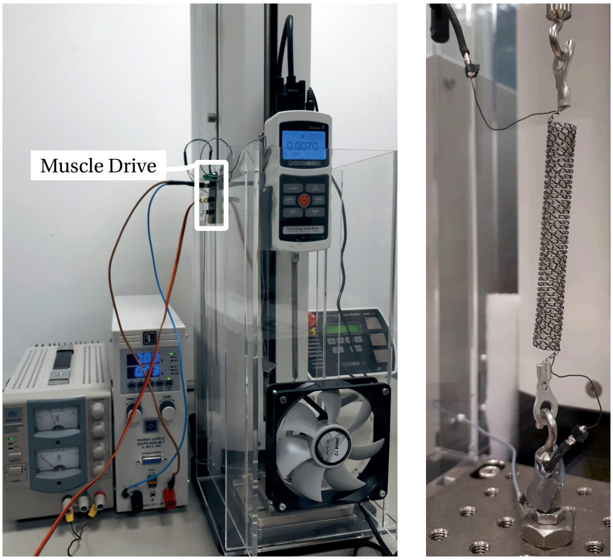

(a) (b)

Figure 7.4: Overall setup, with the Universal Testing Machine and the Muscle Drive in (a) and the Twisted and Coiled Polymer Muscle in (b).

To obtain repeatable actuation behavior we had to train the muscle [155]. In addition, in pilot experiments we found that trained muscles that had been inactive for a day needed a *warming up* to regain that same behavior. Therefore, we included a warming-up phase each time we started an experiment and when we continued an experiment after a pause in the protocol. In this paper, we implemented a warm up as approximately 10 minutes of excitation similar to the experiment.

We determined the following limits of deflection and power through pilot experiments. To be sure to have overcome the preload knee and avoid nonlinear behavior due to touching coils [26, 175], we choose $x_{\mathrm{min}} = 10\,\mathrm{mm}$ as the minimum deflection for the experiments. To prevent overstretching, we choose $x_{\mathrm{max}} = 30\,\mathrm{mm}$ as the maximum deflection. With a voltage of $U_{\mathrm{b}} = 7\,\mathrm{V}$ applied on the electrical leads, and a resistance at the connectors of $R_{\mathrm{b}} = 10.75\,\Omega$, of which the resistance at the muscle is $R_{\mathrm{m}} = 10.18\,\Omega$, the maximum power input would be 4.31 W. However, to prevent overheating, we choose a 85% duty cycle as the maximum, obtaining $P_{\mathrm{max}} = 3.12\,\mathrm{W}$. In addition, the MD requires a minimum duty cycle of 15% to provide accurate measurements. This is a practical limitation of the MD, when combined with constantan wire for Joule heating. This sets the lower limit at $P_{\mathrm{min}} = 0.10\,\mathrm{W}$. Therefore, the boundaries within which we performed the experiments are $[10, 30]\,\mathrm{mm}$ for deflection and $[0.10, 3.12]\,\mathrm{W}$ for power.

7.3.3. SIGNAL CONSTRUCTION

In training, warming up, identification and validation we simultaneously excited the muscle with signals on P and x, respectively applied by the MD and the UTM. We used two signal types: a multi-sine signal m, and random-step signal g.

We constructed the multi-sine signal with N components as

$$m(t) = a_0 + \sum_{i=1}^{N} a_i \sin\left(2\pi f_i t + \phi_i\right), \tag{7.11}$$

with a_0 the signal offset, a_i the amplitude of the ith component, f_i its frequency and ϕ_i its phase. We determine the phases of the signal with

$$\phi_i = \phi_0 - \frac{\pi i^2}{N}, \tag{7.12}$$

where ϕ_0 is a pseudo-randomly chosen phase offset. This construction method avoids high peaks [125]. We took equal amplitudes, with the signal scaled such that it fit the deflection and power limits, respectively. The frequency interval from which we took the N equally spaced frequencies was $[10^{-2.4}, 10^{-1.1}]$ Hz. To avoid producing the same signal for deflection and power, we took two different prime numbers for N and produced two different values for ϕ_0. For the deflection excitation we chose $N = 11$, and for the power excitation we took $N = 7$.

We constructed the random-step signal with H steps as

$$g(t) = b_0 + \sum_{i=1}^{H} b_i h(t - \tau_i) \tag{7.13}$$

with h representing the Heaviside step function, b_0 the signal offset, b_i the amplitude for each step and τ_i the step times. We determined the step times with a random generator, following the construction of step times for generalized binary noise [152]. Given a certain process time constant τ_p and sampling frequency f_s, for each sample time, the probability p the signal switches is

$$p = 1 - \frac{1}{0.5\tau_p f_s}, \tag{7.14}$$

Table 7.1: Muscle Construction Specifications

Property	Value
precursor fiber diameter	0.8 mm
precursor fiber material	nylon
resistance wire diameter	0.3 mm
resistance wire material	constantan
load at twisting	≈ 6.50 N
mandrel diameter	5 mm
mandrel length	50 mm
annealing temperature	165 °C
annealing time	1 hour
nr. of windings	46
Joule-heating resistance	10.18 Ω
Joule-heating inductance	≈1.30 µH

such that the average time between switching was half the process time constant. Via pilot experiments we determined the approximate time constants for deflection and power to be respectively $\tau_p \approx 2\,\mathrm{s}$ and $\tau_p \approx 35\,\mathrm{s}$. However, to not let the influence of deflection dominate in the identification data set, we chose the time constants for deflection and power to be respectively $\tau_p = 12.5\,\mathrm{s}$ and $\tau_p = 20\,\mathrm{s}$. For the size and direction of the step, we used two pseudo-random processes. First, we sampled the step size from a uniform distribution $\left[0, 0.25\left(g_{\mathrm{max}} - g_{\mathrm{min}}\right)\right]$, with g_{max} and g_{min} representing the upper and lower limit of deflection and power, respectively. Next, a virtual coin toss determined the direction of the step. However, if a step in either direction would take the signal out of bounds, the opposite direction was chosen. Finally, we scaled the signal to include the upper and lower limits of deflection and power.

7.3.4. CONTROL TASKS

We performed several control tasks to quantify the self-sensing performance and the closed-loop control performance of the muscle. We had the muscle perform both force and deflection control. Both consisted of step responses to determine control behavior, and tracking sinusoid references to find the bandwidth of the actuator. The step references contained 7 steps, spread over the respective ranges of $[0.375, 0.525]\,\mathrm{N}$ and $[10, 30]\,\mathrm{mm}$. Each step was held for 20 s. The sinusoid reference swept over 15 subsequently applied frequencies. For force control the sinusoid had a 0.05 N amplitude and a 0.40 N offset. For deflection control the sinusoid had a 5 mm amplitude, and a 20 mm offset. The frequencies were logarithmically spaced within the same frequency interval used for the multi-sine identification signal. The application of each frequency lasted for three periods. In pilot experiments we tuned the gains of both controllers, via the Ziegler-Nichols method [186]. For deflection control we used PID control, with $K_{\mathrm{p}} = -1.08\,\mathrm{W/mm}$, $T_{\mathrm{d}} = 0.625\,\mathrm{s}$ and $T_{\mathrm{i}} = 2.5\,\mathrm{s}$. For force control we chose to use PI control, with $K_{\mathrm{p}} = 540\,\mathrm{W/N}$ and $T_{\mathrm{i}} = 1\,\mathrm{s}$. During the control tasks the UTM respectively imposed deflection and force. For deflection control, we had the UTM maintain a constant force of 0.40 N. For force control, we had the UTM maintain a 20 mm deflection.

As part of the control tasks, we implemented a calibration sequence for deflection measurements and force estimates. The calibration provided two offsets, compensating for unmodeled effects, and disturbances happening in between identification and control. For calibration of the deflection measurements the UTM held a deflection of 20 mm. The difference between the deflection estimate and the actual deflection, averaged over 10 s, gave the calibration offset for the deflection measurements. For calibration of the force estimates the UTM held a force of 0.40 N, while the MD controlled the deflection. The difference between the force estimate and the actual force, averaged over 30 s, gave the calibration offset for the force estimates.

7.3.5. EXPERIMENTAL PROTOCOL

For training we first suspended the untrained TCPM and set the load cell to zero. We then attached the bottom of the TCPM to the UTM, and set the position of the UTM, such that the TCPM just started to be under tension. At this point, we set the deflection of the UTM to zero. Then, we turned on the fan and the MD, and started the training. We excited deflection and power for 600 s, using a multi-sine signal for both.

The identification was initiated in the same way as training. Prior to gathering identification data, we gave the TCPM a warming up by means of a 250 s multi-sine on deflection and power. For identification we subsequently applied a 200 s multi-sine, and a 200 s random-step signal on both deflection and power. For validation of the identification, we applied a 100 s multi-sine, followed by a 120 s random-step signal on both deflection and power. Directly after gathering identification data and preceding the control tasks, we identified the model parameters as described in the following paragraph. During this time the TCPM was still suspended in the UTM.

The control tasks were preceded with warming up the TCPM by means of a 380 s multi-sine, and a 200 s random-step signal on both deflection and power. After the warm up, we calibrated the deflection measurements and force estimates. Next, we started the force-control tasks. After completion, we recalibrated the deflection measurements and force estimates, to correct for numeric drifting or low-frequency effects that were not included in the models. We then continued the experiment with the position control tasks.

7.3.6. DATA PROCESSING

The data acquired by the UTM and the MD had their own respective time stamps. Using those, we aligned and re-sampled both UTM and MD data to 16 Hz.

To identify the 6 parameters for (7.1), (7.5) and (7.6), we minimized the squared error between the measured and estimated force response. We obtained the estimated force response by running a simulation of the dynamical system, with the re-sampled power and deflection as input. With MATLAB's genetic-algorithm optimization we came close to the absolute minimum. Subsequently, with MATLAB's nonlinear least-squares optimization, via the Levenberg-Marquardt algorithm, we found the absolute minimum. We found the 3 parameters for (7.4) in a similar fashion, minimizing the squared error between estimated and applied deflection.

For analysis of the models, we first calculated the Root Mean Square Error (RMSE) to quantify the estimation error of deflection and force. Second, we assessed the quality of the fit via the R^2 value, given by

$$R^2 = 1 - \frac{\sum_{i=1}^{n}(y_i - f_i)^2}{\sum_{i=1}^{n}(y_i - \bar{y})^2}, \tag{7.15}$$

where y_i are the n data points with $\bar{y}$ as their mean, and f_i the estimates. We calculated the R^2 and RMSE values for the offline estimates belonging to the identification and validation part, and online estimates of the control tasks. In addition, we calculated the 95% confidence interval for online estimation of both deflection and force. We used the data gathered during deflection control to assess deflection estimates, and data gathered during force control to assess force estimates.

To take a closer look at the performance and limitations of control, we calculated the rise times of the step responses. In addition, to determine the bandwidth of the actuator, we fit the amplitude, phase and offset of a sinusoid with a given frequency to the respective responses to the last two periods of the sinusoid reference. We approximated the bandwidth by determining the -3 dB point via linear interpolation of the resulting magnitudes.

7.4. RESULTS

Figure 7.5 shows the time series of the identification and validation experiment. Table 7.2 gives the fitted parameters for (7.1), (7.4), (7.5) and (7.6). Table 7.3 shows the quality of the fit and the estimation error resulting from these parameters.

Figure 7.6 highlights the online estimation of deflection and force, by directly comparing the estimates to the true values. We achieved 95% confidence intervals of respec-

Table 7.2: Fitted parameters for measuring deflection and estimating force. The unit at * proportionally relates to μHmm. The unit at ** proportionally relates to μH.

	x			F		
λ_l	2.81 *	κ_P	7.2 10^{-3} N/J	k_1	10.8 10^{-3} N/mm
λ_x	28.8 mm	κ_c	131.6 10^{-3} 1/s	k_2	2.7 10^{-3} N/mm
λ_0	0.433 **	ϕ_0	106.9 10^{-3} N	c	4.3 10^{-3} N.s/mm

Table 7.3: Fit quality measures for deflection and force, for data regarding fitting, validation and control.

	Fit		Validation		Control	
	R^2	RMSE	R^2	RMSE	R^2	RMSE
x	0.96	0.97 mm	1.00	0.39 mm	0.93	1.10 mm
F	0.97	12.8 mN	0.98	12.7 mN	0.86	16.3 mN

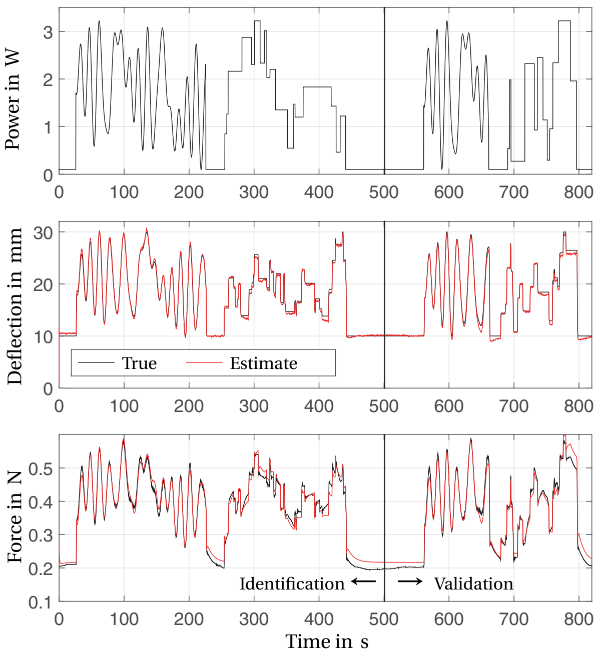

Figure 7.5: Time series of the identification and validation. The top figure shows the applied power. The middle figure shows the applied deflection in black, and the fit deflection estimate in red. The bottom figure shows the measured force in black and the fit force in red. In all figures, the black vertical line shows the separation of identification and validation data.

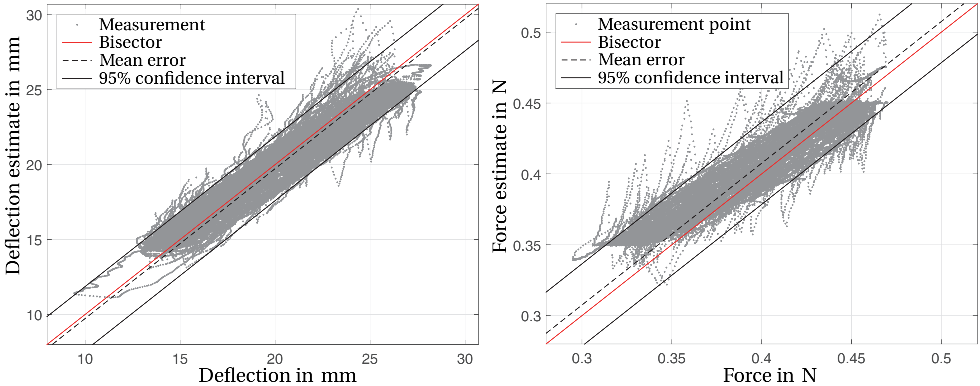

(a) Deflection estimation during deflection control. (b) Force estimation during force control.

Figure 7.6: Estimation data during respectively deflection control (a) and force control (b). The gray dots and effectively gray areas represent the estimates given at the true value. The red line represents bisector of the graph, indicating what the correct values would be. The area between the black lines indicates the 95% confidence interval, which is ±2.14 mm around a mean error of -0.27 mm for deflection, and ±29.0 mN around a mean error of 7.5 mN for force.

tively 2.14 mm around a mean error of -0.27 mm for deflection estimation, and 29.0 mN around a mean error of 7.5 mN for force estimation.

Figure 7.7 shows the resulting time series of the control experiment. Figure 7.7a and Figure 7.7b show the step responses during deflection and force control, respectively. Figure 7.7c and Figure 7.7d show four representative periods of the sine sweeps, respectively. In Figure 7.8 we show the frequency responses of the sine sweeps during deflection control, and during force control. The step responses during deflection control had rise times between 4.2 s and 14.1 s, and during force control they had rise times between 2.1 s and 5.1 s. Both ranges had outliers at 20 s, indicating that the response did not reach the reference value. We found the bandwidth for deflection control to be approximately 0.039 Hz, and for force control approximately 0.056 Hz.

7.5. DISCUSSION

Our method and implementation of self-sensing resulted in a 95% confidence interval of 2.14 mm around a mean error of -0.27 mm for estimation of deflection, and 29.0 mN around a mean error of 7.5 mN for estimation of force. Combined with our control implementation we achieved a 0.039 Hz for deflection control, and 0.056 Hz for force control.

The RMSE and 95% confidence interval we achieved for estimation of deflection were sufficient for feedback control. From these results, we conclude that our measurement model in (7.4) includes the most important effects. Still, tailoring the hardware to the range of inductance of this specific muscle would likely improve the measurements. Furthermore, we needed an averaging filter and a rather strong median filter to avoid spikes in the data. These artifacts should be taken care of in a new version of the hardware. Additionally, the low control bandwidth allows for low-pass filters to smoothen the signals,

7

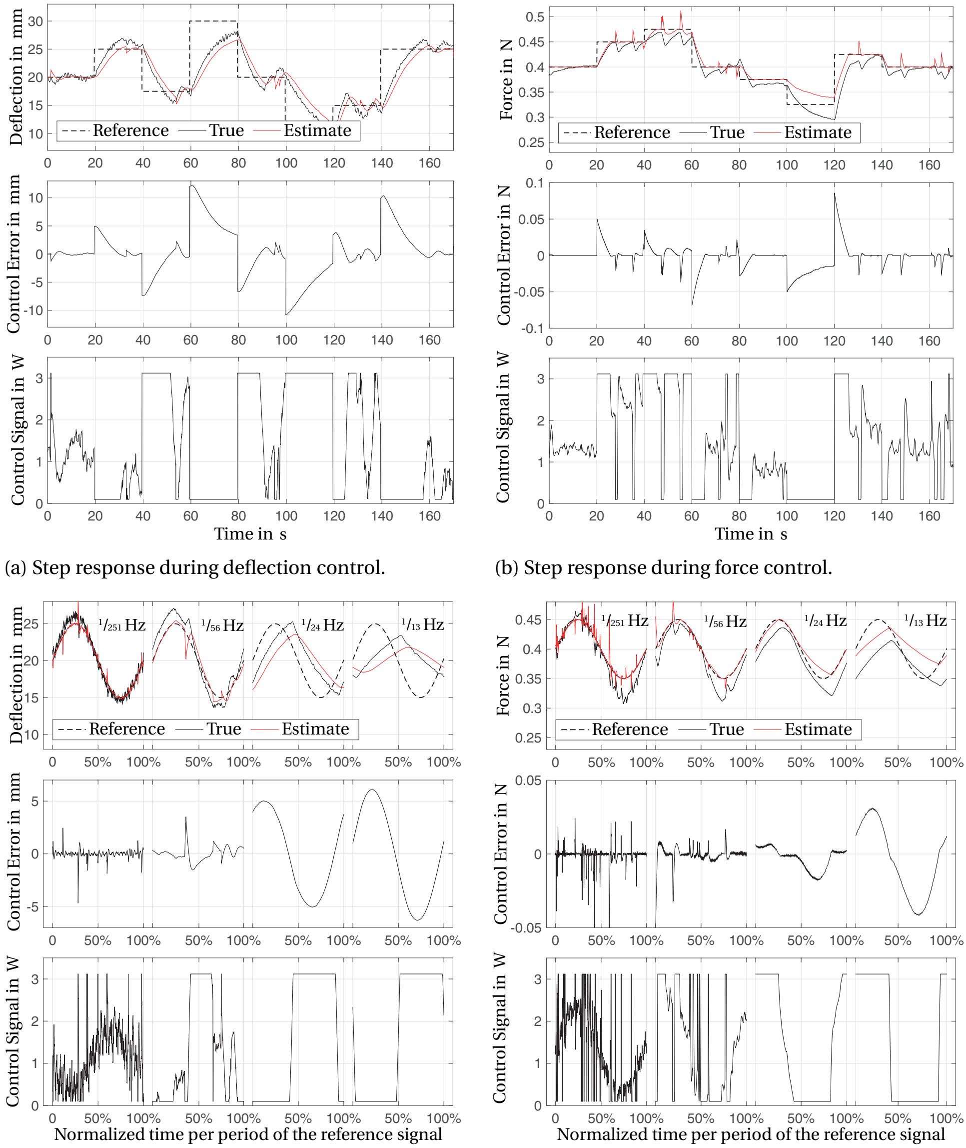

(a) Step response during deflection control.

(b) Step response during force control.

(c) Sine sweep during deflection control.

(d) Sine sweep during force control.

Figure 7.7: Time series data regarding the control experiment. The top figures show the step responses with respectively deflection control (a) and force control (b) over time. The bottom figures show four sample periods during the sine sweep with respectively deflection control (c) and force control (d). In all four figures, the black solid line indicates the true value, the red line indicates the estimate, and the dashed black line indicates the reference.

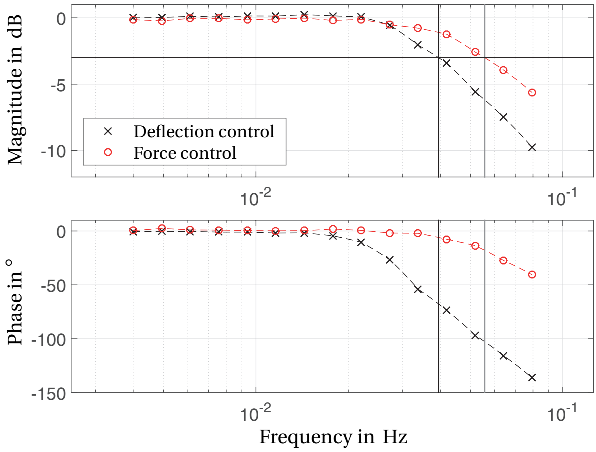

Figure 7.8: Frequency response data of the sine sweeps, with deflection control in black, and force control in red. The cross markers indicate the measured response. The dashed lines indicate the linear interpolation between these points. This shows that the -3 dB point for deflection control lies at approximately 0.039 Hz, and for force control approximately at 0.056 Hz.

without compromising the bandwidth.

Furthermore, in the measurement model we neglected the potential influence of the applied control signal and the influence of temperature. The former requires additional research, in combination with developments in hardware. The latter requires a measurement of temperature, for example via resistance, as in our previous work [155].

The presented implementation for force estimation also captures the most important effects, and allows for feedback control. However, it does need improvement of both precision and accuracy. The force estimates in Figure 7.7b and Figure 7.7d show underestimation at the bottom edge of the achievable force interval, when the control signal is at the lower saturation limit. This indicates that the experimental procedure to find the Joule-heating parameters might underestimate the contribution by convective cooling. Moreover, the peaks in deflection measurements propagate in the force estimate. This explains the peaks in Figure 7.7b. In additional future work, we aim to quantify the repeatability of the behavior of the muscles, both within and between muscles.

We included a warming-up phase in the experimental protocol, to ensure repeatable behavior. This limits the use for practical applications. Effectively, the training is a coping mechanism for a relaxation effect with a low time constant. Endurance tests will reveal this time constant. Subsequent modeling thereof allows for omission of the warming up.

Figure 7.7a and Figure 7.7b illustrate the response of the muscle to step inputs on the reference during respectively deflection and force control. Firstly, the rise times vary from 2.1 s to 14.1 s, excluding outliers at 20 s. Herein, the large variation in settling times can be explained by the variation in step sizes, combined with the saturation on the control action. Secondly, the time constants for heating and cooling seem similar, whilst convective cooling is hard to control. The experimental setup in this paper aims to keep the environment constant, to minimize variation in cooling rates. Furthermore, the procedure has been tuned in pilot experiments to balance the time constants. This shows the challenge of using a TCPM with Joule heating and convective cooling in a practical application.

Figure 7.8 shows a limited bandwidth, while a high bandwidth is beneficial for robotic applications. TCPMs inherently suffer from this issue, because in practice heating and cooling are slow processes. However, these actuators are suitable for tasks that do not require a high bandwidth. For example, in compliant structures like tensegrities they can slowly change the configuration or stiffness, or apply pre-tension.

Furthermore, there are possibilities to increase the bandwidth reported in this study by optimizing material properties, the activation principle, muscle configurations and control methods. For example, we recommend to use smaller diameter fibers or a suitable configuration of several muscles, like an antagonistic setup [134, 138]. In addition, we see opportunities for improving the implementation of the activation principle by expanding the control action space. For example, active cooling with a controlled fan stimulates muscle expansion [140]. Changing the cooling medium from air to liquid improves the performance as well [92, 134, 174], but adds weight and complexity. Moreover, when the application of the actuator is known, a feedforward signal could improve the control performance.

A drawback of the TCPM is the poor scalability when considering a single muscle. Using a structure of TCPMs to perform as one actuator increases the scalability and versatility [49, 66]. However, closely packing the muscle might lead to interaction of actuation and sensing, and complicates cooling. In future work, we will investigate these potential disturbances for self-sensing and actuation in muscle structures, and methods to cope with those disturbances.

7.6. CONCLUSION

In this study, we aimed at strengthening the position of TCPMs as a feasible actuator in inexpensive and lightweight control systems. To that end, we closed the feedback loop of a controlled TCPM via self-sensing. We estimated both the deflection and force, using the applied power and self-sensing measurements of deflection as input. Subsequently, this allowed us to control either deflection or force. We achieved a 95% confidence interval of 2.14 mm around a mean estimation error of -0.27 mm and 29.0 mN around a mean estimation error of 7.5 mN, for respectively deflection and force. This work validated the used sensing model, and laid the foundation for further developments of research and hardware. It demonstrated the increase in potential of TCPMs to be the actuators in inexpensive and lightweight control systems.

8

Discussion and Conclusions

Chapter 1 outlines this thesis based on nine questions. The first section of this chapter starts with a summary of and reflection on the answers to those questions based on the individual chapters, and finishes with a general discussion of this thesis. The second section provides the main conclusions of this thesis. Finally, the last section gives recommendations on how to proceed.

8.1. DISCUSSION

8.1.1. INDUCTANCE-DEFLECTION RELATION IN COIL SPRINGS

OVERVIEW

The first two questions of this thesis are based on two notions. Firstly, helical springs resemble solenoid coils. Secondly, the inductance of solenoid coils strongly varies with their geometric properties, which includes deflection. With an aim to exploit this for sensing purposes, Chapter 2 starts exploring the potential by asking:

1. What is the theoretical relation between inductance and deflection of a coil spring?

The theoretical investigation in Chapter 2 discusses a number of ways to approximate the inductance of solenoid coils with a known geometry. The experiments in this chapter partly aim at determining the usability of these theoretical relations as a sensing model for coil springs. In other words, how accurate do theoretical models predict the length of a coil, when measuring its inductance. The results show that none of the theoretical approximations accurately predict deflection of coil springs. In fact, the average prediction error was larger than 20%, with peaks above 50%. Therefore, theoretical relations cannot be used directly to estimate deflection. This leads to the follow-up question:

2. How can we practically use the inductance-deflection relation to measure deflection?

All theoretical models have one thing in common. They describe a relationship between inductance and length dominated by inverse proportional behavior with an offset. Fitting the two parameters of this relation on a calibration data set delivers a simplified model for individual springs. Calibration compensates for manufacturing uncertainties and other discrepancies.

The experiments validate this method. They result in an averaged estimation error of 1.1%, with peaks at 1.9%. These first results show the potential of this method to compete with traditional sensing methods.

REFLECTION

The theoretical investigation towards inductance calculation provides valuable insights into the modeling of coil spring inductance. It leads to a two-parameter fitted model, which is very well suited for sensing purposes. This model is computationally inexpensive, and the achieved accuracy is competing with existing sensor solutions.

The work in Chapter 2 experimentally validates its premise in a lab environment. Hence, the first question that arises from this promising innovation regards the applicability in a real-world environment. Various factors in coil spring applications can influence the measurements of inductance. For example, electromotors produce rapidly fluctuating electromagnetic fields, and neighboring components made of ferromagnetic material influence the magnetic permeability. Calibration could account for these influences, if they are static. However, dynamic disturbances are more difficult to mitigate. This requires further research on the sensitivity of inductance measurements to various disturbances. Alternatively, an engineering approach could attenuate the potential influences, for example by shielding.

The results indicate where the presented method can be improved. They show an overestimation of deflection in the middle of the investigated range. The accuracy of the method can be improved in two ways. Firstly, fitting the relation on data points closer to the middle of the range, rather than the extremes, might average the error. In general, adding data points will average the error. Secondly, this overestimation indicates that the inverse proportional relation does not fully capture all behavior. Augmenting the relation with a term to account for non-modeled effects might already improve the accuracy.

8.1.2. COMPARING INDUCTANCE- WITH RESISTANCE-BASED SENSING IN COIL SPRINGS

OVERVIEW

The most common electrical property used for sensing is resistance. However, Chapter 2 focuses solely on sensing via inductance. To validate the use of inductance compared to resistance, Chapter 3 answers the question:

3. How does sensing deflection of coil springs via inductance compare to via resistance?

The short study in Chapter 3 first investigates what deformations in deflected coil springs affect the resistance. Next, the change in resistance when deflecting a coil spring is compared to change in inductance, based on the data gathered in Chapter 2. These experiments show an ambiguous relation between resistance and deflection of coil springs, while for inductance and deflection the relation is unambiguous.

REFLECTION

This study indicates that inductance trumps resistance, when it comes to suitability for sensing in coil springs. However, it uses data from experiments optimized for measuring inductance. A method dedicated to obtaining optimal data for resistance might provide quantitatively different results.

In general, resistance measurements have several benefits over inductance measurements. Opposite to inductance measurements, resistance measurements are not known to experience disturbances from their surroundings. Furthermore, resistance measurements are usually not time dependent, while inductance measurements usually are. Moreover, it is a very well developed field of sensing technology. This warrants the study of methods using resistance measurements in coil springs.

8.1.3. MEASURING FORCE IN OSCILLATING COIL SPRINGS

OVERVIEW

Based on the findings of Chapter 2, Chapter 4 applies the new method for sensing deflection in a dynamic setting. While triggered by curiosity towards the dynamic effects on inductance, the leading question of this chapter takes a broader perspective:

4. How do dynamic excitations on coil springs affect measurements of different sensor types?

Chapter 4 first models the dynamics of a coil spring as a lumped-mass model representing the axial motion of individual windings. Next, it couples the mechanical model to an inductance model investigated in Chapter 2. These two models suffice to simulate the output of a force sensor, a deflection sensor and an inductance-based deflection sensor applied on a coil spring.

The simulation includes three impact conditions found in the Series Elastic Actuator (SEA) used in a walking robot and in the Parallel Elastic Actuator used in a lower-leg prosthesis. These impact conditions could result in internal oscillations. In addition, the simulation includes harmonic excitations at half of, and exactly on the Eigenfrequency. The work also includes an experiment. It consists of a coil spring undergoing harmonic excitation at a number of frequencies, while all sensors simultaneously measure deflection of or force on a coil spring.

The simulation and experiment show that internal oscillations due to a number of sources result in different sensor readings depending on the sensor. In simulation, heel strikes, collisions with end-stops and harmonic excitations not near the Eigenfrequency of the coil spring result in force differences below 4%. Simulation of excitation at the Eigenfrequency result in a maximum force difference of 97% between a force sensor at an end point, and using the deflection and stiffness to calculate the force. In experiments, harmonic excitations that avoid excitation of the Eigenfrequency result in differences below 1%, and excitation at half the Eigenfrequency results in a difference over 4%.

Both simulation and experiment show differences between sensor types when internal oscillations occur. In the context of this thesis, this leads to the question:

5. Is the influence of internal oscillations on inductance a practically relevant effect?

The results show the presence of the effect and compare it to the effects noticed in the other sensors. First, they compare deflection-based force measurements with a Laser Distance Meter (LDM) and direct force measurements with a Load Cell (LC). Second, the results compare deflection-based force measurements with a LDM, with inductance-based force measurements. Note that inductance-based force sensing takes a step via deflection, so it essentially is a deflection-based method as well. The differences between direct force measurements and deflection-based force measurements are bigger than the differences within the two deflection-based force measurements. In addition, the differences within the deflection-based methods are small compared to the estimation error achieved in Chapter 2. Based on these findings, the influence of internal oscillations on inductance-based force measurements seems practically irrelevant, especially compared to effects noticed in other sensors.

REFLECTION

The work in Chapter 4 demonstrates the influence of internal oscillations on coil springs. The forces measured at the end points differ from each other and from measurements determined via deflection. However, severe deviations only occur when an Eigenfrequency of the coil spring is harmonically excited. In general, system designers should take into account that coil springs have their own internal Eigenfrequencies, which differ from the system's Eigenfrequencies. When internal oscillations impede normal operation, designers should avoid exciting them, or include physical damping in the system.

This work validates the use of inductance-based sensing in a dynamic application. Internal oscillations do affect deflection and force measurements, especially when exciting an Eigenfrequency of the coil spring. However, the effect is negligible compared to the estimation error found in Chapter 2.

This work also demonstrates that inductance-based sensing underestimates deflection and force when internal oscillations occur. The nonuniform winding distribution resulting from the oscillations influence the inductance. Parts of the coil spring have a higher winding density, and parts have lower winding density. While this variation respectively increases and decreases the local inductance, the inverse proportional relation shows that the increased density has a stronger effect than the decreased density. Hence, the inductance will be larger than with a uniform winding distribution. This in turn results in the underestimation of deflection and force. However, the results show that the averaged estimation error resulting from this effect is negligible compared to the force difference as measured at the end points of the coil spring.

This study only focuses on axial excitations, whilst lateral excitations are also likely to occur. Future research should find how lateral excitations influences sensing on coil springs, and how it compares to the influences of axial excitations.

8.1.4. SELF-SENSING MODELS FOR JOULE-HEATED TCPMS

OVERVIEW

In Chapter 6, the focus of the thesis shifts from coil springs to Twisted and Coiled Polymer Muscle (TCPM)s. The force applied by a TCPM not only varies with deflection, but also with temperature. With the previous chapters as background and considering that temperature typically influences resistance, this chapter aims to find self-sensing models for the full state of a TCPM via the electrical impedance of its Joule-heating element. Hence, the leading question of this chapter is:

6. How does the inductance and resistance of a TCPM relate to its deflection and temperature, and subsequently force?

The study first investigates how inductance and resistance vary with deflection and temperature. Subsequently, it models the relation between deflection, temperature and force. Rewriting the relations results in three equations with in total nine fitted parameters to relate the electrical impedance of the muscle to its (thermo-) mechanical state.

Experiments on a TCPM with an iron resistance wire provide data to fit the parameters. The results indicate that, for this TCPM, deflection influences both inductance and resistance. This holds for temperature as well. However, deflection mainly relates to inductance, and temperature mainly relates to resistance.

The found relations allow for estimation of the full state of the muscle, via electrical impedance. This leads to the following question:

7. What is the estimation quality when using these relations for sensing?

The same experiments provide data to validate the relations as sensing models. Results show the quality of these relations as sensing models. Deflection, temperature and force estimation contain an error of respectively 0.8%, 0.5% and 7.6%. These results validate the use of the former two models as self-sensing models, and shows that the force model does not suffice.

REFLECTION

The work in Chapter 6 derives and quantifies the quality of static self-sensing models of a TCPM with iron-wire as Joule-heating implementation. Based on measurements of inductance and resistance, the models allow estimation of deflection and temperature of the muscle with an accuracy comparable to more mature sensing solutions. However, the model used to estimate force requires improvement.

The models do not include time-dependent behavior. However, steps shown in the time-series data on force show regular and inverse relaxation behavior. This behavior seems to qualitatively correspond to the Standard Linear Solid (SLS) model [120]. This explains the hysteretic behavior found over the full time-series. The experimental setup in this chapter does not allow for time-dependent measurements of electrical impedance. This means that potential hysteretic behavior influencing the electrical impedance could not be observed directly. However, the quality of estimating deflection and temperature implies that the hysteretic behavior does not influence the electrical impedance. Hence, deriving a force model with deflection, temperature and time as input could suffice to improve the estimation of force.

8.1.5. CLOSED-LOOP CONTROL OF TCPMS THROUGH SELF-SENSING

OVERVIEW

A patented invention that can simultaneously apply power and determine a measure of inductance enables the realization of actual self-sensing [43]. While Chapter 6 includes measurements of both inductance and resistance, Chapter 7 only has the applied power and a measure of inductance as available information. However, that should suffice for self-sensing of deflection and force. Hence, the question that follows is:

8. What is the performance of self-sensing of force and position of a TCPM, based on input power and measurements of inductance?

The study starts by deriving self-sensing models that have power and inductance as input, and deflection and force as output. By using constantan as Joule-heating wire, as opposed to iron in Chapter 6, it is safe to assume that the impedance does not change with temperature. This decouples the equations. In addition, a pilot experiment shows an unvarying resistance with varying deflection for the used TCPM. This leads to a self-sensing model for deflection similar to Chapters 2 and 4. Moreover, it relates deflection and power to force using a dynamic model, which partially consists of the SLS model.

Experiments validate the models. The self-sensing method results in an average estimation error for deflection and force of respectively 2% and 3.6% for the validation, and respectively 5.5% and 4.7% during control. The 95% confidence intervals were -0.27 ± 2.14 mm and 7.5 ± 29 mN for respectively deflection and force.

The presented self-sensing implementation enables closed-loop control. However, there might be undesired effects that limit control performance. This begs the question:

9. What is the control performance when using this self-sensing implementation?

The step responses and the sine sweep performed in the control experiment show the control performance. The presented implementation results in step responses with rise times between 2 and 14 seconds, and it reaches a bandwidth of 0.039 Hz and 0.056 Hz when respectively controlling deflection and force.

REFLECTION

The achieved self-sensing performance shows that the models include the dominant effects. It suffices for closed-loop control, and demonstrates the potential. However, there is still room for improvement. For example, expansion of the force model would allow inclusion of observed long-term relaxation behavior. Moreover, improving the hardware, and tailoring it to a specific measurement range will likely improve estimation accuracy. In addition, including a resistance measurement and incorporating it in the models allows more accurate estimates.

The sensitivity of the sensing method presents itself in the propagation of sensor artifacts, i.e. large spikes in the values, from deflection estimates to force estimates. While in deflection estimates it is just a spike, in force estimates it propagates as a contribution of velocity and integration of the spike. To avoid heavy filtering, the hardware should provide a smooth signal.

The experiment illustrates limitations of both the TCPM and control. The limited rise times and bandwidth result from a limited control-action space. During both heating and cooling the set saturation values frequently limit the control action. This issue is inherent to using TCPMs. The maximum temperature to drive the muscle should not exceed the maximum temperature the muscle or its material can handle, hence limiting the heating rate. The cooling rate involves a trade off, which includes the practicality of the cooling medium, its temperature and the minimum temperature the TCPM can handle. Others have presented practical ways to deal with these limits. For example, introducing actively controlled cooling [140] or using smaller diameter fibers would likely improve the muscle's bandwidth. In addition, using a smart configuration of several muscles, like an antagonistic setup [134, 138], could also improve the control performance.

8.1.6. GENERAL DISCUSSION

Self-sensing provides a number of advantages, like cost and weight reduction, collocated sensing, and simpler mechanical designs. However, it also brings its own challenges. First, self-sensing typically requires in-depth knowledge or analysis of the specific component or system and its environment to obtain useful measurements [60, 86]. This makes the systems less apprehensible. Second, combining an actuation and a sensing signal frequently involves complex electronics [43, 50, 60]. In other words, self-sensing partially transfers design complexity from the mechanical domain to the electrical domain. Third, separation of concerns is a paradigm well known in software and systems engineering [6, 158]. By separating system requirements and their solutions, complex systems become apprehensible and the solutions generalizable. Self-sensing opposes this principle by integrating separate tasks in one system. However, confining self-sensing to small systems, like off-the-shelf actuators, limits the complexity of the design and implementation. In turn, this mitigates the presented challenges. Especially in systems where physical space limits the design options, self-sensing potentially warrants the effort.

For TCPMs both resistance and inductance can relate to deflection and force. Additionally, only measuring a single variable does not generally suffice to determine the full state of an actuator. However, in specific cases measuring a single variable should suffice. For example, applications potentially provide information about the load on the actuator via additional sensors or via knowledge on the nature of the load. The studies in [50, 139, 142, 175] make use of this. They measure resistance to estimate and control deflection or temperature. In contrast to these studies, this thesis aims to estimate the full state of the TCPM via self-sensing. To that end, it combines measurements of inductance with resistance, and does not rely on additional sensors or prior knowledge of the application.

While cost and weight are two major benefits, the inherently low bandwidth of the general TCPM is a major drawback. Herein, its performance compares to Shape Memory Alloy (SMA), and is underwhelming compared to other artificial muscles. Next to the applications of TCPMs mentioned in Chapter 5, it could have applications similar to SMA, like cars, planes and biomedical devices [38, 72, 93].

8.2. CONCLUSION

This thesis aims to improve coil springs and TCPMs by integrating sensing. To that end, it investigates and models behavior in multiple physical domains, and connects them such that they function as self-sensing models. The studies presented in this thesis lead to two conclusions.

Firstly, the relation between deflection and inductance of coil springs is very well suited for self-sensing. The inverse-proportional relation can easily be found using a two-point calibration. Internal oscillations or other dynamic effects in coil springs could result in underestimation of deflection and force. However, the magnitude of this effect is of no practical relevance compared to effects noticed by other sensors. Therefore, a static relation suffices. For self-sensing in coil springs, the challenge lies in designing inexpensive and reliable hardware that provides fast measurements, while mitigating environmental influences. The results of this thesis provide leads to simplified mechanical designs of SEA through self-sensing.

Secondly, self-sensing of Joule-heated TCPMs can be achieved via their electrical impedance. For TCPMs with a resistance that is almost constant regardless of temperature, knowing the input power and measuring inductance already suffices to close the control loop using self-sensing models. However, using a temperature-dependent resistance, and using a measurement thereof, allows for more accurate self-sensing. Static relations suffice to relate electrical impedance to deflection and temperature. However, only a dynamic relation captures the behavior of force. These results strengthen the position of TCPMs as feasible actuators for inexpensive and lightweight control systems.

8.3. FUTURE RESEARCH DIRECTIONS

The work in this thesis provides a number of directions to continue the research and development of self-sensing in coil springs and TCPMs. These recommendations aim at advancing the Technology Readiness Level (TRL) of both technologies [42].

To have self-sensing in coil springs and TCPMs become a generally accepted solution rather than an exception, its properties and performance should be well known and practical implementations should be developed. First, quantifying the variance in the fitted parameters within a single and between equal coil springs and TCPMs could benefit the repeatability of the presented models. Second, varying construction parameters and properties of coil springs and TCPMs could benefit the generalizability of the presented methods. Properties to vary should include the shapes and sizes, and the material and dimensions of the conductor. Third, a study towards potential sources of disturbance and their effects on self-sensing could benefit the applicability in a real-life system. For example, sources of electromagnetic emissions could disturb inductance measurements. Fourth, the scalable application of self-sensing in coil springs and TCPMs requires development of several practical methods to measure electrical impedance, like the method in [43] or the use of [147], like in [63]. It is likely that each solution has its own accuracy, sensitivity to different disturbances, optimal sample rate and cost, and will be suitable for specific applications.

Currently studied TCPMs apply limited forces. In general, single TCPMs have a poor scalability. While for some applications that might suffice, for others it will not. However, the force becomes scalable via structures of multiple TCPMs acting as one actuator. Examples include weaving or bundling several TCPMs into a textile-like structure [49, 132], or giving them a parallel or pennate configuration [66, 182]. This makes TCPMs feasible actuators for a larger range of applications. Studies towards different types of structures and interaction between single TCPMs provide interesting directions of research. For example, the architecture and control of structures can be based on biological muscles [182]. Studies could include the influence of pennation angle, fiber count and variations in construction of a single muscle on force production. These studies could also include challenges for self-sensing, for example regarding interaction of signals between fibers [117]. Furthermore, packing muscles into larger structures makes cooling more difficult and the modeling thereof complex. Future research should study cooling of these structures, without compromising on weight and cost, and provide models to describe the thermodynamics.

Finally, refinement of both self-sensing and control could improve the performance of TCPMs. Both could benefit from more accurate modeling. From the perspective of this thesis, the biggest gain lies at improved force models. Chapter 5 refers to a number of alternative force models. A study that compares these models in one or multiple cases gives insight into their respective qualities. Additionally, study of fractional-order models [4, 58, 124] might provide invaluable insights in modeling the hysteretic behavior of TCPMs. Furthermore, TCPMs suffer from a limited control-action space. Next to improving implementations to expand the control-action space (see Chapter 5), implementation of control methods that are better equipped to deal with a limited control-action space could improve control performance as well.

REFERENCES

[1] Public access to data of Chapter 2, 2015. http://homepage.tudelft.nl/q3p2d/IROS2015/data and analysis.zip.

[2] ABBAS, A., AND ZHAO, J. A Physics Based Model for Twisted and Coiled Actuator. In *IEEE International Conference on Robotics and Automation* (Singapore, 2017), pp. 6121–6126.

[3] ABBAS, A., AND ZHAO, J. Twisted and coiled sensor for shape estimation of soft robots. In *IEEE International Conference on Intelligent Robots and Systems* (2017), vol. September, pp. 482–487.

[4] ADOLFSSON, K., ENELUND, M., AND OLSSON, P. On the Fractional Order Model of Viscoelasticity. *Mechanics of Time-Dependent Materials 9*, 1 (2005), 15–34.

[5] AGICH, G. J. *Dependence and Autonomy in Old Age*, 2 ed. Cambridge University Press, Cambridge, 2003.

[6] ALFORD, M. Attacking Requirements Complexity using a Separation of Concerns. In *IEEE International Conference on Requirements Engineering* (1994), pp. 2–5.

[7] ALI, H. I., BAHARI, S., NOOR, B. M., BASHI, S. M., AND MARHABAN, M. H. A Review of Pneumatic Actuators (Modeling and Control). *Australian Journal of Basic and Applied Sciences 3*, 2 (2009), 440–454.

[8] ALMUBARAK, Y., AND TADESSE, Y. Design and motion control of bioinspired humanoid robot head from servo motors toward artificial muscles. *Proceedings of SPIE 10163* (2017), 10163–9.

[9] ALMUBARAK, Y., AND TADESSE, Y. Twisted and coiled polymer (TCP) muscles embedded in silicone elastomer for use in soft robot. *International Journal of Intelligent Robotics and Applications 1*, 3 (sep 2017), 352–368.

[10] ARAKAWA, T., TAKAGI, K., TAHARA, K., AND ASAKA, K. Position control of fishing line artificial muscles (coiled polymer actuators) from Nylon thread. *Proceedings of SPIE 9798* (2016), 9798–12.

[11] ASADA, H., AND KANADE, T. Design of Direct-Drive Mechanical Arms. *Journal of Vibration, Acoustics, Stress, and Reliability in Design 105*, 3 (1983), 312–316.

[12] ASADA, H., AND YOUCEF-TOUMI, K. *Direct-Drive Robots: Theory and Practice*. The M.I.T. Press, Cambridge, Massachusetts, 1987.

[13] ATHERTON, D. P. *Nonlinear Control Engineering.* Van Nostrand Reinhold Company, Wokingham, Berkshire, 1982.

[14] ATIKAH, N. A., WENG, L. Y., ANUAR, A., AND CHIEN, C. Development of Nylon-Based Artificial Muscles for the Usage in Robotic Prosthetic Limb. In *AIP Conference Proceedings* (2017), vol. 1883, p. 020042.

[15] AZIZ, S., NAFICY, S., FOROUGHI, J., BROWN, H. R., AND SPINKS, G. M. Characterisation of torsional actuation in highly twisted yarns and fibres. *Polymer Testing 46* (jul 2015), 88–97.

[16] AZIZ, S., NAFICY, S., FOROUGHI, J., BROWN, H. R., AND SPINKS, G. M. Controlled and Scalable Torsional Actuation of Twisted Nylon 6 Fiber. *Journal of Polymer Science Part B: Polymer Physics 54*, 13 (2016), 1278–1286.

[17] AZIZ, S., NAFICY, S., FOROUGHI, J., BROWN, H. R., AND SPINKS, G. M. Thermomechanical effects in the torsional actuation of twisted nylon 6 fiber. *Journal of Applied Polymer Science 134*, 47 (2017).

[18] BAUGHMAN, R. H., CUI, C., ZAKHIDOV, A. A., IQBAL, Z., BARISCI, J. N., SPINKS, G. M., WALLACE, G. G., MAZZOLDI, A., DE ROSSI, D., RINZLER, A. G., JASCHINSKI, O., ROTH, S., AND KERTESZ, M. Carbon nanotube actuators. *Science 284*, 5418 (1999), 1340–1344.

[19] BEAUCHET, O., ANNWEILER, C., LECORDROCH, Y., ALLALI, G., DUBOST, V., HERRMANN, F. R., AND KRESSIG, R. W. Walking speed-related changes in stride time variability: effects of decreased speed. *Journal of NeuroEngineering and Rehabilitation 6*, 1 (2009), 32.

[20] BRIDGMAN, P. . W. . The Effect of Tension on the Transverse and Longitudinal Resistance of Metals. *Proceedings of the American Academy of Arts and Sciences 60*, 8 (1925), 423–449.

[21] BROEKENS, J., HEERINK, M., AND ROSENDAL, H. Assistive social robots in elderly care: a review. *Gerontechnology 8*, 2 (2009), 94–103.

[22] BUERGER, S. P. *Stable, High-Force, Low-Impedance Robotic Actuators for Human-Interactive Machines.* PhD thesis, Massachusetts Institute of Technology, 2005.

[23] CALDWELL, D. G. *Compliant Polymeric Actuators.* PhD thesis, Hull, 1989.

[24] CARAYANNIS, E., AND GRIGOROUDIS, E. Linking innovation, productivity, and competitiveness: implications for policy and practice. *Journal of Technology Transfer 39*, 2 (2014), 199–218.

[25] CARROZZA, M. C. *The Robot and Us*, 1 ed. Springer Nature Switzerland, Cham, Switzerland, 2019.

[26] CHERUBINI, A., MORETTI, G., VERTECHY, R., AND FONTANA, M. Experimental characterization of thermally-activated artificial muscles based on coiled nylon fishing lines. *AIP Advances 5*, 6 (2015), 067158.

[27] CHI, S., ZHANG, Z., AND XU, L. Sliding-Mode Sensorless Control of Direct-Drive PM Synchronous Motors for Washing Machine Applications. *IEEE Transactions on Industry Applications 45*, 2 (2009), 582–590.

[28] CHO, K. H., SONG, M. G., JUNG, H., PARK, J., MOON, H., KOO, J. C., NAM, J.-D., AND CHOI, H. R. A robotic finger driven by twisted and coiled polymer actuator. *Proceedings of SPIE 9798* (2016), 9798–7.

[29] CHO, S.-M., AND LEE, D.-W. A biomimetic micro-collector based on an ionic polymer metal composite. *Microelectronic Engineering 86*, 4-6 (2009), 916–919.

[30] CHOY, C. L., CHEN, F. C., AND YOUNG, K. Negative Thermal Expansion in Oriented Crystalline Polymers. *Journal of Polymer Science 19* (1981), 335–352.

[31] CLARK, A., FLÈCHE, S., LAYARD, R., POWDTHAVEE, N., AND WARD, G. *The Origins of Happiness.* Princeton University Press, 2018.

[32] COLGATE, E., AND HOGAN, N. An analysis of contact instability in terms of passive physical equivalents. In *Proceedings, 1989 International Conference on Robotics and Automation* (1989), IEEE Comput. Soc. Press, pp. 404–409.

[33] DAERDEN, F., AND LEFEBER, D. Pneumatic artificial muscles: actuators for robotics and automation. *European Journal of Mechanical and Environmental Engineering 47*, 1 (2002), 11–21.

[34] DE BOER, T. Foot placement in robotic bipedal locomotion. *Delft University of Technology, Netherlands* (2012).

[35] DE KRUIJF, R., AND LANGENBERG, H. Vergrijzing en de Nederlandse economie, 2017. https://www.cbs.nl/nl-nl/achtergrond/2017/11/vergrijzing-en-de-nederlandse-economie.

[36] DOMINICI, N., KELLER, U., VALLERY, H., FRIEDLI, L., VAN DEN BRAND, R., STARKEY, M. L., MUSIENKO, P., RIENER, R., AND COURTINE, G. Versatile robotic interface to evaluate, enable and train locomotion and balance after neuromotor disorders. *Nature Medicine 18* (may 2012), 1142–1147.

[37] DOSCH, J. J., AND INMAN, D. J. Self-Sensing Piezoelectric Actuator for Collocated Control. *Journal of Intelligent Materials Systems and Structures 3*, January (1992), 166–185.

[38] DUERIG, T., MELTON, K., STÖCKEL, D., AND WAYMAN, C. *Engineering Aspects of Shape Memory Alloys.* Butterworth-Heinemann Ltd., 1990.

[39] DYM, C. L. Consistent Derivations of Spring Rates for Helical Springs. *Journal of Mechanical Design 131*, 7 (2009), 071004–071004–5.

[40] EDMONDS, B. P. R., AND TREJOS, A. L. Stiffness Control of a Nylon Twisted Coiled Actuator for Use in Mechatronic Rehabilitation Devices. In *International Conference on Rehabilitation Robotics (ICORR)* (London, 2017), IEEE, pp. 1419–1424.

[41] EUROC. EU project, 2014. http://www.euroc-project.eu/, date accessed: 29-01-2019.

[42] EUROPEAN COMMISSION. Horizon 2020 Technology Readiness Levels, 2017. http://ec.europa.eu/research/participants/data/ref/h2020/other/wp/2016-2017/annexes/h2020-wp1617-annex-ga_en.pdf.

[43] FRITSCHI, M., AND VAN DE KAMP, C. Electrical Displacement-, Load- or Force Sensor, 2018. WO 2018/182405 A1.

[44] GREENBLATT, N. A. Self-driving cars and the law. *IEEE Spectrum 53*, 2 (2016), 46–51.

[45] GRIFFITHS, D. J. *Introduction To Electrodynamics*, 3 ed. Prentice Hall, New Jersey, 1999.

[46] GROVER, F. *Inductance Calculations*. D. Van Nostrand Co., New York, 1946.

[47] GUO, S., FUKUDA, T., KOSUGE, K., ARAI, F., OGURO, K., AND NEGORO, M. Micro Catheter System with Active Guide Wire. In *International Conference on Robotics and Automation* (1995), pp. 79–84.

[48] HAINES, C. S., LI, N., SPINKS, G. M., ALIEV, A. E., DI, J., AND BAUGHMAN, R. H. New twist on artificial muscles. *National Academy of Sciences 113*, 42 (2016), 11709–11716.

[49] HAINES, C. S., LIMA, M. D., LI, N., SPINKS, G. M., FOROUGHI, J., MADDEN, J. D. W., KIM, S. H., FANG, S., JUNG DE ANDRADE, M., GÖKTEPE, F., GÖKTEPE, Ö., MIRVAKILI, S. M., NAFICY, S., LEPRÓ, X., OH, J., KOZLOV, M. E., KIM, S. J., XU, X., SWEDLOVE, B. J., WALLACE, G. G., AND BAUGHMAN, R. H. Artificial Muscles from Fishing Line and Sewing Thread. *Science 343*, 6173 (2014).

[50] HAINES, C. S., AND NIEMEYER, G. Closed-Loop Temperature Control of Nylon Artificial Muscles. In *International Conference on Intelligent Robots and Systems (IROS)* (2018), pp. 6980–6985.

[51] HAM, R., SUGAR, T., VANDERBORGHT, B., HOLLANDER, K., AND LEFEBER, D. Compliant actuator designs. *IEEE Robotics & Automation Magazine 16*, 3 (sep 2009), 81–94.

[52] HERR, H. M., WEBER, J. A., AU, S. K., DEFFENBAUGH, B. W., MAGNUSSON, L. H., HOFMANN, A. G., AND AISEN, B. B. Powered ankle-foot prosthesis, 2005. U.S. patent nr: US2014088729 (A1).

[53] HOGAN, N., KREBS, H., CHARNNARONG, J., SRIKRISHNA, P., AND SHARON, A. MIT-MANUS: a workstation for manual therapy and training. In *IEEE International Workshop on Robot and Human Communication* (1992), pp. 161–165.

[54] HOLLERBACH, J. M., HUNTER, I. W., AND BALLANTYNE, J. A Comparitive Analysis of Actuator Technologies for Robotics. *Robotics Review 2* (1992).

[55] HOWARD, R. D. *Joint and actuator design for enhanced stability in robotic force control.* PhD thesis, Massachusetts Institute of Technology, 1990.

[56] HUTTER, M. *StarlETH & Co . – Design and Control of Legged Robots with Compliant Actuation.* PhD thesis, ETH Zurich, 2013.

[57] IONOV, L. Polymeric Actuators. *Langmuir 31*, 18 (nov 2015), 5015–5024.

[58] ITIK, M., SAHIN, E., AND SINASI, M. Expert Systems with Applications Fractional order control of conducting polymer artificial muscles. *Expert Systems with Applications 42*, 21 (2015), 8212–8220.

[59] JAFARZADEH, M., GANS, N., AND TADESSE, Y. Control of TCP muscles using Takagi-Sugeno-Kang fuzzy inference system. *Mechatronics 53*, March (2018), 124–139.

[60] JANOCHA, H. *Adaptronics and Smart Structures*, 2 ed. Springer Berlin Heidelberg, New York, 2007.

[61] JOHNSON, B. L., AND STEWART, E. E. Transfer Functions for Helical Springs. *Journal of Engineering for Industry 91*, 4 (nov 1969), 1011–1016.

[62] KARAMI, F., AND TADESSE, Y. Modeling of twisted and coiled polymer (TCP) muscle based on phenomenological approach. *Smart Materials and Structures 26*, 12 (2017), 125010.

[63] KASEMSADEH, B. Measuring Spring Compression with an Inductance-to-Digital converter, 2015. https://e2e.ti.com/blogs_/b/analogwire/archive/2015/07/13/inductive-sensing-how-to-sense-spring-compression, date accessed: 12-07-2019.

[64] KATO, Y., SEKITANI, T., TAKAMIYA, M., DOI, M., ASAKA, K., SAKURAI, T., AND SOMEYA, T. Sheet-Type Braille Displays by Integrating Organic Field-Effect Transistors and Polymeric Actuators. *IEEE Transactions on Electron Devices 54*, 2 (2007), 202–209.

[65] KIANZAD, S., PANDIT, M., BAHI, A., RAFIE RAVANDI, A., KO, F., SPINKS, G. M., AND MADDEN, J. D. W. Nylon coil actuator operating temperature range and stiffness. *Proceedings of SPIE 9430* (2015), 9430–6.

[66] KIANZAD, S., PANDIT, M., LEWIS, J. D., BERLINGERI, A. R., HAEBLER, K. J., AND MADDEN, J. D. W. Variable stiffness structure using nylon actuators arranged in a pennate muscle configuration. *Proceedings of SPIE 9430* (2015), 9430–5.

[67] KIM, H., HAN, Y., LEE, D.-Y., HA, J.-I., AND CHO, K.-J. Sensorless displacement estimation of a shape memory alloy coil spring actuator using inductance. *Smart Materials and Structures 22*, 2 (feb 2013), 025001.

[68] KIM, K. J., AND TADOKORO, S., Eds. *Electroactive Polymers for Robotics Applications.* Springer-Verlag London, 2007.

[69] KIM, S. H., LIMA, M. D., KOZLOV, M. E., HAINES, C. S., SPINKS, G. M., AZIZ, S., CHOI, C., SIM, H. J., WANG, X., LU, H., QIAN, D., MADDEN, J. D. W., BAUGHMAN, R. H., AND KIM, S. J. Harvesting temperature fluctuations as electrical energy using torsional and tensile polymer muscles. *Energy & Environmental Science 8*, 11 (2015), 3336—-3344.

[70] KRUUSAMÄE, K., PUNNING, A., AABLOO, A., AND ASAKA, K. Self-Sensing Ionic Polymer Actuators: A Review. *Actuators 4* (2015), 17–38.

[71] KUCZYNSKI, G. Effect of Elastic Strain on the Electrical Resistance of Metals. *Physical Review 94*, 1 (1954), 61–64.

[72] KUMAR, P., AND LAGOUDAS, D. Introduction to Shape Memory Alloys. In *Shape Memory Alloys: Modeling and Engineering Applications*, D. Lagoudas, Ed. Springer Science + Business Media, New York, NY, 2008, ch. 1, pp. 1–52.

[73] LAGODA, C., SCHOUTEN, A. C., STIENEN, A. H. A., HEKMAN, E. E. G., AND KOOIJ, H. V. D. rehabilitation training. In *IEEE RAS & EMBS International Conference on Biomedical Robotics and Biomechatronics* (2010), IEEE, pp. 21–26.

[74] LAMUTA, C., MESSELOT, S., AND TAWFICK, S. Theory of the tensile actuation of fiber reinforced coiled muscles. *Smart Materials and Structures 27*, 5 (2018), 55018.

[75] LEE, J., AND THOMPSON, D. Dynamic Stiffness Formulation, Free Vibration and Wave Motion of Helical Springs. *Journal of Sound and Vibration 239*, 2 (jan 2001), 297–320.

[76] LEE, S.-H., KIM, T. H., LIMA, M. D., BAUGHMAN, R. H., AND KIM, S. J. Biothermal sensing of a torsional artificial muscle. *Nanoscale 8* (2016), 3248–3253.

[77] LEMUS, D., VAN FRANKENHUYZEN, J., AND VALLERY, H. Design and Evaluation of a Balance Assistance Control Moment Gyroscope. *Journal of Mechanisms and Robotics 9*, 5 (2017), 051007–051007–9.

[78] LI, T., WANG, Y., LIU, K., LIU, H., ZHANG, J., SHENG, X., AND GUO, D. Thermal actuation performance modification of coiled artificial muscle by controlling annealing stress. *Journal of Polymer Science Part B: Polymer Physics 56*, 5 (2018), 383–390.

[79] LIU, Z. F., FANG, S., MOURA, F. A., DING, J. N., JIANG, N., DI, J., ZHANG, M., LEPRO, X., GALVAO, D. S., HAINES, C. S., YUAN, N. Y., YIN, S. G., LEE, D. W., WANG, R., WANG, H. Y., LV, W., DONG, C., ZHANG, R. C., CHEN, M. J., YIN, Q., CHONG, Y. T., ZHANG, R., WANG, X., LIMA, M. D., OVALLE-ROBLES, R., QIAN, D., LU, H., AND BAUGHMAN, R. H. Hierarchically buckled sheath-core fibers for superelastic electronics, sensors and muscles. *Science 349*, 6246 (2015), 400–404.

[80] LOVE, A. E. H. *A Treatise on the Mathematical Theory of Elasticity*. Cambridge University Press, Cambridge, UK, 1959.

[81] LUONG, T. A., SEO, S., KOO, J. C., CHOI, H. R., AND MOON, H. Differential hysteresis modeling with adaptive parameter estimation of a super-coiled polymer actuator. In *International Conference on Ubiquitous Robots and Ambient Intelligence (URAI)* (2017), pp. 607–612.

[82] MADDEN, D. J. W. *Conducting Polymer Actuators.* PhD thesis, Massachusetts Institute of Technology, 2000.

[83] MASUYA, K., ONO, S., TAKAGI, K., AND TAHARA, K. Modeling framework for macroscopic dynamics of twisted and coiled polymer actuator driven by Joule heating focusing on energy and convective heat transfer. *Sensors & Actuators: A. Physical 267* (2017), 443–454.

[84] MASUYA, K., ONO, S., TAKAGI, K., AND TAHARA, K. Feedforward Control of Twisted and Coiled Polymer Actuator based on a Macroscopic Nonlinear Model Focusing on Energy. *IEEE Robotics and Automation Letters 3*, 3 (2018), 1824 – 1831.

[85] MAXWELL, J. A treatise on electricity and magnetism, 1873.

[86] MCEVOY, M. A., AND CORRELL, N. Materials that couple sensing, actuation, computation, and communication. *Science 347*, 6228 (2015).

[87] MEIER, F. *Permanent-Magnet Synchronous Machines with Non-Overlapping Concentrated Windings for Low-Speed Direct-Drive Applications.* PhD thesis, Royal Institute of Technology, 2008.

[88] MENDES, S. S., AND NUNES, L. C. S. Experimental approach to investigate the constrained recovery behavior of coiled monofilament polymer fibers. *Smart Materials and Structures 26*, 11 (2017), 115031.

[89] MERGNER, T., SCHWEIGART, G., AND FENNELL, L. Vestibular humanoid postural control. *Journal of Physiology Paris 103*, 3-5 (2009), 178–194.

[90] MIRFAKHRAI, T., MADDEN, J. D. W., AND BAUGHMAN, R. H. Polymer artificial muscles. *Materials Today 10*, 4 (2007), 30–38.

[91] MIRVAKILI, S. M., AND HUNTER, I. W. Artificial Muscles: Mechanisms, Applications, and Challenges. *Advanced Materials 30*, 6 (2018).

[92] MIRVAKILI, S. M., RAFIE RAVANDI, A., HUNTER, I. W., HAINES, C. S., LI, N., FOROUGHI, J., NAFICY, S., SPINKS, G. M., BAUGHMAN, R. H., AND MADDEN, J. D. W. Simple and strong: twisted silver painted nylon artificial muscle actuated by Joule heating. *Proceedings of SPIE 9056* (2014), 9056–10.

[93] MOHD JANI, J., LEARY, M., SUBIC, A., AND GIBSON, M. A. A review of shape memory alloy research, applications and opportunities. *Materials and Design 56* (2014), 1078–1113.

[94] MOJARRAD, M., AND SHAHINPOOR, M. Biomimetic Robotic Propulsion Using Polymeric Artificial Muscles. In *IEEE International Conference on Robotics and Automation* (1997), no. April, pp. 2152–2157.

[95] NAGAOKA, H. The Inductance Coefficients of Solenoids. *Journal of the College of Science, Imperial University 27*, 6 (1909), 1–33.

[96] NISSAN. Nissan Leaf power train, 2018. https://www.nissan-global.com/EN/TECHNOLOGY/OVERVIEW/e_powertrain.html, date accessed: 18-12-2018.

[97] OIWA, C., MASUYA, K., TAHARA, K., IRISAWA, T., SHIOYA, M., YAMAUCHI, T., TANAKA, E., ASAKA, K., AND TAKAGI, K. Gray-box modeling and control of torsional fishing-line artificial muscle actuators. *Proceedings of SPIE 10594* (2018), 10594–11.

[98] ONO, S., MASUYA, K., TAKAGI, K., AND TAHARA, K. Trajectory Tracking of a One-DOF Manipulator using Multiple Fishing Line Actuators by Iterative Learning Control. In *IEEE International Conference on Soft Robotics (RoboSoft)* (2018), IEEE, pp. 467–472.

[99] OTERO, T. F., AND MARTINEZ, J. G. Physical and chemical awareness from sensing polymeric artificial muscles . Experiments and modeling. *Progress in Polymer Science 44* (2015), 62–78.

[100] PAINE, N., MEHLING, J. S., HOLLEY, J., RADFORD, N. A., JOHNSON, G., FOK, C.-L., AND SENTIS, L. Actuator Control for the NASA-JSC Valkyrie Humanoid Robot : A Decoupled Dynamics Approach for Torque Control of Series Elastic Robots. *Journal of Field Robotics 32*, 3 (2015), 378–396.

[101] PARIETTI, F., BAUD-BOVY, G., GATTI, E., RIENER, R., GUZZELLA, L., AND VALLERY, H. Series Viscoelastic Actuators Can Match Human Force Perception. *IEEE/ASME Transactions on Mechatronics 16*, 5 (oct 2011), 853–860.

[102] PAUL, C. R., WHITES, K. W., AND NASAR, S. A. *Introduction to Electromagnetic Fields*, 3 ed. McGraw-Hill, New York, 1987.

[103] PEERDEMAN, B., SMIT, G., STRAMIGIOLI, S., PLETTENBURG, D. H., AND MISRA, S. Evaluation of Pneumatic Cylinder Actuators for Hand Prostheses. In *IEEE RAS/EMBS International Conference on Biomedical Robotics and Biomechatronics* (2012), pp. 1104–1109.

[104] PELRINE, R., KORNBLUH, R., PEI, Q., STANFORD, S., OH, S., ECKERLE, J., FULL, R., ROSENTHAL, M., AND MEIJER, K. Dielectric elastomer artificial muscle actuators : toward biomimetic motion. *Proceedings of SPIE 4695*, July 2002 (2002), 126–137.

[105] PELRINE, R., SOMMER-LARSEN, P., KORNBLUH, R. D., HEYDT, R., KOFOD, G., PEI, Q., AND GRAVESEN, P. Applications of dielectric elastomer actuators. *Proceedings of SPIE 4329* (2001), 1–15.

[106] PFEIFER, S., PAGEL, A., MEMBER, S., AND RIENER, R. Actuator with Angle-Dependent Elasticity for Biomimetic Transfemoral Prostheses. *IEEE/ASME Transactions on Mechatronics 20*, 3 (2014), 1384–1394.

[107] PLETTENBURG, D. H. Pneumatic Actuators : a Comparison of Energy-to-Mass Ratio ' s. In *IEEE International Conference on Rehabilitation Robotics (ICORR)* (2005), pp. 545–549.

[108] PRATT, G., AND WILLIAMSON, M. Series elastic actuators. *Proceedings 1995 IEEE/RSJ International Conference on Intelligent Robots and Systems. Human Robot Interaction and Cooperative Robots 1* (1995), 399–406.

[109] PRATT, G. A., WILLIAMSON, M. M., DILLWORTH, P., PRATT, J., ULLAND, K., AND WRIGHT, A. Stiffness Isn ' t Everything. In *Experimental Robotics IV* (1997), Springer Berlin Heidelberg, pp. 253—-262.

[110] PRATT, J., DILWORTH, P., AND PRATT, G. Virtual model control of a bipedal walking robot. In *Proceedings of International Conference on Robotics and Automation* (1997), vol. 1, IEEE, pp. 193–198.

[111] PRATT, J., KOOLEN, T., BOER, T. D., REBULA, J., COTTON, S., CARFF, J., JOHNSON, M., AND NEUHAUS, P. Capturability-based analysis and control of legged locomotion , Part 2 : Application to M2V2 , a lower-body humanoid. *The International Journal of Robotics Research 31*, 10 (2012), 1117–1133.

[112] PUNNING, A., KRUUSMAA, M., AND AABLOO, A. A self-sensing ion conducting polymer metal composite (IPMC) actuator. *Sensors & Actuators: A. Physical 136* (2007), 656–664.

[113] RAGONESI, D., AGRAWAL, S., SAMPLE, W., AND RAHMAN, T. Series Elastic Actuator Control of a Powered Exoskeleton. *IEEE International Conference on Engineering in Medicine and Biology* (2011), 3515–3518.

[114] RAJENDRAN, S. K., AND ZHANG, F. Developing a Novel Robotic Fish With Antagonistic Artificial Muscle Actuators. In *ASME Dynamic Systems and Control Conference* (2017), p. V001T30A011.

[115] ROBINSON, D. W. *Design and Analysis of Series Elasticity in Closed-loop Actuator Force Control.* PhD thesis, Massachusetts Institute of Technology, 2000.

[116] ROBINSON, H., MACDONALD, B., AND BROADBENT, E. The Role of Healthcare Robots for Older People at Home : A Review. *International Journal of Social Robotics 6*, 4 (2014), 575–591.

[117] RÖLING, M. Effect of series versus parallel electrical configuration on self-sensing in a structure of twisted and coiled polymer muscles. Tech. rep., Delft University of Technology, 2017.

[118] ROSA, E. B. Calculation of the self-inductance of single-layer coils. *Bulletin of the Bureau of Standards 2*, 2 (1906), 161–187.

[119] ROUSE, E. J., MOONEY, L. M., MARTINEZ-VILLALPANDO, E. C., AND HERR, H. M. Clutchable Series-Elastic Actuator : Design of a Robotic Knee Prosthesis for Minimum Energy Consumption. In *International Conference on Rehabilitation Robotics* (2013).

[120] ROYLANCE, D. *Engineering Viscoelasticity*. MIT Press, Cambridge, Massachusetts, 2001.

[121] SAHARAN, L., SHARMA, A., ANDRADE, M. J. D., BAUGHMAN, R. H., AND TADESSE, Y. Design of a 3D Printed Lightweight Orthotic Device Based on Twisted and Coiled Polymer Muscle : iGrab Hand Orthosis. *Proceedings of SPIE 10164* (2017), 10164–10.

[122] SAHARAN, L., AND TADESSE, Y. A Novel Design of Thermostat Based on Fishing Line Muscles. In *ASME International Mechanical Engineering Congress and Exposition (IMECE)* (Phoenix, 2016), no. November, ASME, p. V014T07A019.

[123] SAHARAN, L., AND TADESSE, Y. Fabrication Parameters and Performance Relationship of Twisted and Coiled Polymer Muscles. In *ASME International Mechanical Engineering Congress and Exposition (IMECE)* (Phoenix, 2016), no. November, ASME, p. V014T11A028.

[124] SCHIESSEL, H., METZLER, R., BLUMEN, A., AND NONNENMACHER, T. Generalized viscoelastic models: their fractional equations with solutions. *Journal of Physics A: Mathematical and General 28*, 23 (1995), 6567–6584.

[125] SCHROEDER, M. R. Synthesis of Low-Peak-Factor Signals and Binary Sequences with Low Autocorrelation. *IEEE Transactions on Information Theory 16*, 1 (1970), 85–89.

[126] SEMOCHKIN, A. N. A Device for Producing Artificial Muscles from Nylon Fishing Line with a Heater Wire. In *IEEE International Symposium on Assembly and Manufacturing (ISAM)* (2016), pp. 26–30.

[127] SERWAY, R. A., AND JEWETT, J. W. *Physics for Scientists and Engineers*, 9 ed. Brooks/Cole, 2013.

[128] SHAFER, M. W., FEIGENBAUM, H. P., AND RUIZ, D. R. H. A Novel Biomimetic Torsional Actuator Design using Twisted Polymer Actuators. In *ASME Conference on Smart Materials, Adaptive Structures and Intelligent Systems* (2017), p. V001T06A006.

[129] SHAHINPOOR, M., BAR-COHEN, Y., SIMPSON, J. O., AND SMITH, J. Ionic polymer-metal composites (IPMCs) as biomimetic sensors , actuators and artificial muscles - a review. *Smart Materials and Structures 7*, 6 (1998), 15–30.

[130] SHARAFI, S., AND LI, G. A multiscale approach for modeling actuation response of polymeric artificial muscles. *Soft matter 11*, 19 (may 2015), 3833–3843.

[131] SHATZ, L. F., AND CHRISTENSEN, C. W. Numerical inductance calculations based on first principles. *PLoS ONE 9*, 11 (2014), 1–8.

[132] SIMEONOV, A., HENDERSON, T., LAN, Z., SUNDAR, G., FACTOR, A., ZHANG, J., AND YIP, M. Bundled Super-Coiled Polymer Artificial Muscles : Design , Characterization , and Modeling. *IEEE Robotics and Automation Letters 3*, 3 (2018), 1671 – 1678.

[133] SNOW, C. Formula for the Inductance of a Helix Made With Wire of Any Section. *Scientific Papers of the Bureau of Standards 21* (1926).

[134] SONG, H., AND HORI, Y. Force control of twisted and coiled polymer actuators via active control of electrical heating and forced convective liquid cooling. *Advanced Robotics* (2018), 1–14.

[135] STEELE, J. R., GHO, S. A., CAMPBELL, T. E., RICHARDS, C. J., BEIRNE, S., SPINKS, G. M., AND WALLACE, G. G. The Bionic Bra : Using electromaterials to sense and modify breast support to enhance active living. *Journal of Rehabilitation and Assistive Technologies Engineering 5* (2018), 1–9.

[136] SUTTON, L., MOEIN, H., RAFIEE, A., MADDEN, J. D. W., AND MENON, C. Design of an Assistive Wrist Orthosis Using Conductive Nylon Actuators. In *International Conference on Biomedical Robotics and Biomechatronics (BioRob)* (Singapore, 2016), pp. 1074–1079.

[137] SUZUKI, M., AND KAMAMICHI, N. Control of twisted and coiled polymer actuator with anti-windup compensator. *Smart Materials and Structures 27*, 7 (2018), 075014.

[138] SUZUKI, M., AND KAMAMICHI, N. Displacement control of an antagonistic-type twisted and coiled polymer actuator. *Smart Materials and Structures 27*, 3 (2018), 35003.

[139] TAHARA, K., HAYASHI, R., MASUYA, K., TAKAGI, K., IRISAWA, T., YAMAUCHI, T., AND TANAKA, E. Rotational Angle Control of a Twisted Polymeric Fiber Actuator by an Estimated Temperature Feedback. *IEEE Robotics and Automation Letters* (2019).

[140] TAKAGI, K., ARAKAWA, T., TAKEDA, J., MASUYA, K., TAHARA, K., AND ASAKA, K. Position Control of Twisted and Coiled Polymer Actuator Using a Controlled Fan for Cooling. *Proceedings of SPIE 10163* (2017), 10163–8.

[141] TAMAGAWA, H., LIN, W., KIKUCHI, K., AND SASAKI, M. Chemical Bending control of Nafion-based electroactive polymer actuator coated with multi-walled carbon nanotubes. *Sensors & Actuators: B. Chemical 156*, 1 (2011), 375–382.

[142] TANG, X., LI, K., CHEN, W., ZHOU, D., LIU, S., ZHAO, J., AND LIU, Y. Temperature self-sensing and closed-loop position control of twisted and coiled actuator. *Sensors & Actuators: A. Physical 285* (2019), 319–328.

[143] TANG, X., LI, K., LIU, Y., AND ZHAO, J. Coiled Conductive Polymer Fiber Used in Soft Manipulator as Sensor. *IEEE Sensors Journal 18*, 15 (2018), 6123–6129.

[144] TANG, X., LIU, Y., LI, K., CHEN, W., AND ZHAO, J. Finite element and analytical models for twisted and coiled actuator. *Materials Research Express 5*, 1 (2018), 15701.

[145] TESLA. Tesla power train, 2008. https://www.tesla.com/nl_NL/blog/engineering-update-powertrain-15, date accessed: 18-12-2018.

[146] TESLA. Tesla autonomous driving, 2019. https://www.tesla.com/autopilot, date accessed: 28-01-2019.

[147] TEXAS-INSTRUMENTS. Inductance-to-digital converter, 2019. http://www.ti.com/product/LDC1612 , date accessed: 12-07-2019.

[148] TONDU, B., BOITIER, V., AND LOPEZ, P. Naturally Compliant Robot-Arms Actuated By McKibben Artificial Muscles. In *IEEE International Conference on Systems, Man and Cybernetics* (1994), pp. 2635–2640.

[149] TONDU, B., AND LOPEZ, P. Modeling and Control of McKibben Artificial Muscle Robot Actuators. *IEEE Control Systems 20*, 2 (2000), 15–38.

[150] TSAGARAKIS, N., AND CALDWELL, D. G. Development and Control of a 'Soft-Actuated' Exoskeleton for Use in Physiotherapy and Training. *Autonomous Robots 15*, 1 (2003), 21–33.

[151] TSAGARAKIS, N. G., CALDWELL, D. G., NEGRELLO, F., CHOI, W., BACCELLIERE, L., LOC, V. G., NOORDEN, J., MURATORE, L., MARGAN, A., CARDELLINO, A., NATALE, L., HOFFMAN, E. M., DALLALI, H., KASHIRI, N., MALZAHN, J., LEE, J., KRYCZKA, P., KANOULAS, D., GARABINI, M., CATALANO, M., FERRATI, M., VARRICCHIO, V., PALLOTTINO, L., PAVAN, C., BICCHI, A., SETTIMI, A., ROCCHI, A., AND AJOUDANI, A. WALK-MAN : A High-Performance Humanoid Platform for Realistic Environments. *Journal of Field Robotics 34*, 7 (2017), 1225–1259.

[152] TULLEKEN, H. J. Generalized binary noise test-signal concept for improved identification-experiment design. *Automatica 26*, 1 (1990), 37–49.

[153] VALLERY, H., LUTZ, P., VON ZITZEWITZ, J., RAUTER, G., FRITSCHI, M., EVERARTS, C., RONSSE, R., CURT, A., AND BOLLIGER, M. Multidirectional transparent support for overground gait training. *IEEE International Conference on Rehabilitation Robotics* (2013), 1–7.

[154] VALLERY, H., VENEMAN, J., VAN ASSELDONK, E., EKKELENKAMP, R., BUSS, M., AND VAN DER KOOIJ, H. Compliant actuation of rehabilitation robots. *IEEE Robotics & Automation Magazine 15*, 3 (sep 2008), 60–69.

[155] VAN DER WEIJDE, J. O., SMIT, B., FRITSCHI, M., VAN DE KAMP, C., AND VALLERY, H. Self-Sensing of Deflection, Force, and Temperature for Joule-Heated Twisted and Coiled Polymer Muscles via Electrical Impedance. *IEEE/ASME Transactions on Mechatronics 22*, 3 (jun 2017), 1268–1275.

[156] VAN DER WEIJDE, J. O., VLASBLOM, E., DOBBE, P., VALLERY, H., AND FRITSCHI, M. Force sensing for compliant actuators using coil spring inductance. In *2015 IEEE/RSJ International Conference on Intelligent Robots and Systems (IROS)* (sep 2015), IEEE, pp. 2692–2697.

[157] VAN HAM, R., VANDERBORGHT, B., VAN DAMME, M., VERRELST, B., AND LEFEBER, D. MACCEPA, the mechanically adjustable compliance and controllable equilibrium position actuator: Design and implementation in a biped robot. *Robotics and Autonomous Systems 55*, 10 (oct 2007), 761–768.

[158] VAN LAMSWEERDE, A. Goal-Oriented Requirements Engineering : A Guided Tour. In *IEEE International Symposium on Requirements Engineering* (2001), pp. 249–262.

[159] VANDERBORGHT, B., ALBU-SCHAEFFER, A., BICCHI, A., BURDET, E., CALDWELL, D., CARLONI, R., CATALANO, M., EIBERGER, O., FRIEDL, W., GANESH, G., GARABINI, M., GREBENSTEIN, M., GRIOLI, G., HADDADIN, S., HOPPNER, H., JAFARI, A., LAFFRANCHI, M., LEFEBER, D., PETIT, F., STRAMIGIOLI, S., TSAGARAKIS, N., VAN DAMME, M., VAN HAM, R., VISSER, L., AND WOLF, S. Variable impedance actuators: A review. *Robotics and Autonomous Systems 61*, 12 (dec 2013), 1601–1614.

[160] VENEMAN, J. F., EKKELENKAMP, R., KRUIDHOF, R., VAN DER HELM, F. C., AND VAN DER KOOIJ, H. A Series Elastic- and Bowden-Cable-Based Actuation System for Use as Torque Actuator in Exoskeleton-Type Robots. *The International Journal of Robotics Research 25*, 3 (mar 2006), 261–281.

[161] VERL, A., ALBU-SCHAFFER, A., BROCK, O., AND RAATZ, A., Eds. *Soft Robotics*. Springer Berlin Heidelberg, 2015.

[162] VYSOCKY, A., AND NOVAK, P. Human-Robot Collaboration in Industry. *MM (Modern Machinery) Science Journal*, June (2016), 903–906.

[163] WAHL, A. M. *Mechanical springs*, 2 ed. McGraw-Hill Book Company, New York, 1963.

[164] WANG, S., MEIJNEKE, C., AND VAN DER KOOIJ, H. Modeling, design, and optimization of Mindwalker series elastic joint. *IEEE ... International Conference on Rehabilitation Robotics : [proceedings] 2013* (jun 2013), 6650381.

[165] WANG, S., WANG, L., MEIJNEKE, C., ASSELDONK, E. V., HOELLINGER, T., CHERON, G., IVANENKO, Y., SCALEIA, V. L., SYLOS-LABINI, F., MOLINARI, M., TAMBURELLA, F., PISOTTA, I., THORSTEINSSON, F., ILZKOVITZ, M., GANCET, J., NEVATIA, Y., ZANOW, F., AND VAN DER KOOIJ, H. Design and Control of the MINDWALKER Exoskeleton. *IEEE Transactions on Neural Systems and Rehabilitation Engineering 23*, 2 (2015), 277 – 286.

[166] WAYMO. Waymo, 2019. https://waymo.com/tech/, date accessed: 28-01-2019.

[167] WEAVER, R. S. The Inductance of a Helix of Any Pitch, 2011. unpublished, available: http://electronbunker.ca/DLpublic/HelicalInductance.pdf.

[168] WEHNER, M., QUINLIVAN, B., AUBIN, P. M., MARTINEZ-VILLALPANDO, E., BAUMANN, M., STIRLING, L., HOLT, K., WOOD, R., AND WALSH, C. A lightweight soft exosuit for gait assistance. In *IEEE International Conference on Robotics and Automation* (2013), pp. 3362–3369.

[169] WINTERS, J. M. Hill-Based Muscle Models: A Systems Engineering Perspective. In *Multiple Muscle Systems*. Springer, New York, NY, 1990, pp. 69–93.

[170] WISSE, M., AND VAN DER LINDE, R. Q. *Delft Pneumatic Bipeds*. Springer-Verlag Berlin Heidelberg, 2007.

[171] WU, L., ANDRADE, M. J. D., BRAHME, T., TADESSE, Y., AND BAUGHMAN, R. H. A reconfigurable robot with tensegrity structure using nylon artificial muscle. *Proceedings of SPIE 9799* (2016), 9799–11.

[172] WU, L., ANDRADE, M. J. D., SAHARAN, L. K., ROME, R. S., BAUGHMAN, R. H., AND TADESSE, Y. Compact and low-cost humanoid hand powered by nylon artificial muscles. *Bioinspiration & Biomimetics 12*, 2 (2017), 026004.

[173] WU, L., CHAUHAN, I., AND TADESSE, Y. A Novel Soft Actuator for the Musculoskeletal System. *Advanced Materials Technologies 3*, 5 (2018), 1700359.

[174] WU, L., JUNG DE ANDRADE, M., ROME, R. S., HAINES, C., LIMA, M. D., BAUGHMAN, R. H., AND TADESSE, Y. Nylon-muscle-actuated robotic finger. *Proceedings of SPIE 9431* (2015), 9431–12.

[175] WU, L., AND TADESSE, Y. Modeling of the Electrical Resistance of TCP Muscle. In *ASME International Mechanical Engineering Congress and Exposition (IMECE)* (Tampa, 2017), ASME, p. V04AT05A024.

[176] X-ACT. EU project, 2012. http://www.xact-project.eu/, date accessed: 29-01-2019.

[177] XIANG, C., YANG, H., SUN, Z., XUE, B., HAO, L., RAHOMAN, M. D. A., AND DAVIS, S. The design, hysteresis modeling and control of a novel SMA-fishing-line actuator. *Smart Materials and Structures 26*, 3 (2017), 037004.

[178] YANG, Q., AND LI, G. A top-down multi-scale modeling for actuation response of polymeric artificial muscles. *Journal of the Mechanics and Physics of Solids 92* (2016), 237–259.

[179] YIN, H., ZHOU, J., LI, J., AND JOSEPH, V. S. Fabrication and Properties of Composite Artificial Muscles Based on Nylon and a Shape Memory Alloy. *Journal of Materials Engineering and Performance 27*, 7 (2018), 3581–3589.

[180] YIP, M. C., AND NIEMEYER, G. High-performance robotic muscles from conductive nylon sewing thread. In *2015 IEEE International Conference on Robotics and Automation (ICRA)* (Seattle, may 2015), IEEE, pp. 2313–2318.

[181] YIP, M. C., AND NIEMEYER, G. On the Control and Properties of Supercoiled Polymer Artificial Muscles. *Transactions on Robotics 33*, 3 (2017), 689 – 699.

[182] ZELVYTE, A. Characterization and Modeling of a Bioinspired Artificial Muscle Structure made of Twisted and Coiled Polymer Actuators. Tech. rep., Delft University of Technology, 2018.

[183] ZHANG, J., IYER, K., SIMEONOV, A., AND YIP, M. C. Modeling and Inverse Compensation of Hysteresis in Supercoiled Polymer Artificial Muscles. *IEEE Robotics and Automation Letters 2*, 2 (2017), 773–780.

[184] ZHANG, P., AND LI, G. Fishing line artificial muscle reinforced composite for impact mitigation and on-demand damage healing. *Journal of Composite Materials 50*, 30 (2016), 4235–4249.

[185] ZHANG, W., GUO, S.-X., AND ASAKA, K. A New Type of Hybrid Fish-like Microrobot. *International Journal of Automation and Computing 4* (2006), 358–365.

[186] ZIEGLER, J., AND NICHOLS, N. Optimum Settings for Automatic Controllers, 1942.

[187] ZUR, H., AND WIESSNER, F. Application of Mechanical Springs as Inductive Position Sensors. In *SENSOR* (2013), pp. 706–708.

A

Overview of Compliant Actuators

Today there exists a wide variety of compliant actuators. It includes direct-drive motors, pneumatic actuators, shape-memory alloys, series elastic actuators, artificial muscles, and twisted and coiled polymer muscles. This appendix gives a rough description of their properties and applications. Table A.1 compares indicative quantities of actuator properties.

Direct-drive motors [12, 22] are commercially available actuators that excel at force regulation. However, that comes at the cost of a low force density and a large form factor. A number of applications uses this type of actuator, including: robot arms [11, 53], electric cars [96, 145], ship propulsion [87], elevators [87], and a variety of consumer electronics, like washing machines [27, 87].

Pneumatic actuators [7, 22, 33, 107, 149] are lightweight commercially available motors, with a medium-high force density. However, they are still quite large, they need a source of pressured air, and are not equipped to accurately render forces. Their applications include exoskeletons [150], robot arms [148], soft manipulators [161], humanoid robots [170] and prostheses [103].

Table A.1: Representative actuator properties [49, 54, 115, 164]. This comparison is not based on a thorough review of existing literature. Hence, the numbers indicate an order of magnitude.

	Work/Mass	Power/Mass
Direct drive	15 Nm/kg	200 W/kg
Pneumatic	20 Nm/kg	200 W/kg
Shape-memory alloy	1 Nm/kg	6 W/kg
Series Elastic Actuation	33 Nm/kg	500 W/kg
Artificial Muscles	17 Nm/kg	6 W/kg
Twisted and Coiled Polymer Muscles	2480 Nm/kg	27000 W/kg

Shape-memory alloys [38, 72, 93] are commercially available, small and quiet actuators. However, they are inefficient and expensive, and have a low bandwidth. Applications that use shape-memory alloys include cars, planes, robotics and biomedical devices [38, 72, 93].

Series (variable) elastic actuators [22, 55, 106, 108, 159] are usually purpose-built actuators made of mostly commercially available parts. They have a high force density, and are well equipped to render accurate forces. However, these motors have a relatively large form factor. Their applications include (humanoid) robots [34, 56, 100, 110, 111, 151, 157, 161], prostheses [52, 106, 119] and exoskeletons [73, 113, 160, 165].

Artificial muscles [18, 23, 49, 68, 90, 91] are typically small and quiet polymeric or composite actuators. The variety of artificial muscles expand or contract in reaction to different stimuli, like electrical or magnetic fields, chemical potentials, thermal energy or fluid pressure. Properties like force density, efficiency and bandwidth vary with the different types of artificial muscle [91, 105]. Common disadvantages include the sometimes impractical or dangerous stimuli, like chemical potentials and high voltages, and poor commercial availability. Applications include grippers [129], several swimming [94, 185], flying [104], walking [104], or other microrobots [68], biomedical instruments [29, 47], and tactile displays [64, 68].

The Twisted and Coiled Polymer Muscle (TCPM) [49] is a recent development in the field of polymeric artificial muscles. The mostly nylon-fiber-based muscle contracts or expands in reaction to, for example, temperature changes induced by Joule heating. It is low cost and low weight, scalable by increasing the number of fibers, and easy to fabricate and integrate. Moreover, it surpasses biological muscle and most artificial muscles on a number of properties, like power-to-weight ratio and stroke length. Unfortunately, its energy conversion efficiency lies in the order of magnitude of shape memory alloys, which is well below that of biological muscle. Applications include robotic fingers [28, 59, 174, 180, 181], a robot arm [183], orthoses [121, 136], silicon manipulators [9], complete robots [114, 171], and a self-adjusting sports bra [135]. Chapter 5 contains a more detailed description of the working principle of TCPMs, its state of the art, and its applications.

ACKNOWLEDGEMENTS

Getting to this point in my academic career has been quite the experience. The help and company of several people have been instrumental to the content and quality of this work, and to making the journey enjoyable.

First, I am grateful to my promotors: Heike Vallery, Robert Babuška, Ron van Ostayen, and, even though not officially a promotor, Just Herder. To all of you: thank you for taking me on as the candidate to execute the original project on *Shaping nonlinear impedance for bipedal locomotion*. The direction of the project has changed, but all of you were invaluable to what it turned out to be.

Heike, thank you for pushing me forward when I stagnated. I appreciate your eye for detail and your rigor on all facets of my research and education. I might have been a bit reluctant every now and again, but your guidance shaped me and my work for the better; following your suggestions always improved the result.

Robert, thank you for your patience and for believing in me. The project contained a bit less content related to control than you are used to. Nevertheless, I could always count on your guidance and advice; both on the content and on the process.

Ron, thank you for many interesting discussions on varying multi-physical topics. You kept me sharp by always pointing out something that could use a bit more attention. Your feedback always triggered ideas.

Just, thank you for your support. When some ideas seemed far fetched, you managed to boil it down to a relevant contribution. It is a pity that I can *only* have three promotors.

I would also like to thank several people that coauthored some of the work in this thesis. Erik, Michael, Cornelis and Bram, it has been a pleasure collaborating with you.

I also had help in preparing experiments. Jan, thanks for your technical advice and support. You have definitely improved my design skills. Those mandrels came out nice.

To Erik, Ivan, Carlos and Mukunda: thanks for being great colleagues and friends. I've always enjoyed our scientific (and non-scientific) discussions, and the dinners we had during some of those.

Next to the colleagues mentioned earlier, I would also like to thank my other colleagues in DBL: Gijs, Michiel, Wouter, Jeff, Martijn, Daniel, Andy, Patricia, Saher, Ruben. We have done a lot of things that made working together great. On the top of my mind are foosball, going to gym, lunches, VrijMiBo and Feuerzangenbowle. Thanks!

There have also been some passersby: Stefan, Manuel, Alberto and Christian. In a short time, all of you have made a lasting impression. Thanks for some great moments.

I have also had the pleasure of guiding some students through their masters research. Bram, Guido, Wouter, Aureja, Marloes and Kjartan, thanks for your trust. Guiding you guys gave me a lot of inspiration for my own work.

Last, but certainly not least: I would like to thank all of my family and friends for bearing with me through this journey. A special thanks to my parents and to my wife: it has not always been easy, but I always received your love and support when I needed it.

Curriculum Vitæ

Johannes Oosten van der Weijde

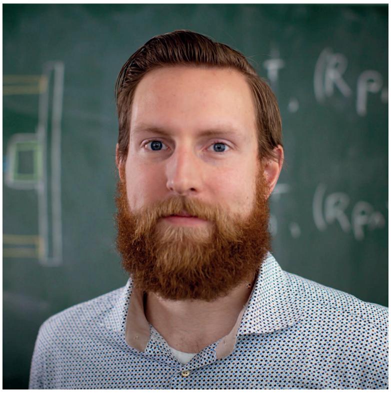

Born:
June 12th 1988
Haarlemmermeer, The Netherlands.

2000–2006 VWO at Herbert Vissers College in Nieuw Vennep
Profile: Nature and Technology & Nature and Health

2006–2012 Bachelor of Science in Mechanical Engineering
Delft University of Technology
Minor: Applied Sustainable Science Engineering and Technology
Thesis: High-Precision Positioning using Ferro-Fluid Bearings

2012–2014 Master of Science in Mechanical Engineering
Delft University of Technology
Track: BioMechanical Engineering - Biorobotics
Thesis: Controller Design for Robust Limit-Cycle Walking
Internship: Design of a fractional-order integrator for high-precision stages

2014–2019 Doctoral Research and Education
Delft University of Technology

List of Publications

Journal papers

5. **J.O. van der Weijde**, H. Vallery and R. Babuška *Closed-Loop Control Through Self-Sensing of a Joule-Heated Twisted and Coiled Polymer Muscle*, Mary-Ann Liebert's Soft Robotics, Vol. 6, Issue 5, pp. 621 – 630 (2019).

4. **J.O. van der Weijde**, R. van Ostayen and H. Vallery *Influence of Internal Oscillations on Force Sensing in Coil Springs*, IEEE Robotics and Automation Letters, Vol. 2, Issue 3, pp. 1466 - 1471 (2017).

3. **J.O. van der Weijde**, B. Smit, M. Fritschi, C. van de Kamp and H. Vallery *Self-Sensing of Deflection, Force and Temperature for Joule-Heated Twisted and Coiled Polymer Muscles via Electrical Impedance*, IEEE/ASME Transactions on Mechatronics, Vol. 22, Issue 3, pp. 1268-1275 (2016).

Conference papers

2. **J.O. van der Weijde**, E. Vlasblom, P. Dobbe, H. Vallery and M. Fritschi *Force Sensing for Compliant Actuators using Coil Spring Inductance*, IEEE/RSJ International Conference on Intelligent Robots and Systems September 2015, pp. 2692-2697.

1. **J.O. van der Weijde** and M. Heertjes *Design of a fractional-order integrator for high-precision stages*, IEEE American Control Conference June 2014, pp. 978-983 [not a part of this thesis].